uS

FACULTY OF SCIENCE AND TECHNOLOGY

MASTER'S THESIS

Acknowledgements

"Education is not the learning of facts, but the training of the mind to think."

Albert Einstein

I am fortunate to have been supervised by Dr. Guang Yin, whose knowledge, experience, and commitment inspired me to complete this master's thesis project. I am grateful to him for constant guidelines, and also taking time to revise the thesis.

I thank my other supervisor, Prof. Muk Chen Ong, who played an active role in improving the thesis with his expertise and insightful comments.

Abstract

Bluff bodies have extensive implementation in engineering. For instance, marine risers, jumpers, umbilicals, and bundle flowlines are the examples of the circular bluff bodies which are used in the field of offshore engineering. They can be designed both to be fixed or flexible supported and to be a single or tandem configurations. The subsea structures are subjected to the external hydrodynamic loads such as cyclic loads, vibrations, high pressure, etc. For example, one of the commonly observed damaging flow features associated with hydrodynamics of the flexible supported bluff bodies is vortex shedding. Therefore, investigation of the instantaneous flow structures and the hydrodynamic forces acting on the bluff bodies at the operational conditions need to be performed to prevent the degradation mechanisms and increase service life of the subsea structures. Nowadays, the modern techniques are used in order to analyse the flow field data with high efficiency. For example, neural networks (NNs) are trained with massive experimental or numerical simulation data to predict the spatial-temporal evolution of the dominant coherent structures of the flow field and structural behaviour can be considered as an alternative to the conventional computational fluid dynamics (CFD) simulations. In the present thesis, numerical investigations of the flow around cylindrical bluff bodies in the upper transition Reynolds number regime ($Re = 3.6 \cdot 10^6$) are performed. Two pipeline operational conditions are considered. First one is tandem configuration of the two stationary pipelines subjected to steady flow. Second one is a pipeline undergoing the vortex-induced-vibrations (VIV) subjected to a steady current. Two-dimensional (2D) Unsteady Reynolds-Averaged-Navier-Stokes (URANS) equations combined with the standard $k-w\,SST$ turbulence model are solved. The open source CFD toolbox OpenFOAM v2012 is employed to perform the simulations. The Reduced Order Models (ROMs) which can provide a low-dimensional representation of the simulation data with reduced computational time and cost are designed. Dynamic mode decomposition (DMD) and proper orthogonal decomposition (POD) techniques are implemented for the first and second cases, respectively. In addition, further development of the ROMs for the VIV cylinder case is done by implementing the long short-term neural network (LSTM-NN). The neural network based model allows to make the predictions of the dominant hydrodynamic characteristics of the flow around the cylindrical bluff bodies subjected to a high Reynolds number flow at a future time instances with a reduced computational cost.

List of Appended Publications

Paper 1

Nazvanova, A.; Yin, G.; Ong, M.C. Numerical Investigation of Flow around Two Tandem Cylinders in the Upper Transition Reynolds Number Regime Using Modal Analysis. *J. Mar. Sci. Eng.* **2022**, 10, 1501.

Paper 2

Nazvanova, A.; Ong, M.C.; Yin, G. A Data Driven Reduced Order Model based on Long Short-Term Memory Neural Network for Vortex-Induced Vibrations of a Circular Cylinder. *J. Physics of Fluids.* **2023**, 35, 065103.

Table of Contents

Chapter 1.

Introduction

1.1. Background and motivation

Investigation of the flow structures around the bluff bodies has gained the essential attention during the past decades as the bluff bodies are widely used in engineering structures. For instance, cylindrical bluff bodies are extensively implemented in offshore engineering as production pipelines, power cables, jumpers, umbilicals, etc. They can be designed to be fixed or flexible supported and to be a single or tandem configurations subjected to a uniform or oscillatory flow. Subsea structures experience a high Reynolds number ($Re = U_\infty D/\nu$, where U_∞ is a free stream velocity, D defines cylinder diameter and ν is the kinematic viscosity) flow up to 10^7 as reported by Sumer and Fredsøe (1997) [1] and Ong. et al. (2009) [2]. In addition, there are external loads acting on the structures due to surrounding flow. For example, vortex shedding of the separated from the cylinder surface shear layers can lead to a vortex induced vibrations of the body if the vortex-shedding frequency is synchronized with the natural frequency of the system. This phenomenon causes a fatigue degradation of the structures due to cyclic loads. Therefore, combination of the various impact factors leads to a significant reduction of the fatigue life of the subsea structures. Analysis of the hydrodynamic forces and flow features around the bluff bodies allows to understand the phenomena causing the degradation mechanisms and improve the design of the subsea structures. A lot of experimental studies as well as computational fluid dynamics (CFD) simulations have been conducted previously to investigate the flow hydrodynamics around a single circular cylinder (Sumer & Fredsøe 1997 [1], Tritton 1959 [3], Dimopoulos & Hanratty 2006 [4]), tandem cylinder configuration (Zdravkovich et al., 1977 [5], Zhou 2004 [6], Alam 2011) [7]) as well as vortex-induced vibration (VIV) cylinder (Pan et al., 2007 [8], Pang et al., 2016 [9], Kang et al., 2019 [10]).

However, experimental investigations require expensive laboratory equipment to reproduce the real flow at high Reynolds numbers with a minimum instrumental error and solving the Navier-Stokes equations leads to enormous computational costs. Therefore, a modern approach based on the reduced-order model (ROM) is designed to analyse the flow data in an efficient way. To build the ROM for the flow system, a

modal decomposition of the flow data should be performed. The main idea of the decomposition techniques such as proper orthogonal decomposition (POD) and dynamic mode decomposition (DMD) is to extract the most dominant spatial-temporal coherent structures of the flow field to achieve the model reduction. POD (Janocha et al., 2022 [11], Eiximeno et al., 2022 [12]) and DMD (Jovanovic et al., 2014 [13], Janocha et al., 2021 [14]) methods were successfully implemented for investigation of the flow field around the bluff bodies under flow-induced vibrations. When the dominant modes containing most of the flow energy are extracted, a ROM based on that modes can be built to predict the future time instants of the flow systems. One of the approaches which allows to achieve it is the Galerkin Projection (GP) method. It gives an approximate description of the real flow dynamics developed in time. It was implemented by Rapun & Vega (2010) [15], Rowley et al. (2004) [16] and Carlberg et al. (2011) [17] for solving different milestone problems. However, it is difficult to achieve both accuracy and stability by solving the GP reduced order model as reported by Iollo et al. (2000) [18] who investigated the flow around an airfoil and a square cylinder.

In order to overcome the disadvantages of the GP method, a promising approach based on deep learning is proposed to model the nonlinear systems, for example, turbulent flow. The advantage of the deep learning method is the ability to understand the correlations between the different parameters of the dataset and to predict their values purely based on data. There are various types of the neural network for different problems can be utilized: multi-layer perceptron (MLP) (Gardner & Dorling 1998 [19]), convolution neural network (CNN) (Cheng et al., 2021 [20]), recurrent neural network (RNN) (Zhang & Xiao 2000 [21]) and long-short-term memory neural network (LSTM-NN) (Rahman et al. (2019) [22]).

Although the neural network based ROMs are fast developing nowadays, their application in the hydrodynamics analysis of the flow around the bluff bodies as well as fluid-structure-interactions is limited. Therefore, the main motivation of the master's thesis project is to evaluate the effectiveness of the analysing the surrounding flow structures and hydrodynamic forces acting on the cylindrical bluff bodies at a high Reynolds number flow by using modal analysis and neural network techniques.

1.2. Objectives and methodology

In the master's thesis, two pipeline configurations subjected to a high Reynolds number uniform flow ($Re = 3.6 \times 10^6$) are considered and investigated. The first pipeline arrangement is two tandem fixed cylinders with the center-to-center spacing ratios (L/D) of $1.56, 1.8, 2.5, 3, 3.7, 4$. The second pipeline configuration is a flexible supported cylinder subjected to vortex-induced vibrations with a reduced velocity of $u_r = 3, 6,$ and 11. Two-dimensional (2D) Unsteady Reynolds-Averaged-Navier-Stokes (URANS) equations combined with the standard $k - \omega$ SST turbulence model are solved to investigate the flow features of the two proposed cases. The open source CFD toolbox OpenFOAM v2012 is employed to perform the simulations. The ROMs are designed by means of the POD and DMD model reduction techniques. The number of modes is chosen individually for each case to capture the dominant flow dynamics. The LSTM-NN is applied to predict the evolution of the flow structures at the future time instances for the VIV cylinder case. The LSTM-NN is designed based on the open-source toolbox TensorFlow and Keras.

The main objectives investigated within the scope of the first appended publication are defined as follow:

- Analyse the influence of the relative distance between two tandem cylinders subjected to a high Reynolds number flow on the lift and drag coefficients as well as the instantaneous flow structures based on the hydrodynamic quantities, power spectral analysis of their fluctuation and instantaneous flow structures.
- Create the ROMs based on the most dominant modes extracted by the SPDMD algorithm and confirm the ability of the designed SPDMD-ROMs to accurately reconstruct the surrounding flow and hydrodynamic properties by comparing the lift and drag force time-histories, obtained by the simulation results and the reduced order representations.

The main objectives investigated within the scope of the second appended publication are defined as follow:

- Design the ROMs based on the POD modes and implement the LSTM-NN for prediction of the POD temporal coefficients and streamwise and cross-flow velocities and displacements of the cylinder.
- Implement the force partitioning method (FPM) to predict the hydrodynamic forces acting on the cylinder purely based on the surrounding flow field predicted by using

the POD-LSTM-NN ROMs. The predicted time-histories of the lift and drag forces are compared with the CFD simulation results.

1.3. Thesis structure

The content of each chapter is summarized as follow:

Chapter 2: The chapter provides the theoretical review of the fundamental knowledge about the flow hydrodynamics around the circular bluff body, modal decomposition techniques and machine learning basic principles.

Chapter 3: Numerical investigation of flow around two tandem cylinders in the upper transition Reynolds number regime using modal analysis.

This chapter contains the paper which is published on Journal Marine Science and Engineering and also selected as the cover page paper. The influence of the center-to-center spacing between the two tandem cylinders undergoing a high Reynolds number regime flow to the coherent structures around the bluff bodies as well as the acting hydrodynamic forces are investigated. Furthermore, ROMs are created based on the most dominant DMD modes extracted by using the sparsity promote algorithm. The time histories of the lift and drag force of the reduced-order representations are compared with those obtained by the CFD simulations.

Chapter 4: A data driven reduced order model based on long short-term memory neural network for vortex-induced vibrations of a circular cylinder.

This chapter contains a paper which is published in Physics of Fluids. The feasibility of the POD-ROM- LSTM-NN to predict the flow field evolution around a VIV cylinder subjected to a high Reynolds number flow is evaluated in this paper. Different values of the reduce velocities are considered. In addition, FMP is applied to estimate the hydrodynamic forces acting on the bluff body using the surrounding flow field predicted by the POD-ROM- LSTM-NN as well as the original flow field calculated by means of CFD.

Chapter 5: The chapter provides the main conclusions of the master's thesis research work as well as suggestions for further investigations.

References

1. Sumer, B; Fredsøe, J. Hydrodynamics around Cylindrical Structures; World Scientific Publishing Co., Pte. Ltd.: Singapore, **1997**.

2. Ong, M.C.; Utnes, T. Numerical simulation of flow around a smooth circular cylinder at very high Reynolds numbers. *J. Mar. Struct.* **2009**, 22, 142–153.

3. D. Experiments on the Flow past a circular cylinder al low Reynolds numbers. *J. Fluid Mech.* **1959**, 6, 547–567.

4. Dimopoulos, H; Hanratty, T. Velocity gradients at the wall for flow around a cylinder for Reynolds numbers between 60 and 360. *J. Fluid Mech.* **2006**, 33, 303–319.

5. Zdravkovich, M. Review of flow interference between two circular cylinders in various arrangements. *J. Fluids.* **1977**, 99, 618–663.

6. Xu, G.; Zhou, Y. Strouhal numbers in the wake of two inline cylinders. *J. Exp. Fluids.* **2004**, 37, 248–256.

7. Alam, A. Two interacting cylinders in cross flow. *J. Phys.* Rev. E. **2011**, 84, 639–654.

8. Pan, Z; Cui, W; Miao, Q. Numerical simulation of vortex-induced vibration of a circular cylinder at low mass-damping using RANS code. Journal of Fluids and Structures. **2007**, 23(1), 23-37.

9. Pang, A; Skote, M; Lim, S. (2016). Modelling high Re flow around a 2D cylindrical bluff body using the k-ω (SST) turbulence model. *J. Progress in CFD.* **2016**, 16(1), 48-57.

10. Kang, Z; Zhang, C; Chang, R; Ma, G. A numerical investigation of the effects of Reynolds number on vortex-induced vibration of the cylinders with different mass ratios and frequency ratios. *J. Naval Architecture and Ocean Engineering.* **2019**, 11(2), 835-850.

11. Janocha, M; Ong, M; Yin, G. Large eddy simulations and modal decomposition analysis of flow past a cylinder subject to flow-induced vibration. Physics of Fluids. **2022**, 34(4), 045119.

12. Eiximeno, B; Miró, A; Cajas, J; Lehmkuhl, O; Rodriguez, I. On the Wake Dynamics of an Oscillating Cylinder via Proper Orthogonal Decomposition. *J. Fluids.* **2022**, 7(9), 292.

13. Jovanović, M; Schmid, P; Nichols, J. Sparsity-promoting dynamic mode decomposition. *J. Physics of Fluids.* **2014**, 26(2), 024103.

14. Janocha, M; Yin, G; Ong, M. Modal Analysis of Wake Behind Stationary and Vibrating Cylinders. *J. Off. Mech. and Arctic Engineering.* **2021**, 143(4).

15. Rapún, M; Vega, J. Reduced order models based on local POD plus Galerkin projection. *J. Comp. Physics*. **2010**, 229(8), 3046-3063.

16. Rowley, C; Colonius, T; Murray, R. Model reduction for compressible flows using POD and Galerkin projection. *J. Physica D: Nonlin. Phenomena*. **2004**, 189(1-2), 115-129.

17. Carlberg, K; Bou-Mosleh, C; Farhat, C. Efficient non-linear model reduction via a least-squares Petrov–Galerkin projection and compressive tensor approximations. *J. Num. methods in engineering*. **2011**, 86(2), 155-181.

18. Iollo, A; Lanteri, S; Désidéri, J. Stability properties of POD–Galerkin approximations for the compressible Navier–Stokes equations. J. *Theor. and Comp. Fl. Dyn*. **2000**, 13(6), 377-396.

19. Gardner, M; Dorling, S. Artificial neural networks (the multilayer perceptron)—a review of applications in the atmospheric sciences. *J. Atmospheric environment*. **1998**, 32(14-15), 2627-2636.

20. Cheng, W; Wang, Y; Peng, Z; Ren, X; Shuai, Y; Zang, S; Wu, J. High-efficiency chaotic time series prediction based on time convolution neural network. *J. Chaos, Solitons & Fractals*. **2021**, 152, 111304.

21. Zhang, J; Xiao, X. Predicting chaotic time series using recurrent neural network. *J. Chinese Physics Letters*. **2000**, 17(2), 88.

22. Rahman, S; Pawar, S; San, O; Rasheed, A; Iliescu, T. Nonintrusive reduced order modeling framework for quasigeostrophic turbulence. *J. Phys. Review E*. **2019**, 100(5), 053306.

Chapter 2.

Theory

2.1. Hydrodynamics around cylindrical structures

2.2.1. Boundary layer

According to Schlichting & Gersten 2016 [1], when a fluid flows over a stationary surface, the boundary layer is developed. It is a region where the flow adjusts from zero velocity at the wall to the free stream velocity in the mainstream zone. The viscous effects cannot be ignored in the boundary layer while the outer layer can be considered inviscid as reported by Cimbala & Cengel 2006 [2]. According to Kundu et al. (2012) [3], the boundary layer equations for two-dimensional (2D) and steady flow can be written as follow:

$$\frac{\partial u}{\partial x} + \frac{\partial v}{\partial y} = 0, \tag{2.1}$$

$$u\frac{\partial u}{\partial x} + v\frac{\partial v}{\partial y} = U\frac{\partial U}{\partial x} + v\frac{\partial^2 u}{\partial y^2}, \tag{2.2}$$

where U denotes the free stream velocity; u and v are streamwise and cross flow velocity components, respectively. The flow separates from the surface at the point where the shear stress is zero and a pressure gradient changes from favourable to adverse:

$$\tau_w = \mu \cdot \frac{\partial u}{\partial y} = 0, \tag{2.3}$$

where τ_w denotes the wall shear stress. Figure 2.1 shows the boundary layer separation from a circular cylinder surface. Starting from the stagnation point when the incoming flow hit the structures where the pressure is the highest, the boundary layer is subjected to a favourable pressure gradient and the flow is accelerated. However, due to the curvature of the cylindrical body surface, the flow will deaccelerate and will be subjected to an adverse pressure gradient due to the reduced flow velocity. Therefore, there is one location where the shear stress which balance the pressure gradient becomes zeros and the boundary layer is separated from the body surface to form a vortex. However, due to changing separation point at a high Reynolds number regime

flow, the vortex will grow faster from one side than the other side. As a result, the strong vorticity is cut off by the weak vortex from the other side and shed from the cylinder. This process will happen alternatively from the two sides of the cylinder.
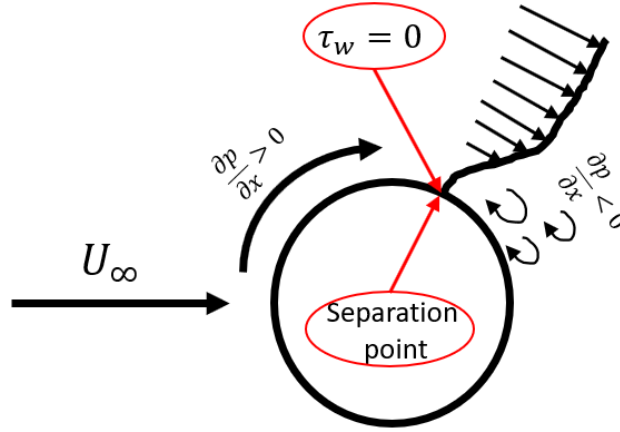

Figure 2.1. Boundary layer separation from a circular cylinder.

With increasing the Reynolds number, a transition from laminar to turbulent boundary layer occurs. The laminar boundary layer is characterized by the smooth paths in parallel layers of the fluid particles while the turbulent boundary layer is depicted by the appearance of the turbulent eddies. The turbulent boundary layer can be separated into viscous sublayer, buffer layer, log law and outer regions. The nondimensional parameters such as dimensionless velocity (U^+), dimensionless distance from the surface (y^+) and shear velocity (u_τ) are derived to define the various boundary layer regions:

$$U^+ = \frac{U}{u_\tau}, \tag{2.4}$$

$$y^+ = \frac{u_\tau y}{v}, \tag{2.5}$$

$$u_\tau = \sqrt{\frac{\tau_w}{\rho}}, \tag{2.6}$$

where τ_w is the shear stress and ρ is the density of the flow. The viscous sublayer is located in a range from $y^+ = 0$ to $y^+ = 5$. The velocity profile of the viscous sublayer varies linearly and can be expressed as follow:

8

$$U^+ = y^+. \tag{2.7}$$

When the y^+ takes the values in a range of $5 < y^+ < 30$, the buffer region dominates. The log low region following by the buffer region is located in the range of $30 < y^+ < 500$. The velocity profile of the log low region can be defined as follow:

$$U^+ = \frac{1}{\kappa}\ln(y^+) + B, \tag{2.8}$$

where B is the constant which typical value is 5; κ is denoted as the von Karman's constant which is equal to 0.41. The outer layer region is referred to the $y^+ > 500$.

2.2.2. Flow around a cylinder in a steady current

According to Sumer & Fredsøe (1997) [4], depending on the Reynolds number values, the flow around a circular fixed cylinder experiences different flow regime subjected to a steady current. The classification of the flow regimes around a fixed circular cylinder in a steady flow published by the Sumer & Fredsøe (1997) [4] is shown in Table 2.1.

Table 2.1. Flow regimes around a smooth circular cylinder in steady current. Reproduced from Sumer & Fredsøe (1997) [4].
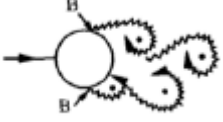
	No separation. Creeping flow	$Re < 5$
	A fixed pair of symmetric vortices	$5 < Re < 40$
	Laminar vortex street	$40 < Re < 200$
	Transition to turbulence in the wake	$200 < Re < 300$
	Wake completely turbulent. A: laminar boundary layer separation	$300 < Re < 3 \times 10^5$ Subcritical
	A: laminar boundary layer separation B: Turbulent boundary layer separation; but boundary layer laminar	$3 \times 10^5 < Re < 3.5 \times 10^5$ Critical (Lower transition)

Table 2.1. *Cont.*

	B: Turbulent boundary layer separation; but boundary layer partly laminar partly turbulent	$3.5 \times 10^5 < Re < 1.5 \times 10^6$ Supercritical
	C: Boundary layer completely turbulent at one side	$1.5 \times 10^5 < Re < 4.5 \times 10^6$ Upper transition
	C: Boundary layer completely turbulent at two sides.	$4.5 \times 10^6 > Re$ Transcritical

According to Table 2.1, at $Re < 5$, the creeping flow regime dominates. It is characterized by no separation of the shear layers from the cylinder surface. A fixed pair of vortices for the first time appears when the Reynolds number is in a range of $5 < Re < 40.$ With a further increase in the Reynolds number, the phenomenon called vortex shedding appear. The pairs of the alternately formed vortices separate at either side of the cylinder at a certain frequency forming a vortex street in the wake region of the cylinder. At $40 < Re < 200$, the vortex street is laminar and 2D as reported by Williamson (1989) [5]. The transition of the wake region to turbulence happens at $200 < Re < 300$. The wake region becomes fully turbulent only at $300 < Re < 3 \times 10^5$ while keeping laminar boundary layer separation. The vortex shedding occurs in a well-defined and regular pattern. For the Reynolds number range of $3 \times 10^5 < Re < 3.5 \times 10^5$, the boundary layer separation is turbulent at the one side of the cylinder and laminar at the other side. It causes the asymmetry in the flow behaviour. Due to constantly changing hydrodynamic forces on the cylinder surface the mean lift coefficient becomes non-zero. When Reynolds number is in a range $3.5 \times 10^5 < Re < 1.5 \times 10^6$, the boundary layer separation is observed at both sides of the cylinder while the transition to turbulence in the boundary layer has not been completed yet. With a further increase in the Reynolds number ($1.5 \times 10^6 < Re < 4.5 \times 10^6$), the boundary layer becomes completely turbulent at the one side of the cylinder while it is partially turbulent partially laminar at the other side. The asymmetry in the formation of the vortices results in a disordered and irregular vortex shedding. The boundary layer becomes totally turbulent at both sides of the cylinder at Reynolds number larger than 4.5×10^6 resulting in re-establishment of the regular vortex shedding formation.

2.2.3. Flow induced vibrations of a free cylinder in steady currents

In a case of a flexibly mounted circular cylinder, the lift and drag forces acting on the cylinder surface can cause the cross-flow and in-line vibrations of the circular bluff body, respectively, as reported by Sumer & Fredsøe (1997) [4]. Figure 2.2 shows a schematic illustration of a frequency response of a flexibly mounted circular cylinder in air with regard to cross-flow vibrations. According to Figure 2.2, when the reduced velocity ($u_r = U_\infty/f_n \cdot D$, where f_n denotes the natural frequency of the system in a vacuum) is smaller than 4, the circular cylinder does not experience vibration. At that region, the vortex shedding frequency (f_v) follows the stationary cylinder Strouhal frequency. At $u_r = 4$, the vibrations begin to emerge as reported by Sumer & Fredsøe (1997) [4]. At $5 < u_r < 7$, the natural frequency (f_n) of the system is synchronized with the vortex shedding frequency: $f = f_n = f_v$. This phenomenon is known as lock-in. It is characterized by the large vibration amplitudes of the cylinder. With further increase in the u_r values, the vortex shedding frequency unlocks the natural frequency and starts to follow a Strouhal low again.
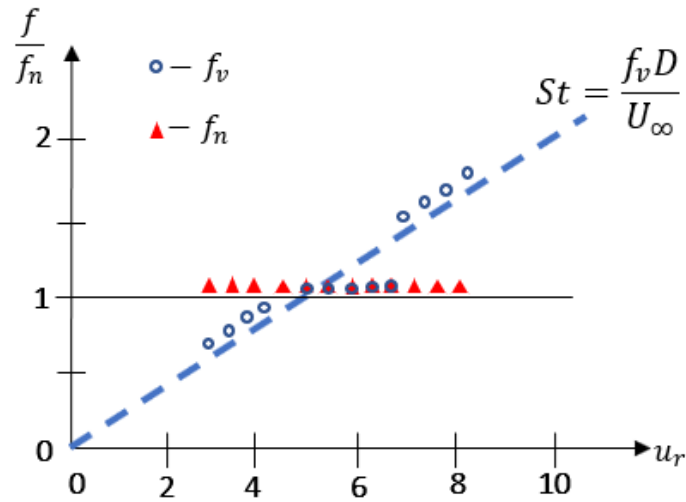
Figure 2.2. Schematic illustration of a frequency response of a flexibly mounted circular cylinder in air with regard to cross-flow vibrations.

Wake topology depending on the reduced velocity for a two degree of freedom (2DoF) cylinder with a low mass ratio is splitted into the initial branch, the upper branch, and the lower branch as reported by Williamson & Roshko (1988) [6]. Figure 2.3 shows the flow structures around 2DoF cylinder subjected to steady current at different branches. The initial branch is characterized by the formation of two single counter-rotating vortices (2S) per shedding cycle, similar to the von-Karman vortex

street observed behind a stationary cylinder as shown in Figure 2.3a. The cylinder undergoes a low amplitude of oscillation in streamwise and cross flow directions. With the increase in u_r, the upper branch starts to dominate. The main feature of the upper branch flow pattern is the separation of two triplets (2T) of vortices per shedding cycle as shown in Figure 2.3b. In the upper branch, the system reaches its higher oscillation amplitudes. Finally, the lower branch occurs at large u_r. It is indicated by the separation of the two pairs (2P) of the counter-rotating vorticities per shedding cycle as shown in Figure 2.3c. The motion amplitude of the system at the lower branch is reduced in comparison with the upper branch.

| **(a)** | **(b)** | **(c)** |
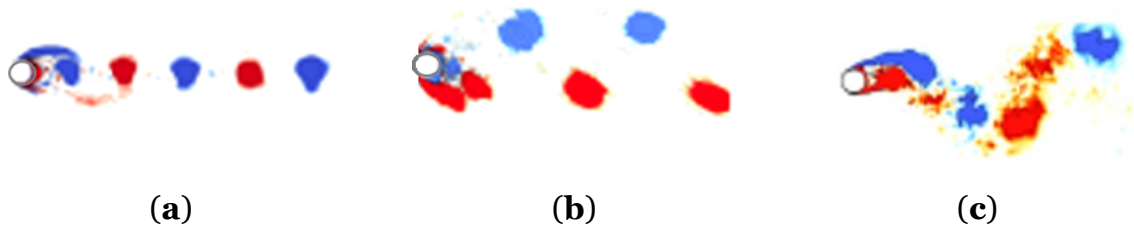
Figure 2.3. Wake topology of the (**a**) initial branch (2S), (**b**) upper branch (2T), (**c**) lower branch (2P). Reproduced from Eiximeno et al. (2022) [7].

2.2. Decomposition techniques

The reduced order modelling allows to represent a high-dimensional dynamical systems using a low dimensional subspace while keeping the relatively high accuracy of the simulated results and decreasing computational time. In order to build ROM of the non-linear dynamical system, the decomposition techniques can be utilized. The main idea of the various decomposition methods is to extract the dominant spatial-temporal coherent structures of the flow field in order to achieve a model reduction. POD method is one of the most popular decomposition techniques. The main feature of the POD method is that spatial modes (ϕ_m) and their corresponding time coefficients ($a_m(t)$) are extracted based on the energy content of the flow. These modes are orthogonal to each other, and each POD mode contains continuous frequency spectral. A reduced order approximation of the flow field by using the most energetic POD modes can be represented as:

$$u(x,y,t) \approx \sum_{n=1}^{N} a_n(t) \cdot \phi_n(x,y),$$

(2.9)

where $u(x, y, z, t)$ is the data which consists of streamwise and crossflow velocities of the flow field at each time step; N is the number of the dominant POD modes.

Singular Value Decomposition (SVD) technique can be applied to decompose the flow field data presented in a form of matrix. A snapshot $\boldsymbol{u}_p \in \mathbb{C}^n$ consists of samples of the flow field data with subscript p indicating sampling at time t_p: $\boldsymbol{u}_p := [\boldsymbol{u}(x_1, t_p)\, \boldsymbol{u}(x_2, t_p) \ldots \boldsymbol{u}(x_n, t_p)]^T$, where n denotes the spatial location. A time series of data, with m measurement instances in time can be presented in a tall-skinny matrix $\mathbf{X}$ as usually $n \gg m$:

$$\mathbf{X} = \begin{bmatrix} | & | & | \\ \boldsymbol{u}_1 & \boldsymbol{u}_2 \ldots \boldsymbol{u}_m \\ | & | & | \end{bmatrix}, \tag{2.10}$$

SVD approach can be implemented to decompose the matrix $\mathbf{X} \in \mathbb{C}^{n \times m}$ to the components:

$$\mathbf{X} = \mathbf{U}\boldsymbol{\Sigma}\mathbf{V}^{\mathbf{T}}, \tag{2.11}$$

where $\mathbf{U} \in \mathbb{C}^{n \times n}$ and $\mathbf{V} \in \mathbb{C}^{m \times m}$ are unitary matrices and $\boldsymbol{\Sigma} \in \mathbb{C}^{n \times m}$ is a matrix with non-negative values on the diagonal. The matrix $\mathbf{U}$ presents the eigenvalues of the modes, the matrix $\mathbf{V}$ gives the time history evolution of each POD mode while the diagonal matrix $\boldsymbol{\Sigma}$ shows the weighting of each mode relative to the others.

The other decomposition technique which is widely implemented is DMD. The non-orthogonal DMD modes are characterized by their dynamics. Each DMD mode has its own single frequency. The snapshots of the flow field data can be arranged into two data matrices, $\mathbf{X}$ and $\mathbf{X}'$:

$$\mathbf{X} = \begin{bmatrix} | & | & | \\ \boldsymbol{u}_1 & \boldsymbol{u}_2 \ldots \boldsymbol{u}_{m-1} \\ | & | & | \end{bmatrix}, \tag{2.12}$$

$$\mathbf{X}' = \begin{bmatrix} | & | & | \\ \boldsymbol{u}_2 & \boldsymbol{u}_3 \ldots \boldsymbol{u}_m \\ | & | & | \end{bmatrix}. \tag{2.13}$$

The DMD approach tries to find the best fit linear operator A which can connect the two snapshot matrices in time as reported by Brunton & Kutz (2022) [9]:

$$\mathbf{X}' \approx A\mathbf{X} \tag{2.14}$$

The best-fit operator A can be defined as follow:

$$A = \underset{A}{\mathrm{argmin}}\|\mathbf{X}' - \mathbf{AX}\|_F = X'X^\dagger,$$

(2.15)

where $\|.\|_F$ is the Frobenius norm and $\dagger$ is the pseudo-inverse. The more detailed explanation of the DMD approach can be found in Brunton & Kutz (2022) [9].

2.3. Machine learning basic principles

Machine learning is a sub-field of artificial intelligence. It refers to the idea that the computer programs can define correlations between the new impute data and learn them without human assistance. A sub-set of machine learning is Neural Network (NN) which is designed in analogy to the structure and functions of the brain's neural network. The model used in NN is called Artificial Neural Network (ANN) which is the collection of connected units (neurons) that are organized into input, hidden and output layers as reported by Jung (2022) [8]. If ANN has more than one hidden layer, the ANN is considered as a deep ANN. Figure 2.4. shows the main components of the deep ANN.
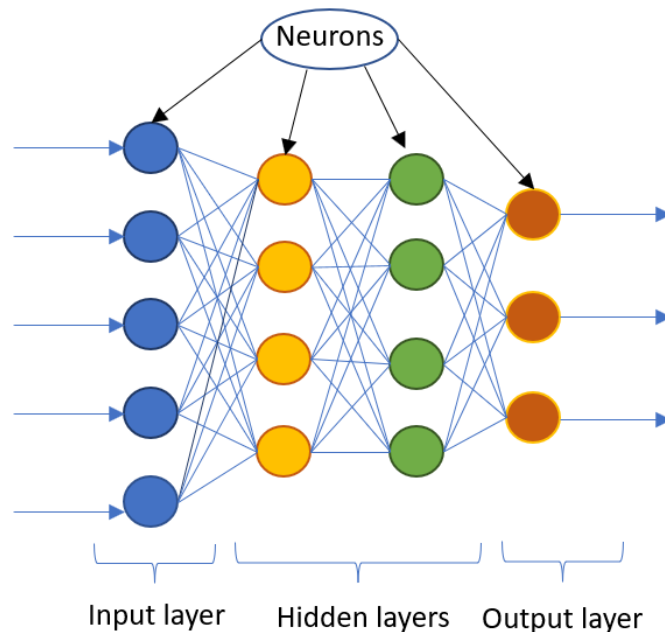

Figure 2.4. The diagram of the deep ANN architecture.

According to Figure 2.4, each node is connected to every node in the next layer. Each connection between two nodes has an associated weight which represents the

connection strength between the two neurons. The input signal sent to the node of the input layer passes via a connection to reach the neuron of the following layer. The input signal will be multiplied by the weight assigned to that connection. The weighted sum of the following layer node is calculated as a sum of all incoming connection values. Then the weighted sum of the node is passed to an activation function. The activation function (Sigmoid activation function, ReLU activation function, Swish, etc.) allows to modify the sum to be a number between defined values. For example, the Sigmoid activation function transforms the input to be between zero and one.

The training of the neural network is finding the most suitable values of the weights within the model. During the optimization process, the weights are updated iteratively and changed towards their optimal values. Therefore, the mean absolute scaled error (MASE) is used to evaluate how good the model is compared with the real data. The mean MASE is calculated as follow:

$$MASE = \frac{1}{n}\sum_{i=1}^{n}\left|\frac{A(i)-B(i)}{\sum_{j=2}^{n}\frac{A(j)-A(j-1)}{n-1}}\right|, \tag{2.16}$$

where n is the total number of the time instants; $A(i)$ denotes the real value at the time instant i; $B(i)$ is the forecasted value at the time instant i.

Different datasets are used for training of the model and its testing. The training set is used only for the model training purposes. While the test data set is used to validate the performance of the designed neural network model. The two most common issues of the neural network are overfitting and underfitting. Figure 2.5 shows the schematic illustration of the models undergoing underfitting and overfitting, and balanced model. The overfitting problem occurs when the model exactly fits against its training data while it cannot perform accurately against unseen data as shown in Figure 2.5a. This issue can be solved if more data to the training set can be added, the complexity of the modal is reduced, or the data augmentation technique is applied. The underfitting model is the model which has quite low training accuracy and cannot classify the data properly as shown in Figure 2.5b. In order to overcome the underfitting issue, measures such as increasing the complexity of the model or adding more features to the input samples can be used. Figure 2.5c shows the balanced model with the optimally chosen parameters for data classification.
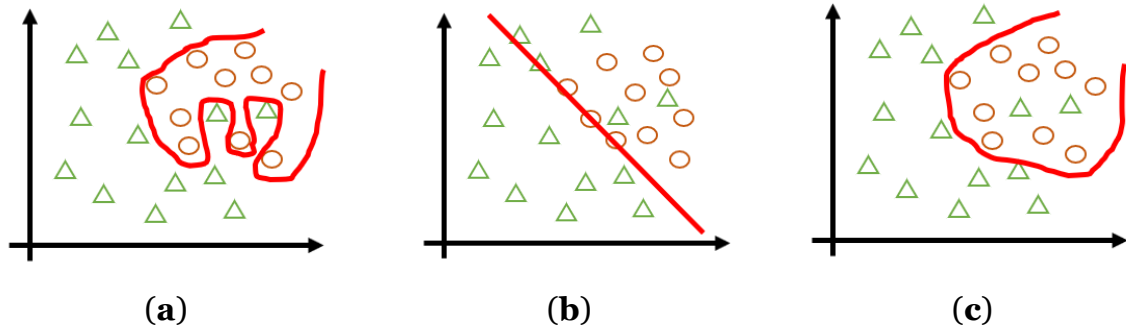
Figure 2.5. Schematic illustration of the (**a**) overfitting model, (**b**) underfitting model and (**c**) balanced model.

References

1. Schlichting, H; Gersten, K. *Boundary-layer theory*. springer. **2016**.

2. Cimbala, J; Cengel, Y. *Fluid mechanics: fundamentals and applications*. McGraw-Hill Higher Education. **2006**.

3. Kundu, P; Cohen, I; Dowling, D. *Fluid mechanics*. Academic press. **2015**.

4. Sumer, B.; Fredsøe, J. Hydrodynamics around Cylindrical Structures; World Scientific Publishing Co., Pte. Ltd.: Singapore, **1997**.

5. Williamson, C. Oblique and parallel modes of vortex shedding in the wake of a circular cylinder at low Reynolds numbers. *Journal of Fluid Mechanics*. **1989**, *206*, 579-627.

6. Williamson, C; Roshko, A. Vortex formation in the wake of an oscillating cylinder. J. Fluids Struct. **1988**, 2, 355–381.

7. Eiximeno, B; Miró, A; Cajas, J; Lehmkuhl, O; Rodriguez, I. On the Wake Dynamics of an Oscillating Cylinder via Proper Orthogonal Decomposition. *Fluids*, **2022**, *7*(9), 292.

8. Jung, A. *Machine learning: The basics*. Springer Nature. **2022**.

9. Brunton, S; Kutz, J. *Data-driven science and engineering: Machine learning, dynamical systems, and control*. Cambridge University Press. **2022**.

Chapter 3.

Numerical Investigation of Flow around Two Tandem Cylinders in the Upper Transition Reynolds Number Regime Using Modal Analysis

Anastasiia Nazvanova [a], Guang Yin (尹光) [a] and Muk Chen Ong [a]

[a] Department of Mechanical and Structural Engineering and Material Science, University of Stavanger, N-4036 Stavanger, Norway.

Abstract

Flow around two tandem cylinders at $Re = 3.6 \times 10^6$ for different center-to-center spacing ratio (L/D) is investigated numerically using two-dimensional (2D) Unsteady Reynolds-Averaged Navier–Stokes (URANS) equations combined with a standard $k - \omega$ SST turbulence model. The instantaneous flow structures around the cylinders, hydrodynamic forces on the cylinders and Strouhal number (St) are analyzed and discussed. Dynamic Mode Decomposition (DMD) is used to extract the spatiotemporal information of the coherent flow structures in the wake regions behind the upstream (UC) and downstream (DC) cylinders. A sparsity-promoted algorithm is implemented to select the dominant modes which contribute the most to the dynamics of the system. Based on the dominant modes, a reduced-order representation of the flows is built. A comparison of the lift and drag force–time histories, obtained by simulation results and the reduced-order representations, shows a high capability of the latter to reproduce the surrounding flow and hydrodynamic properties of the tandem cylinders at the high Reynolds number.

3.1. Introduction

Flow around tandem cylinders is of industrial and academic interest. In the field of offshore engineering, marine risers and subsea pipelines are usually subjected to a high Reynolds number flow in the order of 10^6 to 10^7 as reported by Sumer and Fredsøe (1997) [1] and Ong et al. (2009) [2]. When two cylinders are in proximity, there are complex hydrodynamic forces acting on the cylinders. The tandem configuration of the cylinders results in a complicated surrounding flow, due to the mutual interaction of the upstream cylinder (UC) and the downstream (DC) shear layers shedding from the cylinders. As a result, the impact of lift and drag forces becomes higher, compared with those for a single cylinder, and reduces the fatigue life of the cylindrical structures. Therefore, it is significant to explore the hydrodynamic forces and the instantaneous flow structures around cylinders subjected to a high Re flow to optimize the relative arrangement of the tandem cylindrical structures and increase their service life in the subsea environment.

Plenty of studies have been conducted to investigate the flow around, and forces on, circular, rectangular (Nakaguchi et al., 1968 [3], Norberg 1993 [4], Ohya 1994 [5], Okajima et al., 1990 [6], Tian et al., 2013 [7]) and triangular (Dutta et al., 2015 [8], El-Sherbiny et al., 1983 [9], Nakagawa 1989 [10], Cheng 2000 [11]) cylinders. Especially, the prediction of the flow separation around circular bluff bodies is a crucial topic for many researchers. The reason is the complexity of the separated flow caused by a constantly changing point of separation on the surfaces of the structures, due to the unsteadiness of the flow. Thus, comprehensive experimental studies have been conducted in the previous decades in order to get a deep understanding of the flow separation phenomenon. Tritton (1959) [12], Dimopoulos and Hanratty (2006) [13] investigated the flow around circular cylinders at low Re number experimentally. Trittion (1959) [12] conducted measurements of the drag force on the flow past a circular cylinder at $Re = 0.5{\sim}100$. Dimopoulos and Hanratty (2006) [13] employed electrochemical techniques to analyze the velocity gradient around the surface of a cylinder at $Re = 60{\sim}360$. They found that the values of the velocity gradient near the cylinder surface in the wake region are lower in comparison with that in the front part of the cylinder.

However, experimental investigation of hydrodynamic quantities and instantaneous flow structures requires suitable laboratory equipment to reproduce real

flow conditions to achieve correct scaling of the dimensionless parameters, such as *Re,* and also to minimize instrumental errors, which is difficult and expensive. Therefore, Computational Fluid Dynamics (CFD) has become increasingly popular, which allows the obtaining of full spatial and temporal information of the surrounding flow fields, including the flow velocities and pressures for engineering design. Park et al. (1998) [14] and Rajani et al. (2009) [15] numerically investigated the hydrodynamic coefficients and instantaneous flow patterns around cylindrical bluff bodies at low *Re* number. Park et al. (1998) [14] studied flow around a circular structure at *Re* numbers up to 160 by employing high resolution unsteady simulations. He reported that the simulation results showed a reasonable agreement with previously published experimental data. Rajani et al. (2009) [15] investigated instantaneous flow structures around a circular cylinder at $Re = 0.1 \sim 400$ by using an implicit pressure-based finite volume algorithm. He reported that the 2D numerical simulations results were in good agreement with the measured data up to $Re = 200$. However, beyond the critical Re number, differences between the simulation results and experimental data were observed, due to three-dimensional (3D) effects.

Investigation of the hydrodynamic quantities around tandem cylindrical bluff bodies has both practical and academic significance. A comprehensive review of the work on two cylinders in various arrangements was presented by Zdravkovich et al. (1977) [16] and Sumer et al. (2010) [17]. When a cylinder is placed in-line downstream of another cylinder, they are called a tandem arrangement. When two cylinders are placed in tandem, a complex flow structure is generated as a result of flow interference in the wake behind the upstream body. Flow around two tandem cylinders may be classified into three regimes based on the center-to-center spacing, *L/D,* between the two cylinders, as reported in Zdravkovich et al. (1978) [18]: 1) an extended body regime, where *L/D* ranges from 1 to 1.5. The two cylinders are placed sufficiently close to each other such that the free shear layers separated from the UC overshoot the DC; 2) a reattachment regime, where *L/D* is between 1.5 and 4 (critical *L/D*), and the shear layers reattach on the DC; 3) a co-shedding regime, where *L/D* is larger than a critical value and the shear layers from the two cylinders roll up alternately. A vortex street appears in the gap between, as well as behind, the cylinders.

Hori (1959) [19], Huhe-Aode et al. (1985) [20], Nishimura et al. (1986) [21], Xu and Zhou (2004) [22] and Alam et al. (2011) [23] analyzed the flow pattern around tandem cylinders at high *Re* number experimentally. Hori (1959) [19] performed

measurements in a closed-circuit wind tunnel over $Re = 800 \sim 4.2 \times 10^4$ and a cylinder center-to-center spacing of $L/D = 1 \sim 15$. His study confirmed the previous observation of a bi-stable flow between the reattachment and co-shedding regimes. Huhe-Aode et al. (1985) [20] investigated the wake flow structure behind two tandem cylinders at $Re = 100 \sim 1000$ experimentally by using a hot-wire anemometer and flow visualization techniques. Nishimura et al. (1986) [21] analyzed the flow pattern around two cylinders in tandem at $Re = 800 \sim 1 \times 10^4$. and the relative distance between two cylinders from 1.2 to 7.2, by using flow visualization techniques. Xu and Zhou (2004) [22] measured the dominant vortex frequencies in the wake region of two tandem cylinders by using two hot wires placed in tandem at $Re = 800 \sim 4.2 \times 10^4$ and $L/D = 1 \sim 15$, which also showed the existence of a bi-stable flow regime. Alam et al. (2011) [23] did experiments to investigate the influence of the L/D ratio between cylinders on the hydrodynamic coefficients at $Re = 9.7 \times 10^3 \sim 6.5 \times 10^4$ in a low-speed, closed-circuit wind tunnel. He proposed six different interaction mechanisms of the vortices between the cylinders which have different influence on the induced forces on the cylinders and St.

The present study focuses on prediction of flow structures around tandem cylinders at the upper transitional Reynolds number regime. To this date, the flow at this high Re has not been intensively explored. A prediction of hydrodynamic forces on cylinders, and the surrounding instantaneous flow structures, is challenging, due to the complexity of the flow at the high Re. The flow around a circular cylinder at $Re = 0.5 \times 10^6 \sim 4 \times 10^6$ was studied by Catalano et al. (2003) [24] by using both Large Eddy Simulations (LES) with a wall model and URANS simulations combined with the $k - \varepsilon$ turbulence model. He pointed out that LES solutions capture the delayed separation of the boundary layer on the surfaces of the cylinder and reduced drag coefficients after the 'drag crisis' more accurately than those obtained by using RANS simulations. Ong et al. (2009) [2] numerically solved 2D Unsteady Reynolds-Averaged Navier–Stokes (URANS) equations with a standard high Reynolds number $k - \varepsilon$ turbulence model at $Re = 1 \times 10^6, 2 \times 10^6$ and 3.6×10^6 to investigate the flow around a circular cylinder. It was found that the 2D simulations were capable of predicting the hydrodynamic coefficients at these high Re values. Hu et al. (2019) [25] analyzed the characteristics of the flow passing two tandem cylinders at both subcritical and supercritical Reynolds

numbers by using Improved Delayed Detached-Eddy Simulation (IDDES) for spacing ratio $2 \leq L/D \leq 5$.

In the analysis of the surrounding flow and the hydrodynamic forces on the cylindrical structures, statistics, such as the mean values, the root-mean-square values and spectra of the time histories of forces, were usually obtained. However, their relationship with the flow structures was not clearly revealed. Moreover, the turbulent wake flows were characterized by temporal and spatial multiscale vortical structures, which brought challenge to the analysis of the flow phenomena. Therefore, data-driven methods, such as Proper Orthogonal Decomposition (POD) and Dynamic Mode Decomposition (DMD), as well as their variations, allow the extraction of dominant flow features from time-dependent flow fields and the achievement of a deep understanding of the experimental, or simulation, results. In the present study, to reveal the spatiotemporal behaviors of the flow data, the DMD method was employed, which was proposed by Schmid (2010) [26] and is based on the Koopman operator theory of dynamical systems (Rowley et al., 2009 [27]). The development and use of modal decomposition techniques has gained increasing popularity in recent years due to its advantage in processing huge experimental and numerical simulations data, as reported by Taira et al. (2017) [28]. DMD decomposes flow data into the modes and their associated eigenvalues, which characterizes the frequencies and growth rates of the DMD modes. DMD has been used in a wide variety of applications, including the wake flows of circular cylinders, such as in the works by Bagheri et al. (2013) [29] and Hemati et al. (2017) [30], and for jet flow, such as in the work conducted by Schmid et al. (2011) [31].

The present study investigates the influence of the relative distances between two cylinders on the hydrodynamic coefficients and instantaneous flow structures in the upper transition Reynolds number regime. To obtain the flow data, two-dimensional (2D) Unsteady Reynolds Averaged Navier–Stokes (URANS) equations, with the standard $k - \omega$ SST turbulence model, are solved. The relationship between the dominant flow structures with the hydrodynamic forces were studied. The paper is organized as follows. Section 3.2 gives a brief introduction to the numerical method applied in the present study. The computational domain and the grid resolution convergence study are provided in Section 3.2. The validation study is performed by comparing the obtained hydrodynamic coefficients with the previously published data. In Section 3.3, the results and discussion, based on hydrodynamics quantities, power

spectra analysis of their fluctuations, and instantaneous flow structures, are presented. The DMD analysis is also performed. Finally, conclusions are presented in Section 3.4.

3.2. Numerical Modeling

3.2.1. Mathematical formulation

The two-dimensional incompressible URANS equations of mass and momentum conservation are given by:

$$\frac{\partial u_i}{\partial x_i} = 0, \tag{3.1}$$

$$\frac{\partial u_i}{\partial t} + u_j \frac{\partial u_i}{\partial x_j} = -\frac{1}{\rho}\frac{\partial P}{\partial x_i} + v\frac{\partial^2 u_i}{\partial x_j^2} - \frac{\partial \overline{u_i' u_j'}}{\partial x_j}, \tag{3.2}$$

where i, j = 1, 2; x_1, x_2 are the streamwise and cross-flow directions, respectively; u_1 and u_2 are the corresponding mean velocity components; $\overline{u_i' u_j'}$ is the Reynolds stress component where u_i' is the fluctuating part of the velocity; P is the dynamic pressure; ρ is the density of the fluid. The shear stress transport $k - \omega$ SST turbulence model (Menter et al., 2003 [32]) was applied in the present study. It consists of the $k - \omega$ and $k - \varepsilon$ models. The $k - \varepsilon$ model is suitable for simulating the free-stream flow, while it performs poorly where there are adverse pressure gradients, boundary layer separations and strong streamline curvatures. The $k - \omega$ model performs better under adverse pressure gradient conditions, and flow separations, compared with the $k - \varepsilon$ model. Therefore, the adopted $k - \omega$ SST model that is presented was selected because it can combine the advantages of the $k - \varepsilon$ model in the free stream outside the cylinder boundary layer and the advantages of the $k - \omega$ model to predict the boundary layer separations in the near-wall regions. The transport equations for specific dissipation rate ω and turbulence kinetic energy k are given by:

$$\frac{Dk}{Dt} = \widetilde{P_k} - \beta^* k\omega + \frac{\partial}{\partial x_j}\left[(v + \sigma_k v_t)\frac{\partial k}{\partial x_j}\right], \tag{3.3}$$

$$\frac{D\omega}{Dt} = \alpha S^2 - \beta^* \omega^2 + \frac{\partial}{\partial x_j}\left[(v + \sigma_\omega v_t)\frac{\partial \omega}{\partial x_j}\right] + 2(1 - F_1)\frac{\sigma_{\omega 2}}{\omega}\frac{\partial k}{\partial x_j}\frac{\partial \omega}{\partial x_j}, \qquad (3.4)$$

where $\widetilde{P_k}$ is a production limiter term given by the equation:

$$\widetilde{P_k} = \min\left[v_t\frac{\partial u_i}{\partial x_j}\left(\frac{\partial u_i}{\partial x_j} + \frac{\partial u_j}{\partial x_i}\right), 10\beta^* k\omega\right]. \qquad (3.5)$$

The variable φ_1 represents any constant in the standard $k - \omega$ model and φ_2 denotes any constant in the standard $k - \varepsilon$ model. The blending function F_1 is used to calculate the corresponding constant of the $k - \omega$ SST model:

$$\varphi = F_1\varphi_1 + (1 - F_1)\varphi_2, \qquad (3.6)$$

$$F_1 = \tanh\left\{\left[\min\left[\max\left(\frac{\sqrt{k}}{\beta^* \omega y}, \frac{500v}{y^2\omega}\right), \frac{4\rho\sigma_{\omega 2}k}{CD_{k\omega}y^2}\right]\right]^4\right\}, \qquad (3.7)$$

$$CD_{k\omega} = \max\left[2\rho\frac{\sigma_{\omega 2}}{\omega}\frac{\partial k}{\partial x_j}\frac{\partial \omega}{\partial x_j}, 10^{-10}\right], \qquad (3.8)$$

where y is the distance to the nearest wall, $CD_{k\omega}$ is the positive part of the cross-diffusion term in Eq. (3.4). The turbulent eddy viscosity v_t can be defined as:

$$v_t = \frac{a_1 k}{\max(a_1\omega, SF_2)}, \qquad (3.9)$$

where S represents the strain rate invariant and F_2 is a second blending function given by:

$$F_2 = \tanh\left[\left[\max\left(\frac{2\sqrt{k}}{\beta^* \omega y}, \frac{500v}{y^2\omega}\right)\right]^2\right]. \qquad (3.10)$$

The model constants: $\sigma_k, \sigma_\omega, \beta, \beta^*, \gamma$ have standard values and can be found in Menter et al. (2003) [32].

3.2.2. Numerical Method

The open source CFD toolbox OpenFOAM v2012 was used to perform all the simulations in the present study. The PIMPLE algorithm was used to solve the governing equations. It is a combination of the Semi-Implicit Method for Pressure Linked Equations (SIMPLE) and the Pressure Implicit with Split Operators (PISO) method. An implicit second order backward time integration scheme was applied. The divergence and gradient terms were discretized using the Gauss linear integration scheme. The Laplacian term was discretized using Gauss linear integration with limited non-orthogonal correction. All the used schemes were of second-order accuracy.

3.2.3. Computational domain

The computational domain is shown in Figure 3.1. The center of the front cylinder is located at a distance $10D$ from the inlet boundary and $25D$ from the outlet boundary. The center of the back cylinder is located with a horizontal center-to-center offset L from the front cylinder. The upper and lower boundaries are placed at the distance of $10D$ to the centers of both cylinders.
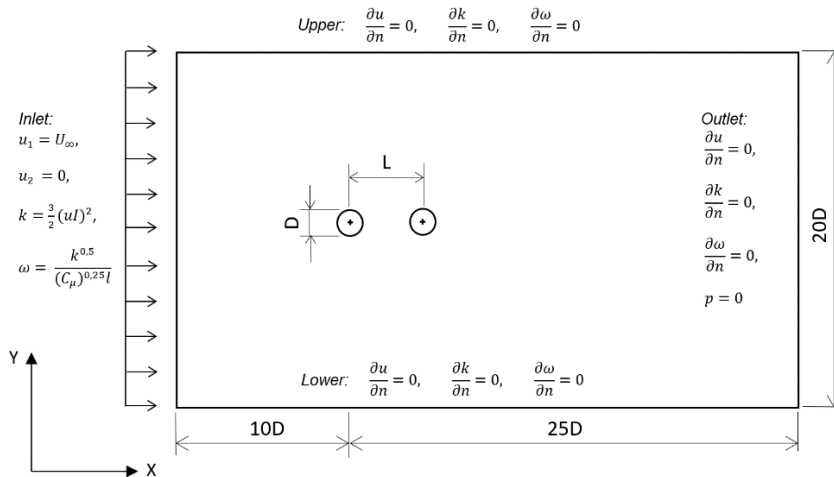

Figure 3.1. The computational domain for the tandem cylinders.

The boundary conditions used for the numerical simulations were set as follows:
1. A uniform flow was specified at the inlet as:

$$u_1 = U_\infty, \tag{3.11}$$

$$u_2 = 0, \tag{3.12}$$

$$k = \frac{3}{2}(uI)^2, \tag{3.13}$$

$$\omega = \frac{k^{0,5}}{(C_\mu)^{0,25}l}, \tag{3.14}$$

where $C_\mu = 0.09$ is the model constant; $l = 0.045D$ is the turbulent length scale; $I = 1\%$ is the turbulent intensity.

2. At the outlet of the domain, the velocities, k and ω were set as zero normal gradient condition and the pressure was set to be zero.

3. At the top and bottom of the domain, the velocities, the pressure, k and ω were set as zero normal gradient.

4. A no-slip boundary condition was applied for the velocities on the cylinder surfaces with $u_1 = u_2 = 0$. A standard wall function was used to resolve the near-wall boundary layer. Therefore, a criterion of $30 < y^+ < 40$ with y^+ was used, defined as:

$$y^+ = \frac{u_* h_p}{v}, \tag{3.15}$$

where u_* is the friction velocity defined as:

$$u_* = \sqrt{\frac{\tau_\omega}{\rho}} \tag{3.16}$$

and τ_ω is the wall shear stress.

3.2.4. Mesh convergence and validation studies

The aim of the mesh convergence study was to determine the appropriate grid resolutions for the simulations. The convergence studies were conducted on three computational grids, shown in Table 3.1, with a different number of cells for the single cylinder case. An example of the mesh for the case M1 in Table 3.1 is shown in Figure 3.2. The geometry of each grid was kept similar. The time step (Δt) used in the mesh convergence study was chosen such that a maximum Courant number (defined as $Co = u \cdot \Delta t / \Delta x$ where u is the velocity magnitude of the flow and Δx is the computational cell

size) at each time step was below 0.5. The difference in the cell number was approximately 50% between cases.

Table 3.1. Results of grid convergence study

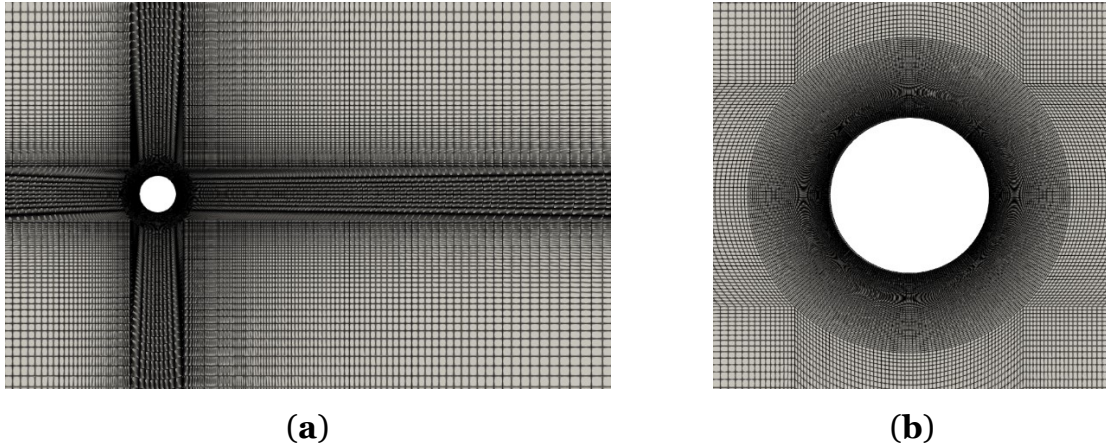| Case	No. of Cells	$\bar{C}_D$	$C_{L,rms}$	St
M1	74496	0.4657	0.1565	0.3227
M2	113256	0.4706	0.1599	0.3293
M3	171970	0.4639	0.1553	0.3221

(a)   (b)

Figure 3.2. Example of the mesh M2 (**a**) an overall view and (**b**) a zoom-in view of the mesh close to the cylinder

Table 3.1 presents the results of the grid convergence study of the single cylinder case. The results showed that the relative difference of the time-averaged drag coefficient (the drag coefficient C_D is defined as $F_D/(0.5\rho D U_\infty^2)$, where the force acting on the cylinder in the streamwise direction per unit length and the time-averaged values was calculated as $\bar{C}_D = \frac{1}{n}\sum_{i=1}^{n} C_{D,i}$) between cases, was lower than 2%. The relative difference of the root-mean-square values of the lift coefficient (the lift coefficient C_L is defined as $F_L/(0.5\rho D U_\infty^2)$, where the force acting on the cylinder in the cross-stream direction per unit length and the root-mean-square value was defined as $C_{L,rms} = \sqrt{\sum_{i=1}^{n}(C_{L,i} - \bar{C}_L)^2/n}$), was lower than 5%, and the relative difference of the Strouhal number (defined as $St = f_v D/U_\infty$, where f_v is the vortex shedding frequency obtained by performing fast Fourier transform of the time histories of the lift force coefficient C_L of the cylinder) was lower than 3% between cases. According to Table 3.1, the results suggested that for the computational grids with a cell number higher than

approximately 113,000, a further grid refinement showed a slight influence on the obtained hydrodynamic quantities. Therefore, it could be concluded that the mesh of the case M2 could provide sufficient grid resolution for the simulations.

The obtained hydrodynamic coefficients are compared with the previously published experimental and numerical simulation data in Table 3.2. Generally, the $\bar{C}_D$ predicted in the present simulation was within the range of the experimental data and in reasonable agreement with the numerical simulation results. However, the $C_{L,rms}$, which was more sensitive than the value of $\bar{C}_D$, was different from the obtained value of $C_{L,rms}$ reported by Ong et.al. (2009) [2], where the $k - \varepsilon$ turbulence model was applied. However, the present predicted values were close to those reported by Porteous et al. (2015) [33] and Pang et al. (2016). The value of St was higher than the value predicted by Porteous et al. (2015) [33] but close to the data reported by Ong et al. (2009), Pang et al. (2016) [34] and Janocha et al. (2021) [35]. To sum up, a general agreement with the published data could be achieved by the present numerical model. Therefore, the numerical model could be used for further investigation of the instantaneous flow structures and hydrodynamic properties around tandem cylinders. An example of the mesh used in the study for two tandem cylinders for $L/D = 3$ is shown in Figure 3.3. The mesh of the near cylinder wall region was refined to accurately predict the flow features in that area. Mesh distribution around the cylinders could be described by P_C and P_R parameters, which are presented in Figure 3.3b. The value $P_C = 220$ is the total number of points in circumferential direction along the cylinder surface and $P_R = 41$ is the number of nodes in radial orientation.

Table 3.2. Numerical and experimental data of a fixed single cylinder at high Reynolds number regime.

| Source/Author	Method	Re	$\bar{C}_D$	$C_{L,rms}$	St
Present study	2D URANS $k - w$ SST	3.6×10^6	0.4706	0.1599	0.3293
Ong et al. (2009) [2]	2D URANS $k - \varepsilon$	3.6×10^6	0.4573	0.0766	0.3052
Porteous et al. (2015) [33]	2D URANS $k - \omega$ SST	3.6×10^6	0.4206	-	0.1480
Pang et al. (2016) [34]	2D URANS $k - \omega$ SST	5.2×10^6	0.4570	0.1847	0.3210
Janocha et al. (2021) [35]	2D URANS $k - \omega$ SST	3.6×10^6	0.4616	0.1750	0.3204
Jones et al. (1969) [36]	Experiments	$(0.5 - 8) \times 10^6$	0.15-0.54	-	-
Shih et al. (1993) [37]	Experiments	$(1 - 5) \times 10^6$	0.16-0.50	-	-
Schmidt (1996) [38]	Experiments	$(0.3 - 8) \times 10^6$	0.18-0.53	-	-
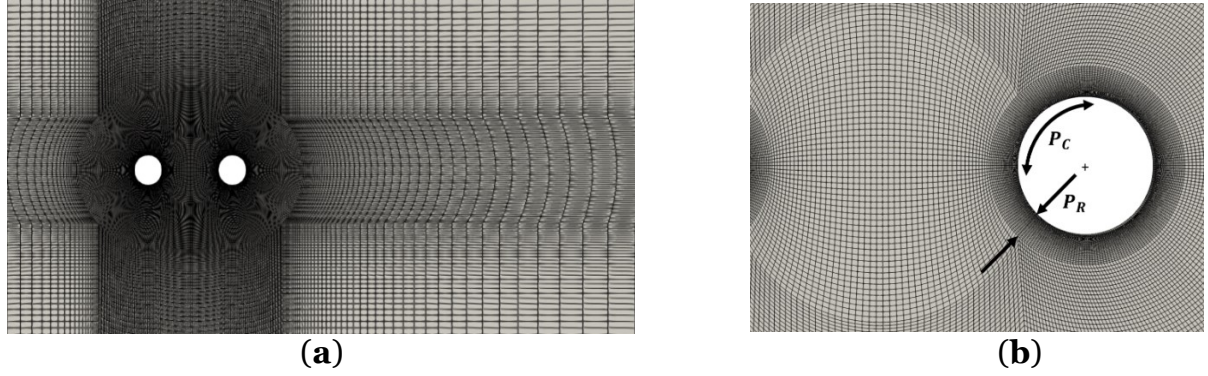
Figure 3.3. An example of the mesh for $L/D = 3$ (**a**) an overview of the mesh (**b**) a zoom-in view in the gap region.

3.3. Results

The effect of the center-to-center offset between two cylinders on the instantaneous flow structures, hydrodynamic quantities and St were analyzed for $L/D = 1.56, 1.8, 2.5, 3, 3.7, 4$. Furthermore, DMD was applied to the velocities and pressure data in the 2D XY-plane flow field to extract the spatiotemporal information of the coherent flow structures in the wake regions of the UC and DC.

3.3.1. Hydrodynamic forces

The hydrodynamics forces are analysed in this section in terms of the instantaneous drag and lift coefficients of the two tandem cylinders.

Figure 3.4 presents the time histories of C_L and C_D for $L/D = 1.56, 1.8, 2.5, 3, 3.7$ and 4 . As seen from Figure 3.4, the C_D oscillated at a frequency which was twice the C_L of the cylinders. The pressure distribution around the cylinder underwent a periodic change as the vortex shedding grew, resulting in periodic variation in the force. The drag force was always positive due to the stagnation point at the front surface of the cylinders, in comparison with the lift force which could be positive and negative. Two vortices of almost equal strength and opposite signs were shed each oscillation period in the wake of a cylinder. Each vortex contributed to the maximum positive value of C_D and contributed to the maximum values with opposite signs of C_L. Therefore, two positive peaks of the C_D and two negative and positive peaks per one cycle of vortex shedding were seen. It resulted in a period doubling of the C_D compared to the oscillation of the C_L.
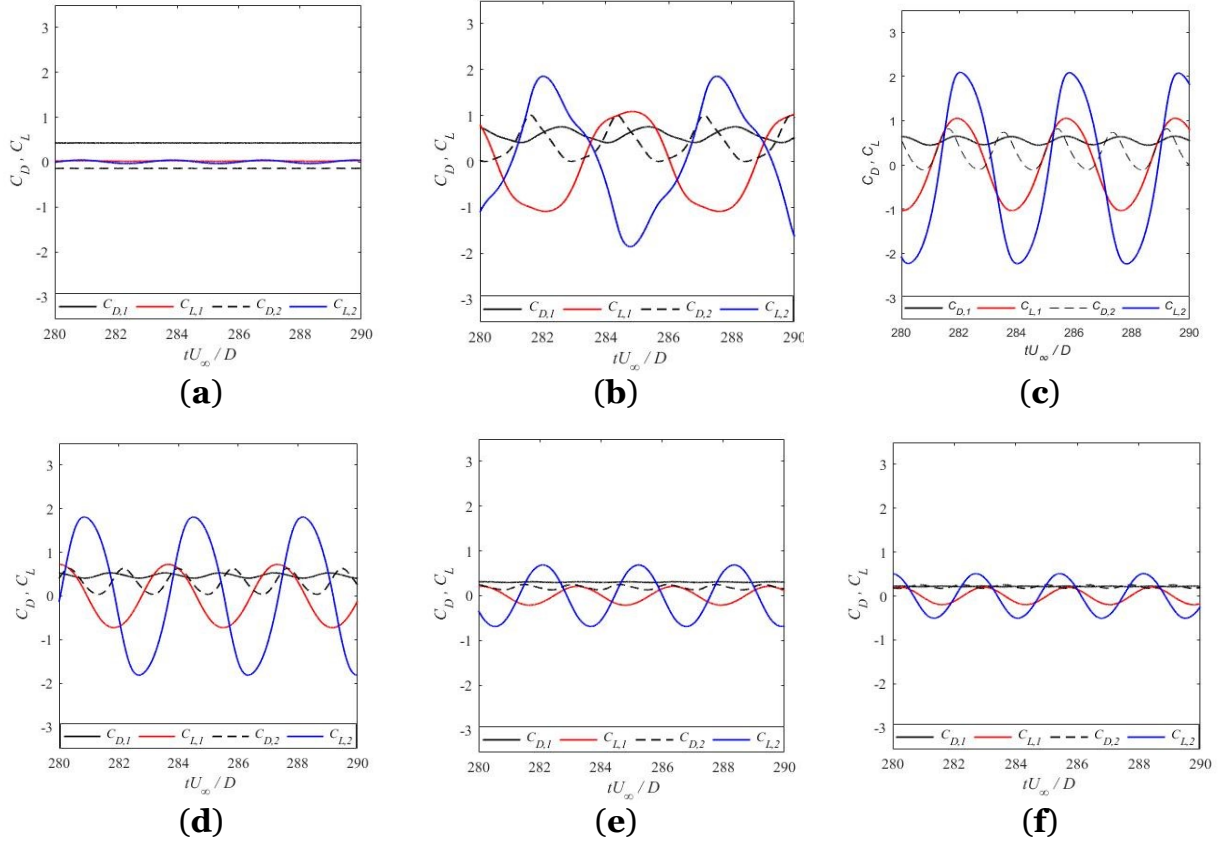
Figure 3.4. Time histories of C_L and C_D for different distance ratios: (**a**) $L/D = 1.56$, (**b**) $L/D = 1.8$, (**c**) $L/D = 2.5$, (**d**) $L/D = 3$, (**e**) $L/D = 3.7$, (**f**) $L/D = 4$.

According to Figure 3.4, the value of C_D of the UC increased when the distance between UC and DC reduced. In contrast, the value of C_D for the DC underwent a nonmonotonic change with shortening of the space between the two cylinders due to shielding effect. At $L/D = 1.56$, C_D of the DC was negative, as presented in Figure 3.4a. This was related to the cavity flow in the gap between UC and DC. In addition, C_D fluctuation amplitude of the DC was higher in comparison with the UC for distance ratios $L/D = 1.8, 2.5, 3, 3.7$ and 4, as shown in Figure 3.4. The UC shear layers reattached to the DC surface and contributed to the pressure distribution around the DC. However, at $L/D = 1.56$, the values of C_D of the UC and DC were approximately constant, as shown in Figure 3.4a. A possible reason was that the shear layers of the UC overshot the DC. Therefore, the two cylinders behaved as an extended body at $L/D = 1.56$.

According to Figure 3.4b–d, the fluctuation amplitudes of C_L were large in comparison with other cases. This might have been connected with the reattachment

flow regime which triggered strong interaction of shear layers between UC and DC. A small angle of the UC shear layers reattachment to the front part of the DC caused strong vortex shedding behind the DC, and vice versa, which influenced the values of C_L. In addition, at $L/D = 1.8$, the shape of the oscillating time history of C_L was not sinusoidal, which indicated a strong modulation of the C_L for both cylinders, as shown in Figure 3.4b. For $L/D = 3.7$ and 4, the fluctuation amplitudes of C_L were smaller in contrast to $L/D = 1.8, 2.5$ and 3. The reason might have been connected with a change of the flow pattern around the tandem cylinders caused by the increasing distance between the two cylinders.

Table 3.3 represents the values of $C_{L,rms}$ and $\overline{C_D}$ for different distance ratios. According to Table 3.3, the value of the $\overline{C_D}$ of the DC was smaller in comparison with UC for all distance ratios. The DC was located in the wake region of the UC. Therefore, the shielding effect caused by the UC influenced the flow pattern around the DC. However, the values of $\overline{C_D}$ of the DC achieved maximum values at $L/D = 1.8$ and 3, as presented in Table 3.3. This might have again been connected with the transitions of the instantaneous flow structures between $L/D = 1.8$ and $L/D = 2.5$, and $L/D = 2.5$ and $L/D = 3$.

Table 3.3. The values of $C_{L,rms}$ and $\overline{C_D}$ for different distance ratios.

L/D	$C_{L,rms}$		$\overline{C_D}$	
	UC	DC	UC	DC
1.56	0.0271	0.0283	0.4279	−0.1376
1.8	0.8352	1.1848	0.5845	0.3969
2.5	0.7512	1.5898	0.5456	0.2740
3	0.5234	1.3160	0.4707	0.3106
3.7	0.1447	0.4911	0.3031	0.1875
4	0.1394	0.3580	0.2169	0.2120

As shown in Table 3.3, the values of the $C_{L,rms}$ for both UC and DC became large when the distance between two cylinders reduced. At $L/D = 2.5$, the value of the $C_{L,rms}$ of the DC achieved a maximum value. This might have been related to the dominance of the front reattachment (FR) flow regime, which caused strong vortex shedding behind the DC. However, the value of the $C_{L,rms}$ of both cylinders decreased drastically at $L/D = 1.56$. The possible reason was that the overshoot flow regime dominated at $L/D = 1.56$ and the interaction of UC and DC shear layers was minimized.

Figure 5 shows the mean pressure coefficient around the UC and DC for $L/D = 1.56$. According to Figure 3.5, the front surface of the DC had a low negative pressure, which was almost the same as the corresponding value of the base pressure of the UC. This fact was an indication that the flow in the gap between UC and DC was almost stagnant. Furthermore, the negative pressure coefficient on the front side of the DC exceeded that on its back surface. Therefore, the DC experienced a negative drag force.
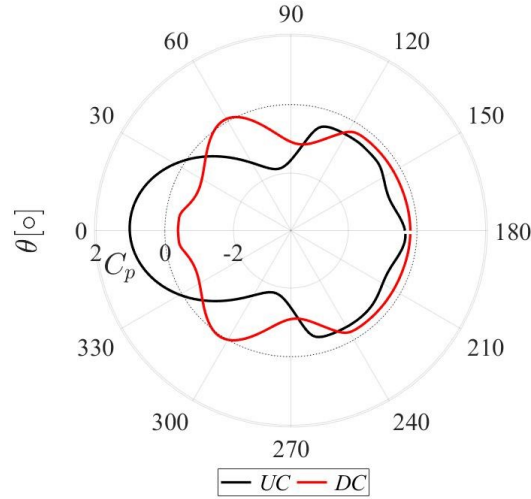

Figure 3.5. The pressure coefficient distribution for $L/D = 1.56$. $c_p = (\bar{p} - p_0)/(\frac{1}{2}\rho U^2)$, where p_0 is the pressure in the far field.

3.3.2. Strouhal Number and Flow Structures

The relationship between St and flow structures around tandem cylinders is analysed in this section. Figure 3.6 presents the PSD (Power Spectral Density) functions $E_{C_{L_1}}$ and $E_{C_{L_2}}$ of C_L for $L/D = 1.56, 1.8, 2.5, 3, 3.7$ and 4 of the UCs and DCs, respectively. For all considered cases, the values of St, and its harmonics of the DC, dominated at the same frequency as measured for the UC. This was explained by Meyer et al. (2011) [39] as follows: when L/D is less than 8 the vortices of the UC can trigger the vortex shedding from the DC, leading to a lock-in of UC and DC vortex shedding.

According to Figure 3.6a,b, the value of St decreased from 0.336 to 0.180 when L/D increased from 1.56 to 1.8. The decrease was connected to change in the flow structure. Instantaneous contours of the spanwise vorticity for $L/D = 1.56$ are presented in Figure 3.7a. At $L/D = 1.56$, where over-shoot flow regime dominated, as shown in Figure 3.7a, the value of St was close to that of an isolated cylinder (≈ 0.329,

as presented in Table 3.2). When the over-shoot regime dominated, the DC was located inside the recirculation region behind the UC. The separated shear layers of the UC overshot the DC without reattachment before rolling up into a Karman vortex street, as shown in Figure 3.7a. Therefore, only one St was observed, shown in Figure 3.6a.
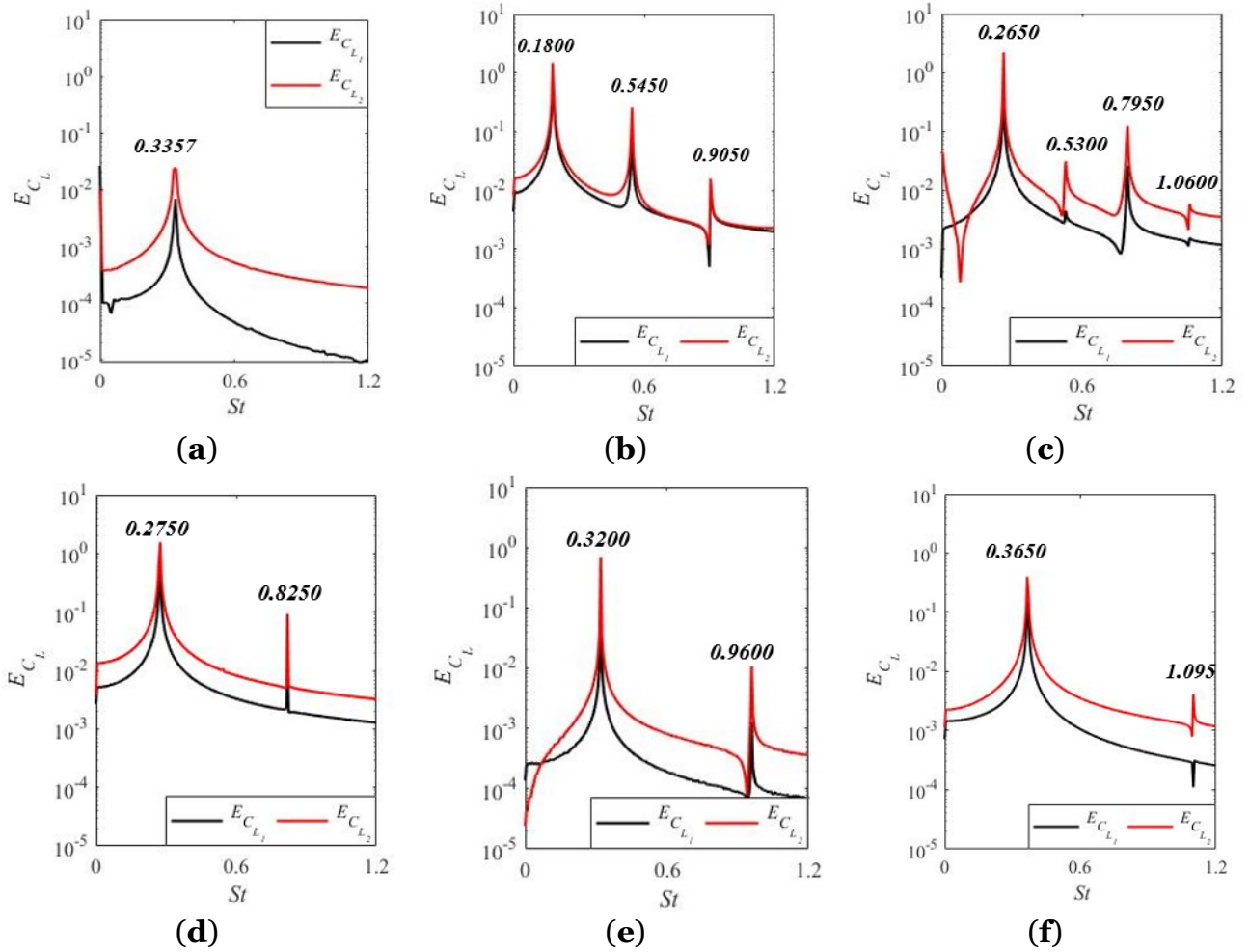

Figure 3.6. The PSD $E_{C_{L_1}}$ and $E_{C_{L_2}}$: (**a**) $L/D = 1.56$, (**b**) $L/D = 1.8$, (**c**) $L/D = 2.5$, (**d**) $L/D = 3$, (**e**) $L/D = 3.7$, (**f**) $L/D = 4$.
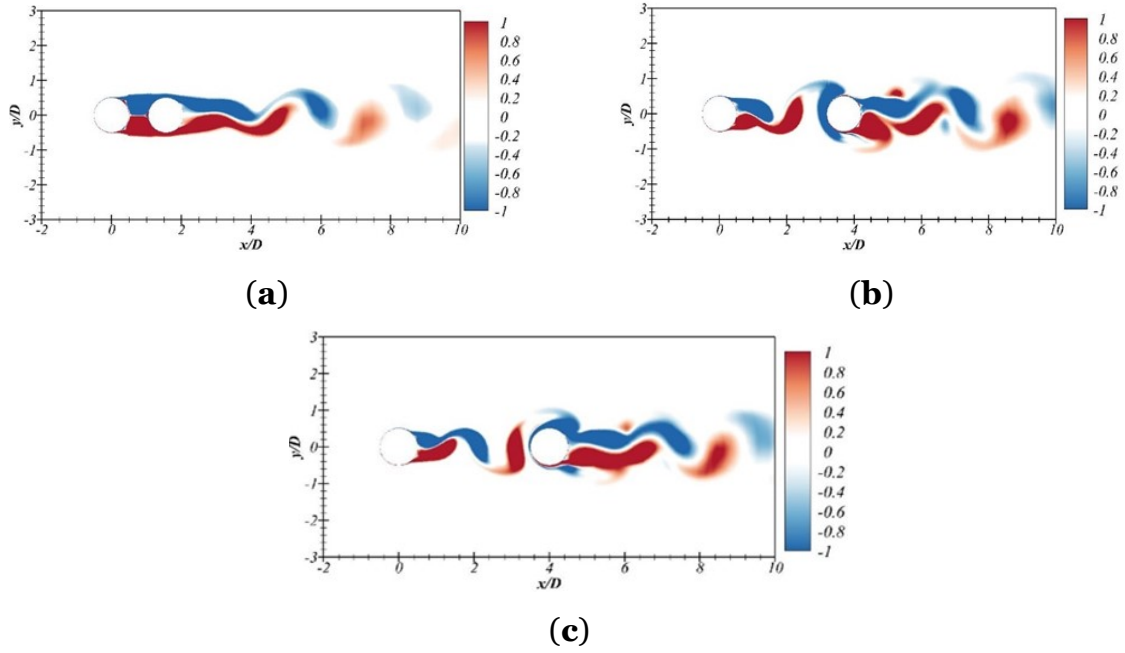
Figure 3.7. Instantaneous contours of the spanwise vorticity for (**a**) $L/D = 1.56$; (**b**) $L/D = 3.7$; (**c**) $L/D = 4$.

The spanwise vorticities for $L/D = 1.8$ at different time steps are shown in Figure 3.8. Meyer et al. (2011) [39] suggested a division of the cylinder surface to the following zones: front ($\theta = 0°{\sim}60°$), front-side ($\theta = 60°{\sim}90°$), rear-side ($\theta = 90°{\sim}120°$) and rear ($\theta = 120°{\sim}180°$) (θ is presented in Figure 3.9). According to the surface division, front-side reattachment regime dominated at $L/D = 1.8$, as shown in Figure 3.8a. Three peaks, including the third and fifth harmonics of St, were observed in the PSD, as shown in Figure 3.6b at $L/D = 1.8$. The first St was connected to the vortex shedding. The multiple peaks in the PSD were due to the reattachment of the shear layer on the DC. The lower shear layer of the UC reattached on the upper part of the DC at the front-side surface, as seen in Figure 3.8a. Then, the reattached shear layer split into two vortex slices going through the lower and upper part of the DC. The upper reattached vortex slice went to the upper side of the DC and further separated from its surface. It did not seem to influence the negative vortex behind the DC, as shown in Figure 3.8b. At the same time, a positive vortex began to grow and was about to move up, as denoted by the arrow in Figure 3.8b. Then, this positive vortex would go down to merge the split reattached vortex slice from the UC, as shown in Figure 3.8c. This flow pattern also happened with the opposite vortex signs, as shown in Figure 3.8d, and this might have been associated with the third harmonic of St, in Figure 3.6b.
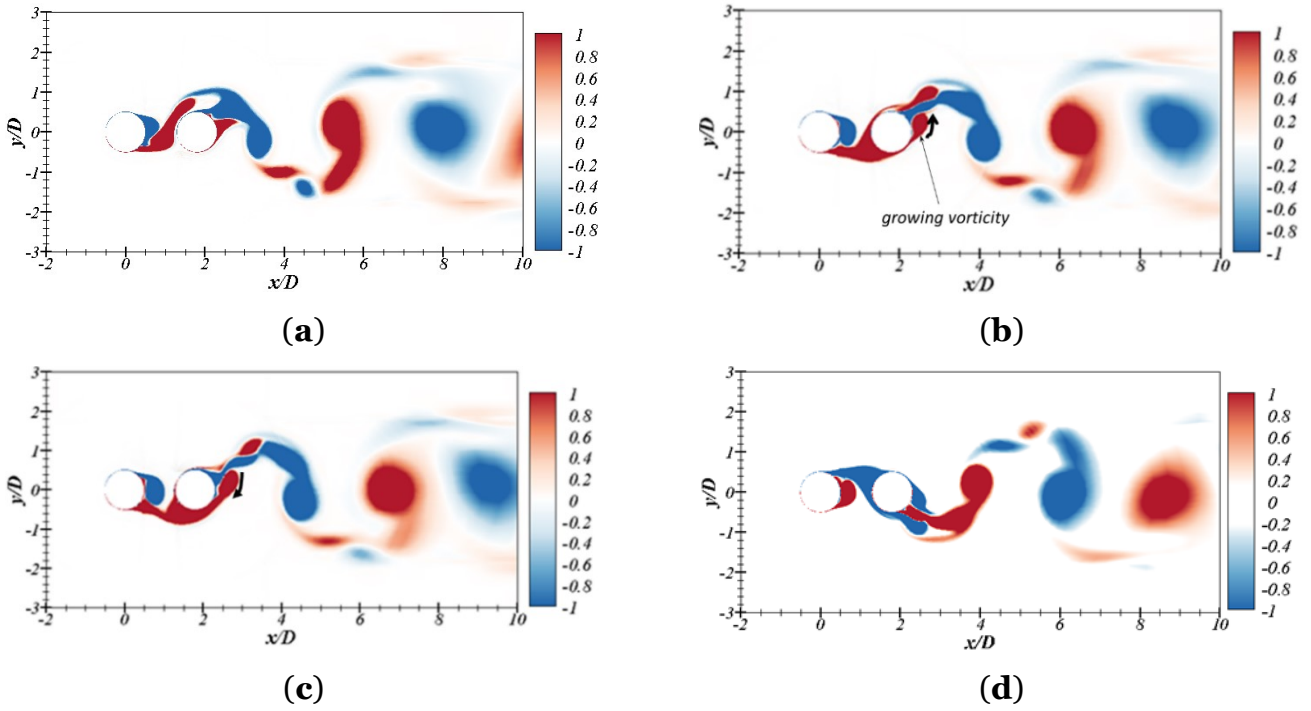
Figure 3.8. Instantaneous contours of the spanwise vorticity for $L/D = 1.8$ at: **(a)** $tD/U_\infty = 278.5$, **(b)** $t\,D/U_\infty = 279.5$, **(c)** $tD/U_\infty = 280$, **(d)** $tD/U_\infty = 282$.
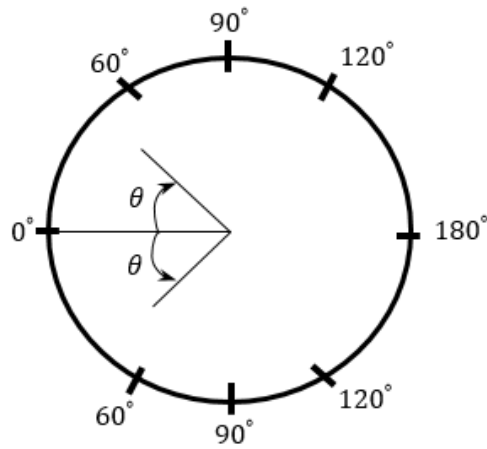
Figure 3.9. The division of the cylinder surface to the zines depending on the angle θ.

Four peaks, including the second, third and fourth harmonics of St, were observed in the PSD, as shown in Figure 6c at $L/D = 2.5$. As shown in Section 3.3.1, $C_{L,rms}$ of the DC achieved a higher value at $L/D = 2.5$, compared with $L/D = 1.8$ and 3. It meant that the shear layers reattached on the surface of the DC at a smaller θ at $L/D = 2.5$ in comparison with that for $L/D = 1.8$ and 3. Therefore, the flow pattern changed from front-side reattachment (FSR) to FR at $L/D = 2.5$. The spanwise vorticities for $L/D = 2.5$ at different time steps are shown in Figure 3.10. According to

Figure 3.10a, the shear layer of the UC reattached on the front surface of the DC at $L/D = 2.5$ and divided into the upper and lower vortex slices. The upper vortex slice would interact with the negative vortex shedding from the DC, as shown in Figure 3.10b. At the exact same time, a positive vortex began to grow behind the DC and also moved up to interact with the negative vortex, as denoted by the arrow in Figure 3.10b. This interaction between three vortices might have been associated with the second harmonics of St, as shown in Figure 3.6c. Then, after the negative vortex separated, the positive vortex behind the DC went down and merged with the reattached lower positive vortex slice from the UC, as shown in Figure 3.10c. The flow pattern was the same as that shown for $L/D = 1.8$ and occurred with the opposite vortex signs, as shown in Figure 3.7d. Again, this flow pattern was related to the third harmonics of St.
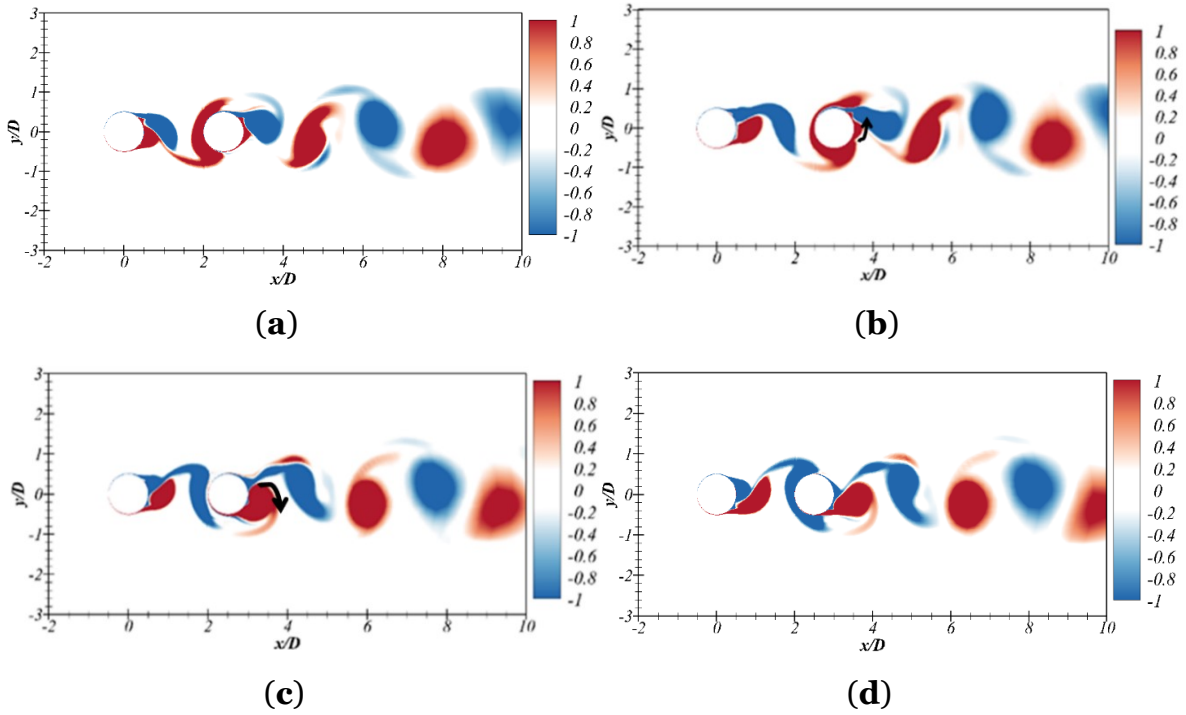
Figure 3.10. The contours of the spanwise vorticities for $L/D = 2.5$: (**a**) $tD/U_\infty = 279.5$; (**b**) $tD/U_\infty = 281$; (**c**) $tD/U_\infty = 280$; (**d**) $tD/U_\infty = 281$.

At $L/D = 3$, two peaks, including the third harmonic of St, were observed in the PSD, as shown in Figure 6e. At $L/D = 3$, the flow pattern changed from FR to the FSR. This was indicated by the decreasing $C_{L,rms}$ at $L/D = 3$ in comparison with $L/D = 2.5$. The reason was that at $L/D = 3$, the shear layers reattached to the surface of the DC at a bigger θ compared to those at $L/D = 2.5$ and produced weaker Karman vortices

behind it. A detailed development of vorticity structures for $L/D = 3$ at different time steps is shown in Figure 3.11.

The lower shear layer of the UC reattached on the front-side surface of the DC, as presented in Figure 3.11a. After that, the reattached shear layer split into two into two vortex slices moving through the lower and upper parts of the DC, as shown in Figure 3.11b. The upper vortex slice went upper side of the DC and then separated from its surface. It seemed that the upper vortex slice did not contribute to the development of the negative vortex behind the DC, as shown in Figure 3.11b. Simultaneously, the positive vortex was growing and moving up, as depicted by the arrow in Figure 3.11b. Furthermore, the positive vortex would move down and merge with the lower vortex slice from the reattached shear layer of the UC, as presented in Figure 3.11c, and this might have been associated with the third harmonic of St in Figure 3.6d. This flow pattern also repeated with the opposite vortex signs, as shown in Figure 3.11d. Therefore, the evolution of the flow pattern around tandem cylinders at $L/D = 3$ was similar to the development of the vortical structures around UC and DC at $L/D = 1.8$.
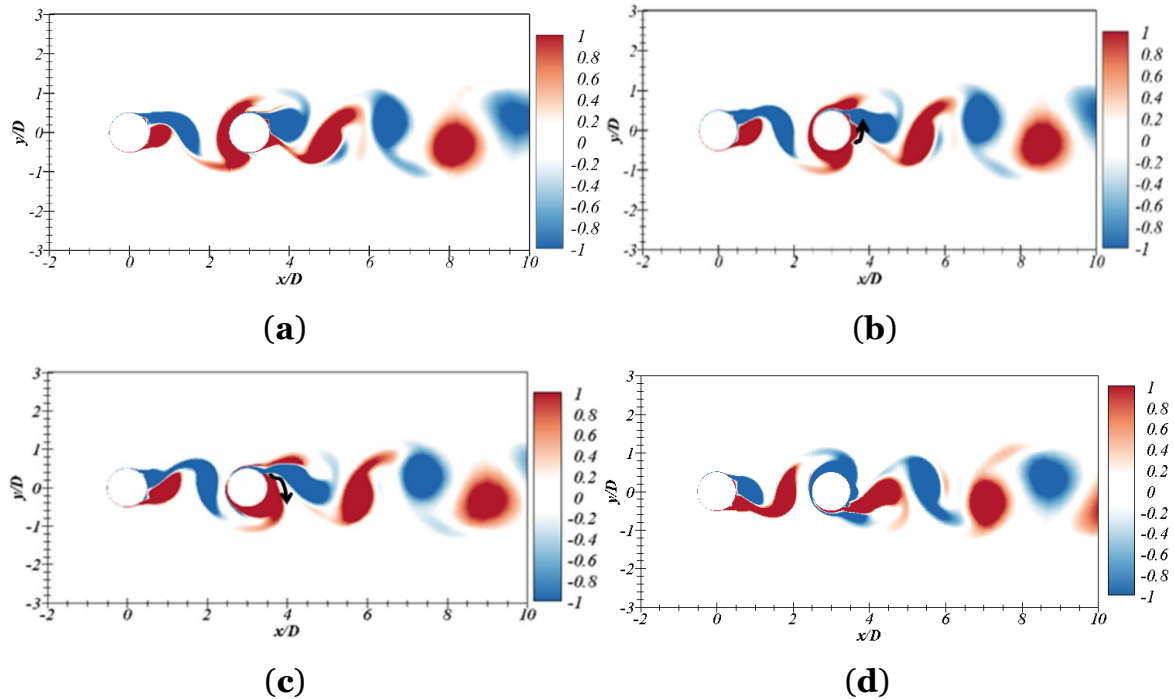

Figure 3.11. Instantaneous contours of the spanwise vorticity for $L/D = 3$ at: **(a)** $tD/U_\infty = 285.5$; **(b)** $tD/U_\infty = 286$; **(c)** $tD/U_\infty = 287$; **(d)** $tD/U_\infty = 288$.

St was again about 0.329 for $L/D = 3.7$, indicating that the flow pattern changed. Alam et al. (2011) proposed that at $Re = 9.7 \times 10^3$ and $Re = 6.5 \times 10^4$ a bi-stable

regime exists between the FR and co-shedding flows at the distances of $3.5 < L/D <$ 3.9 and $3.9 < L/D < 4.2$, respectively. Therefore, it could be concluded that $L/D = 3.7$ and 4, shown in see Figure 3.7b,c belonged to the bi-stable flow regime as the present investigation was performed for $Re = 3.6 \times 10^6$. In line with Figure 3.6e,f, two peaks were observed in the PSD. The second peak, which was characterized by a small amplitude, was the third super-harmonic of the first one. The influence of the third super-harmonic was negligible for $L/D = 3.7$ and 4.

Figure 3.12 presents the time-averaged flow streamlines and pressure field. The cavity flow indicated by the strong recirculation motions appeared in the gap between the two cylinders, as shown in Figure 3.12a. The low pressure at the surface of the DC caused a dramatic change in its $\bar{C}_D$, which has been explained in Section 3.3.1. According to Figure 12b,c, the two recirculation motions behind the DC disappeared, resulting in an attached flow around the DC for $L/D = 1.8$ and 2.5. The probable reason was that the high transverse interactions of the shear layers resulted in a delayed separation point, which suppressed the two recirculation motions. However, the recirculation bubbles reappeared for $L/D \geq 3$, as shown in Figure 3.12d–f. A possible reason was that the influence of the UC shear layers was not sufficient to influence the separation point in the boundary layer of the DC. The behaviour of the DC boundary layer became close to that of a single cylinder.
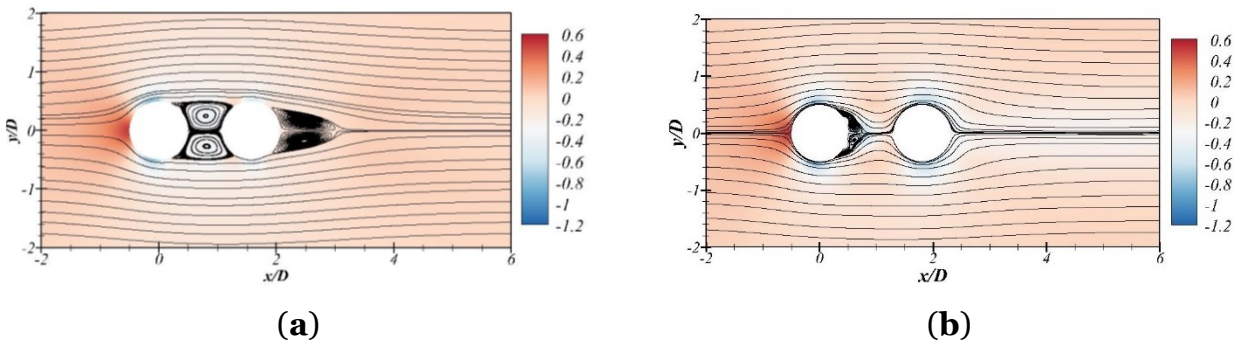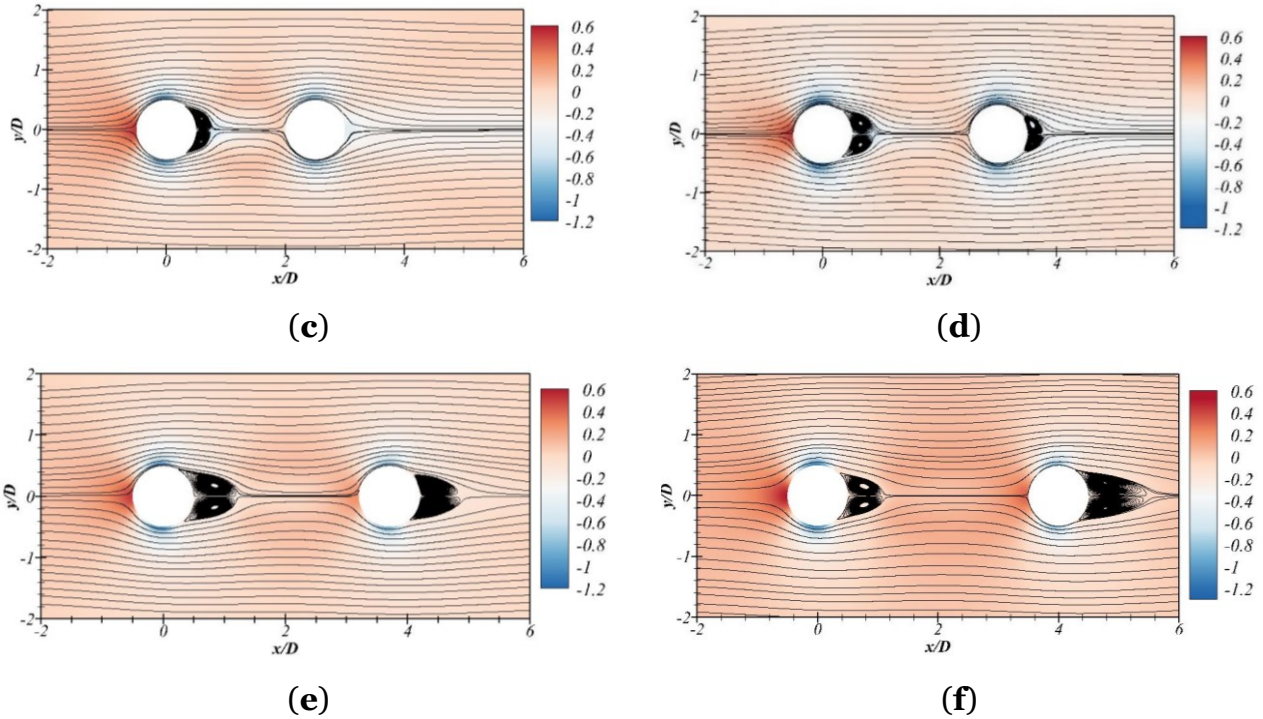

(a)　　　　　　　　　　　　　　　　　　(b)

Figure 3.12. *Cont.*

Figure 3.12. The time-averaged flow streamlines and pressure field for different distance ratios: (**a**) $L/D = 1.56$, (**b**) $L/D = 1.8$, (**c**) $L/D = 2.5$, (**d**) $L/D = 3$, (**e**) $L/D = 3.7$, (**f**) $L/D = 4$.

As a summary, the values of St for different distance ratios are presented in Table 3.4. At $L/D = 1.56$ and 3.7 the value of St was close to that of an isolated cylinder (≈ 0.329). It was related to the change of the flow regime, as discussed previously and presented in Table 3.4. At $L/D = 1.8$, this distance ratio created a longer length of the combined tandem structure which caused a reduction of the St value, compared with that at $L/D = 1.56$. According to Table 3.4, the value of St gradually became close to the value of a single cylinder case with further enlargement of the distance between the two cylinders.

Table 3.4. Summary of the St values and different flow regimes.

L/D	St		Flow Regime
	UC	DC	
1.56	0.3357	0.3357	Overshoot
1.8	0.1800	0.1800	FSR
2.5	0.2650	0.2650	FR
3	0.2750	0.2750	FSR
3.7	0.3200	0.3200	Bi-stable
4	0.3650	0.3650	Bi-stable

3.3.3. Dynamic Mode Decomposition Analysis

The DMD method proposed by Schmid (2010) [40] was implemented in the present study to get a good understanding of the spatial distribution of the coherent structures related to the dominant frequencies, shown in Section 3.3.2. The method allows approximation of the flow fields obtained by numerical simulations or experiments using a linear combination of the DMD modes and further develops a reduced order representation of the dynamical system as:

$$\boldsymbol{\Psi_0} = [\mathbf{u_1}, \mathbf{u_2}, \mathbf{u_3}, \dots, \mathbf{u_N}] \approx \boldsymbol{\Phi} \mathbf{D}_\alpha \mathbf{V}_{\text{and}} =$$

$$[\boldsymbol{\varphi_1}, \boldsymbol{\varphi_2}, \boldsymbol{\varphi_3}, \dots, \boldsymbol{\varphi_N}] \begin{bmatrix} \alpha_1 & \cdots & \cdots \\ \cdots & \cdots & \cdots \\ \cdots & \cdots & \alpha_N \end{bmatrix} \begin{bmatrix} \mu_1^0 & \cdots & \mu_1^{N-1} \\ \vdots & \ddots & \vdots \\ \mu_N^0 & \cdots & \mu_N^{N-1} \end{bmatrix}, \tag{3.17}$$

where $\boldsymbol{\Psi_0}$ is a matrix consisting of flow fields $\mathbf{u_i}$ ($i = 1,2, \dots N$) at each time step and $\mathbf{u_i}$ stores flow data, such as the flow velocities and pressure at each spatial point; $\boldsymbol{\Phi}$ represents the matrix consisting of the spatial DMD modes $\boldsymbol{\varphi}_i$, $\mathbf{D}_\alpha = \text{diag}(\alpha_1, \dots, \alpha_N)$ represents the amplitudes of the corresponding modes within the time span and $\mathbf{V}_{\text{and}}$ denotes the Vandermonde matrix, which contains the temporal variations of each mode during the investigated time span. Schmid (2010) [26] states that $\text{Im}(\log(\mu_i)/\Delta t)$ represents the frequency and $\text{Re}(\log(\mu_i)/\Delta t)$ demonstrates the amplification rate of the mode.

A key problem in the DMD method is the selection of a small subset of DMD modes which can provide a reduced order approximation of the original dynamical system. However, the contribution of each DMD mode to the dynamic system is difficult to quantify, due to the lack of information of its energy obtained through the original DMD algorithm. Therefore, Jovanovic et al. (2014) [40] proposed a sparsity-promoting DMD (SPDMD) method to select a finite number of dynamically important modes within the time span. To achieve this, a positive regularization parameter γ is used to maintain a balance between the approximation error and the number of selected dominant DMD modes. An optimization problem is solved to obtain the unknown elements of the matrix $\mathbf{D}_\alpha$:

$$\min_\alpha \|\boldsymbol{\Psi}_0 - \boldsymbol{\Phi} \mathbf{D}_\alpha \mathbf{V}_{\text{and}}\|_F^2 + \gamma \sum_{i=1}^{N} |\alpha_i|, \tag{3.18}$$

where $\|\ldots\|_F$ is the Frobenius norm of a matrix. Usually, a large value of γ will introduce a high limitation on the number of non-zero elements in $\mathbf{D}_\alpha = \text{diag}(\alpha_1, \ldots, \alpha_N)$. Therefore, the SPDMD algorithm removes the modes which are only of influence for a short time in the early stages of the time evolution and are damped rapidly and also the modes with small amplitudes, as reported in Jovanovic et al. (2014) [40]. As a result, the DMD modes which contribute the most to the dynamic system are retained. Various applications of this method can be found in Yin & Ong (2020, 2021) [41], [42] and Janocha et al. (2021) [35].

The present analysis was performed on the velocity and pressure data obtained in the computational domain. The number of the snapshots was $N = 260$ with a time step of $\Delta t D / U_\infty = 0.5$ for $L/D = 1.8, 2.5$ and 3. The distance ratios were chosen to show how the second and third harmonics of St influenced the mode pattern.

Figure 3.13 shows the DMD eigenvalues for $L/D = 1.8, 2.5$ and 3. The modes which were located inside the unit circle were damped within the temporal evolution of the dynamical system because of their negative growth rate. Most of the eigenvalues lay on the unit circle, indicating that they were 'neutrally stable' with almost zero growth/decay rate. This was because of the statistically stationary state of the wake flow, as reported in Schmid (2010) [26], Jovanovic et al. (2014) [40] and Pan et al. (2015) [43].

(a)   (b)   (c)
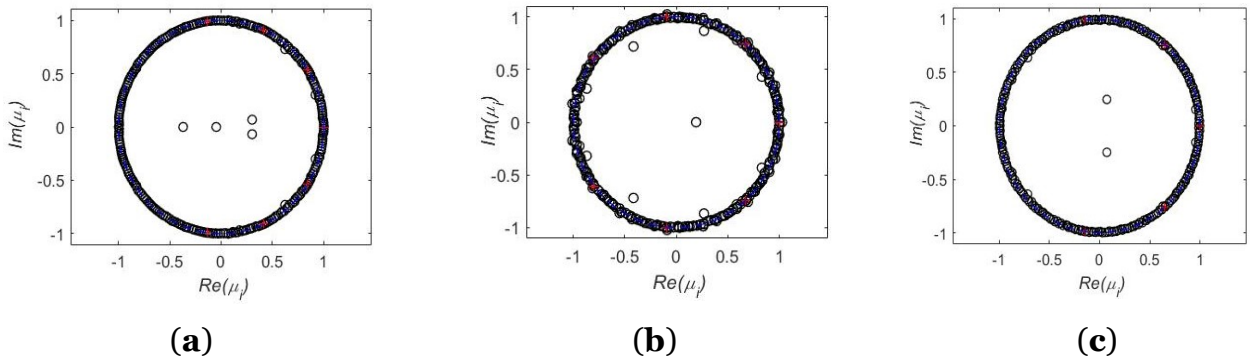
Figure 3.13. The DMD eigenvalues. The black circles denote the eigenvalues obtained using the original DMD and the red crossings denote the eigenvalues obtained using the SPDMD: (**a**) $L/D = 1.8$, (**b**) $L/D = 2.5$, (**c**) $L/D = 3$.

Figure 3.14 shows the DMD spectra obtained using the DMD algorithm and the modes selected by using the SPDMD algorithm. The total number of the selected

modes corresponded to $N_{sp} = 7, 9$ and 7 for $L/D = 1.8, 2.5$ and 3, respectively. According to Figure 3.14, among the chosen modes, by using the SPDMD algorithm, the most dominant mode corresponded to the time-averaged flow with a zero frequency. The rest of the modes determined the large-scale fluctuating flows, which appeared in pairs with positive and negative oscillation frequencies.
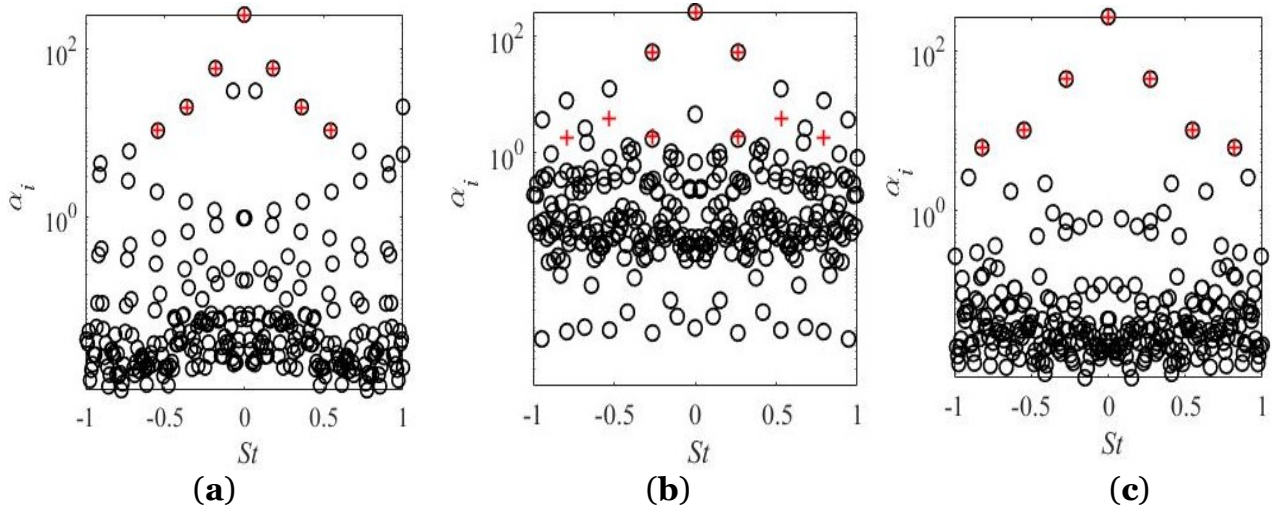

(a)   (b)   (c)

Figure 3.14. The DMD spectrum for different distance ratios. The black circles denote the eigenvalues obtained using the original DMD and the red crossings denote the eigenvalues obtained using the SPDMD: (**a**) $L/D = 1.8$; (**b**) $L/D = 2.5$; (**c**) $L/D = 3$.

Table 3.5 provides the ratios of the energy contribution of the DMD modes selected by using the SPDMD algorithm to the total energy of the system for $L/D = 1.8, 2.5$ and 3. According to Table 3.5, the SPDMD algorithm allowed the capturing of a few of the most dominant modes which contained more than 94% of the system energy and almost reflected the entire spatial distribution of the flow structure in the flow field.

Table 3.5. Energy levels of the DMD modes and their respective contributions to the total energy.

L/D	Mode 1	Mode 2	Mode 3
	Cumulative Energy, %		
1.8	85.70	92.85	95.35
2.5	87.10	93.55	94.02
3	93.60	96.33	98.17

A comparison between the PSD of the C_L of the DC and the DMD spectrum was performed, as indicated in Figure 3.15. Modes chosen by using the SPDMD algorithm could correspond well to the different frequency peaks in the PSD. According to Figure 3.15b, more modes were required to completely reproduce the dynamic information of the coherent flow structures in the wake regions behind both UC and DC for distance ratio $L/D = 2.5$, due to the flow complexity compared with the other two cases. As has been explained in Section 3.2, there are strong interactions between the shear layers with large amplitudes of transverse oscillation behind the UC and DC. Therefore, several peaks were observed in PSD at $L/D = 2.5$.
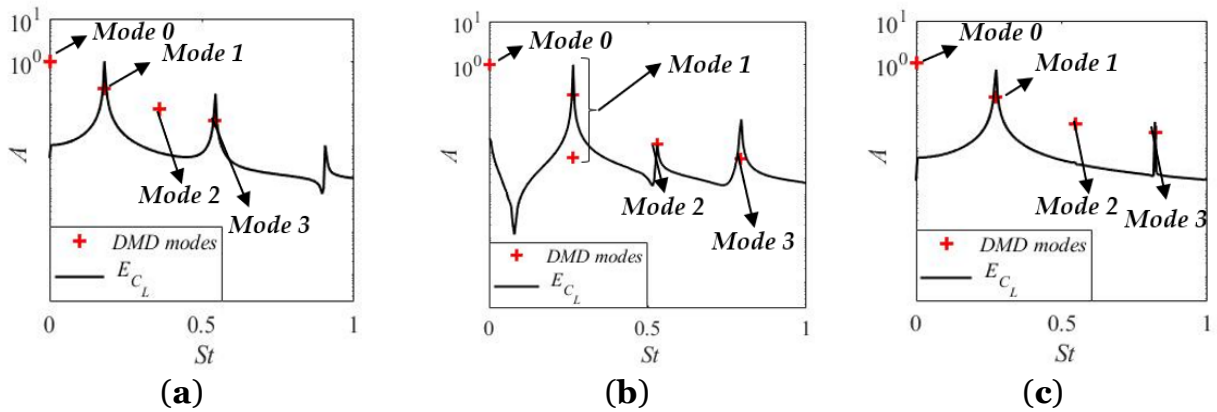

Figure 3.15. The DMD modes obtained by the SPDMD algorithm and the PSD E_{C_L} for DC: (**a**) $L/D = 1.8$; (**b**) $L/D = 2.5$; (**c**) $L/D = 3$.

The modes are supposed to display spatial distribution and length scale features of the flow structures. Figures 3.16, 3.17 and 3.18 show the spatial structures of velocity modes selected by the SPDMD method for $L/D = 1.8, 2.5$ and 3. The streamwise velocities of Modes 1 and 3 revealed a top−bottom mirrored symmetry with respect to the centreline of the cylinders, while the cross-flow velocities displayed asymmetry. The two velocity components of Mode 2 showed reverse symmetry properties compared with Modes 1 and 3. In addition, with the increasing frequency and decreasing amplitude of the higher order modes, the length scale of the structures became smaller. Especially for Mode 3, the energetic streamwise velocity structures were located near the shear layers in the wake regions behind the UC and DC indicating the oscillating features of the shear layers.

Figure 3.16. The spatial distribution of velocities for $L/D = 1.8$: the streamwise velocity for (**a**) Mode 1; (**b**) Mode 2; (**c**) Mode 3 and the cross-flow velocity for (**d**) Mode 1; (**e**) Mode 2; (**f**) Mode 3.

Figure 3.17. Spatial structures of velocities for $L/D = 2.5$: the streamwise velocity for (**a**) Mode 1; (**b**) Mode 2; (**c**) Mode 3 and the cross-flow velocity for (**d**) Mode 1; (**e**) Mode 2; (**f**) Mode 3.
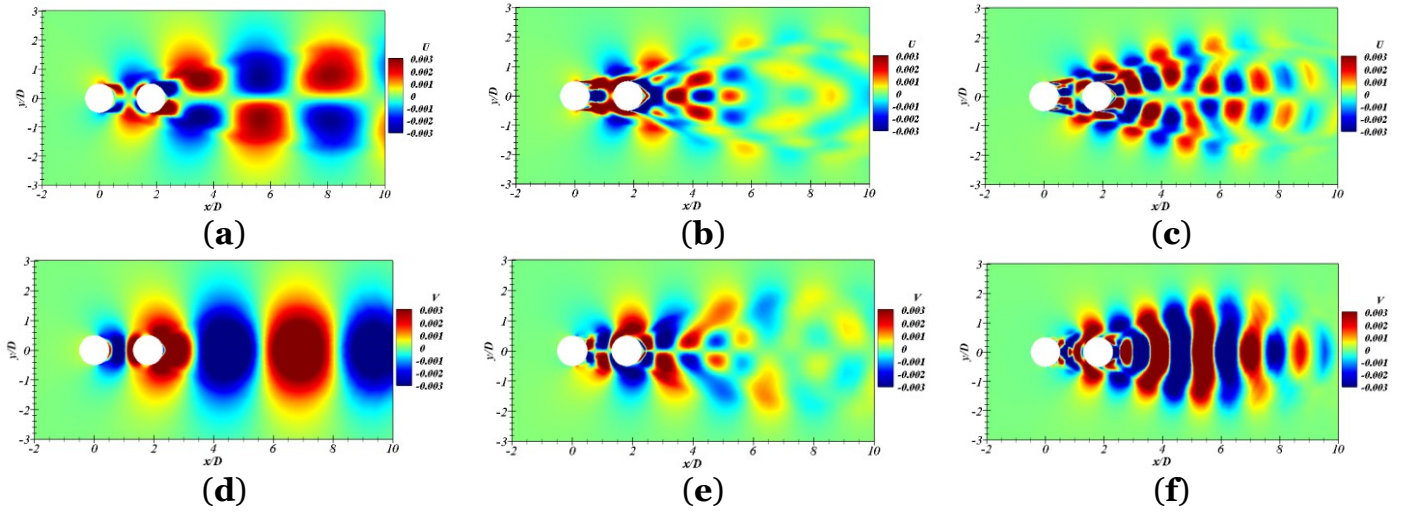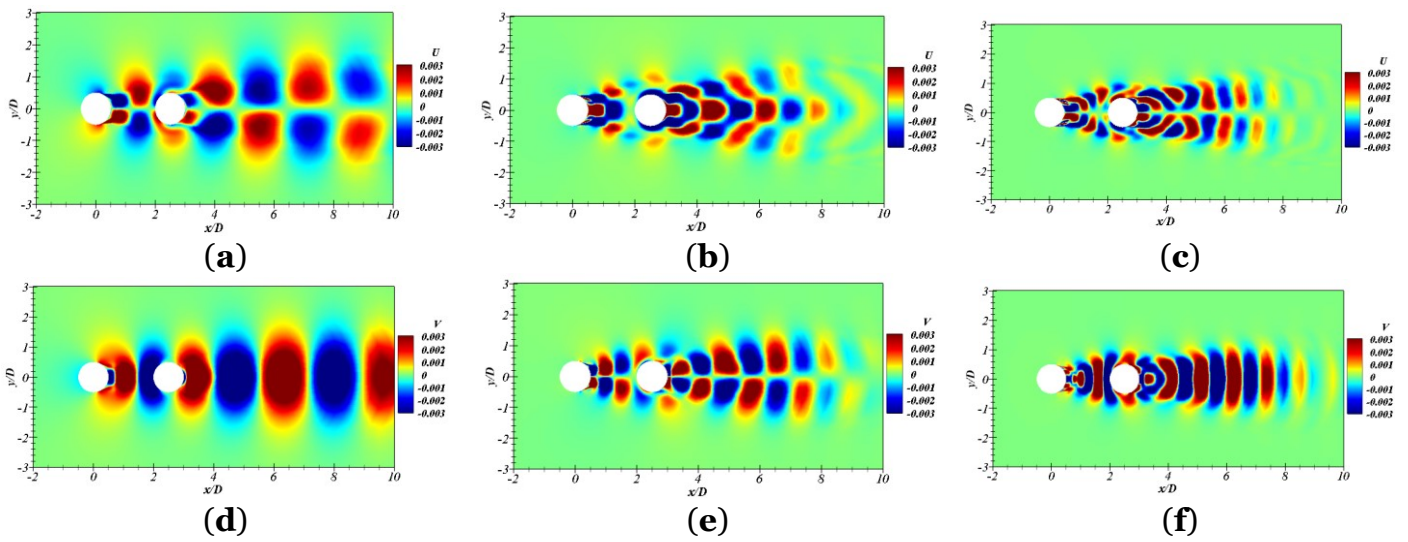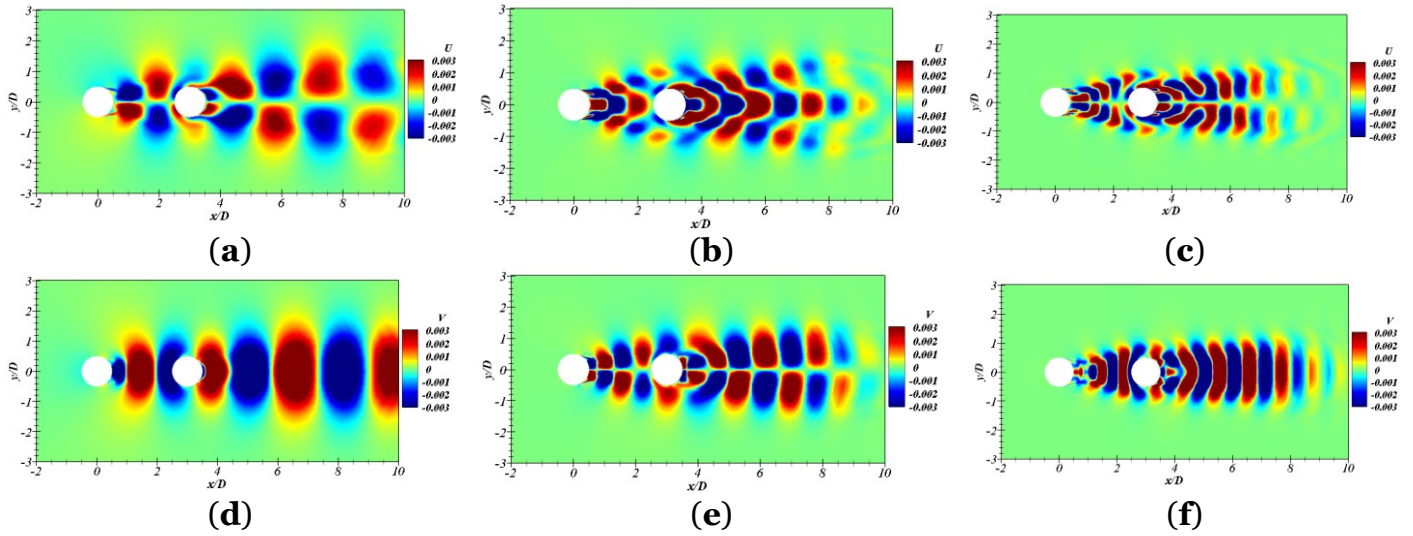
Figure 3.18. Spatial structures of velocities for $L/D = 3$: the streamwise velocity for (**a**) Mode 1; (**b**) Mode 2; (**c**) Mode 3 and the cross-flow velocity for (**d**) Mode 1; (**e**) Mode 2; (**f**) Mode 3.

Figure 3.19 shows the spatial structures of pressure modes selected by the SPDMD method for $L/D = 1.8, 2.5$ and 3. For the pressure distribution of the modes, there were positive and negative regions around the two cylinders, indicating a periodic changing of forces acting on the cylinders. In the cross-flow direction, if the positive and negative regions formed a pair, as indicated by the red circle in Figure 3.19, it would contribute to the lift force at the corresponding frequency of the mode. However, Mode 2 for $L/D = 1.8$ and 3.0 had similar distribution of the pressure, especially around the DC, as shown in Figure 3.19b,h. It had negative pressure regions around both the two sides, which had no contribution to the lift force. Therefore, although Mode 2 was identified by SPDMD, there was no peak in the frequency spectra at the second harmonic of St. For $L/D = 2.5$, on the contrary, there were both positive and negative pressure regions around the DC, which contributed to the lift force at the second harmonic of St.
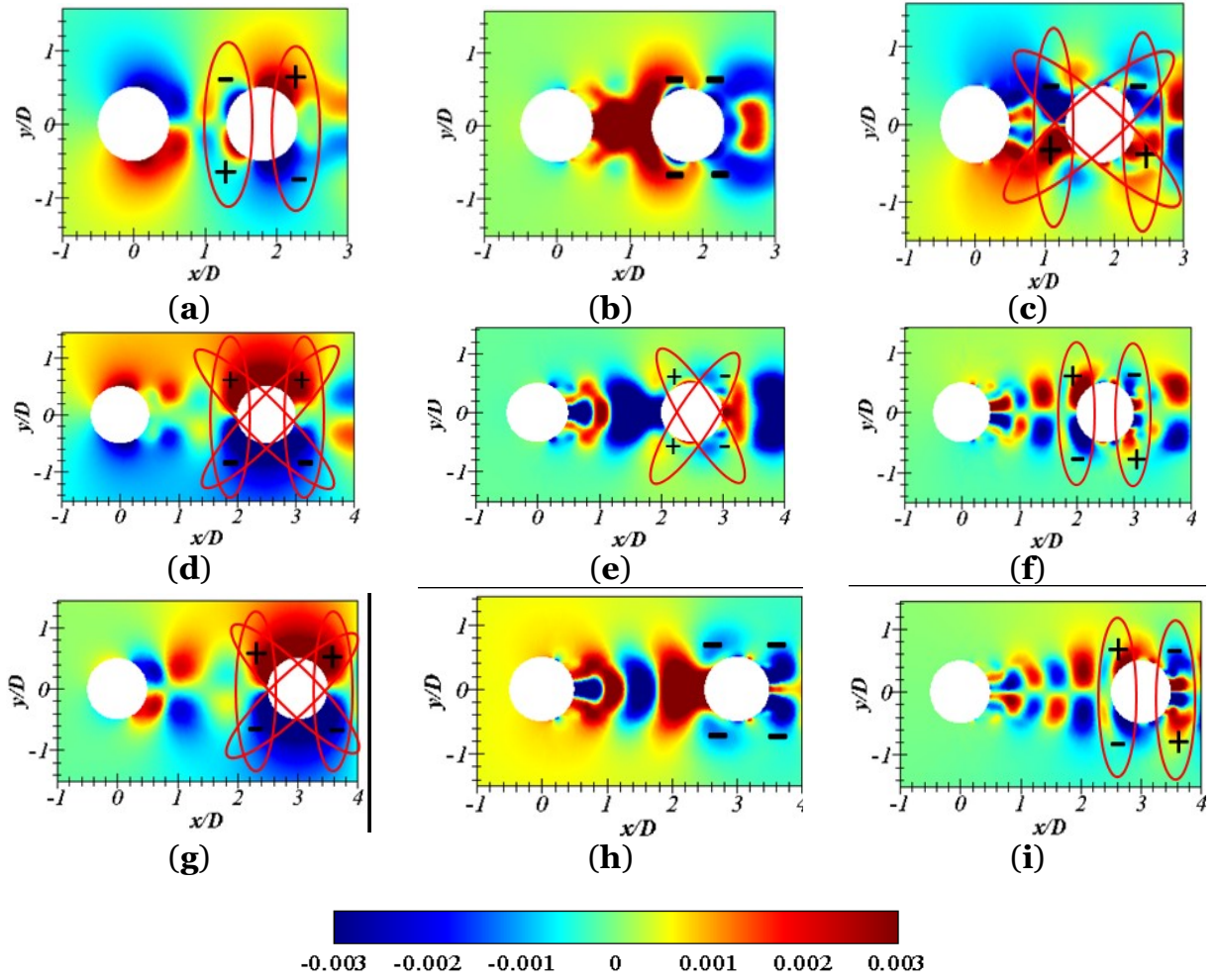
Figure 3.19. The spatial structures of the pressure of Mode 1, Mode 2 and Mode 3 for $L/D = 1.8, 2.5$ and 3: **(a)** Mode 1, $L/D = 1.8$, **(b)** Mode 2, $L/D = 1.8$, **(c)** Mode 3, $L/D = 1.8$; **(d)** Mode 1, $L/D = 2.5$, **(e)** Mode 2, $L/D = 2.5$, **(f)** Mode 3, $L/D = 2.5$, **(g)** Mode 1, $L/D = 3$, **(h)** Mode 2, $L/D = 3$, **(i)** Mode 3, $L/D = 3$.

By using the extracted dominant DMD modes, a reduced-order representation of the flow field could be reconstructed. The snapshots of the vorticity at $\Delta t D / U_\infty = 280$ for the original numerical simulations and reconstructed flow fields are presented in Figure 3.20 for $L/D = 1.8, 2.5$ and 3. The DMD mode shapes, with their corresponding amplitudes and frequencies, obtained by the SPDMD algorithm were used to create the reduced-order representations. The velocity and pressure at a point (x, y) and $t = t_n$ were reconstructed by:

$$u(x, y, t_n) = \sum_{i=1}^{N_{sp}} \alpha_i \varphi_i(x, y) \mu_i^{n-1},$$

(3.27)

46

$$p(x, y, t_n) = \sum_{i=1}^{N_{sp}} \alpha_i \varphi_i(x, y) \mu_i^{n-1}, \qquad (3.28)$$

where N_{sp} is the total number of SPDMD modes. As shown in Figure 3.20, in comparison with the original flow fields, it was evident that the SPDMD method could successfully reconstruct the main flow features, although the investigated flow was complicated at a high Reynolds number. The reconstructed flow field had some differences in the wake region of the DC for $L/D = 2.5$, where there were strong interactions of shear layers in the flow, as shown in Figure 3.20d. The noisy structures in the reconstructed wake flow behind the DC could be removed by including more DMD modes.

Original flow

Reconstructed flow

(a)

(b)

(c)

(d)

Figure 3.20. *Cont.*

(**e**) (**f**)
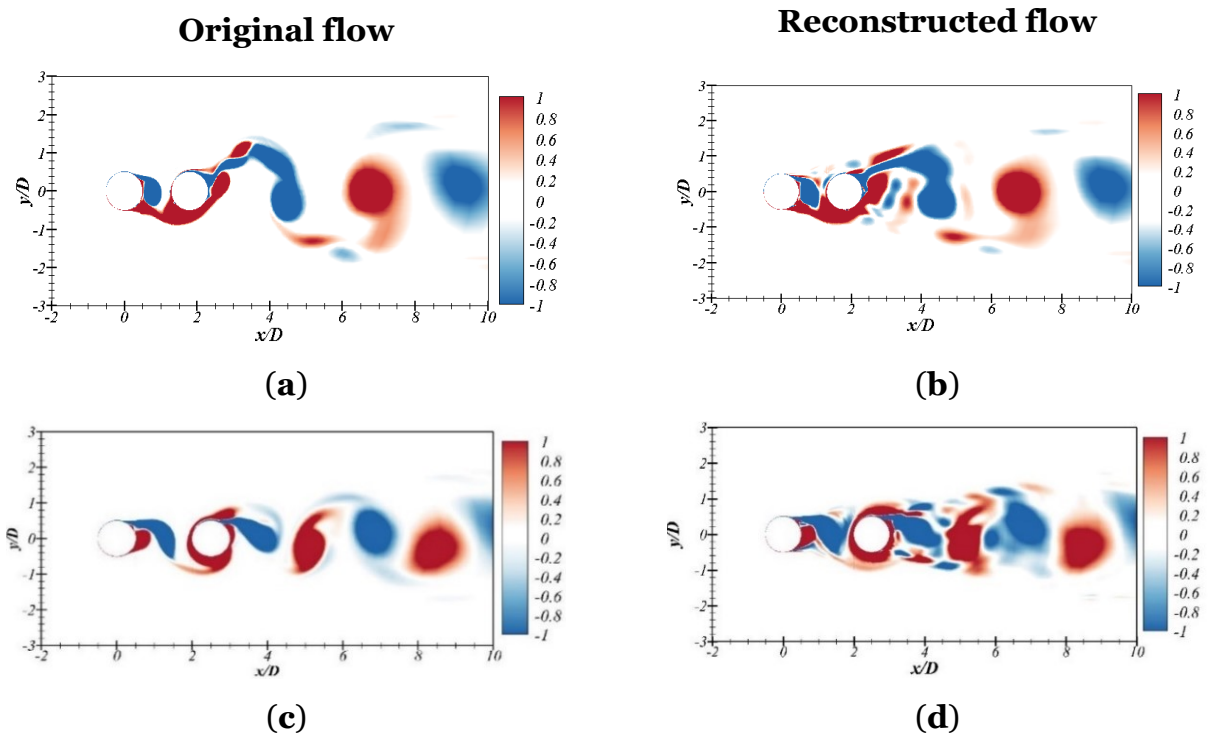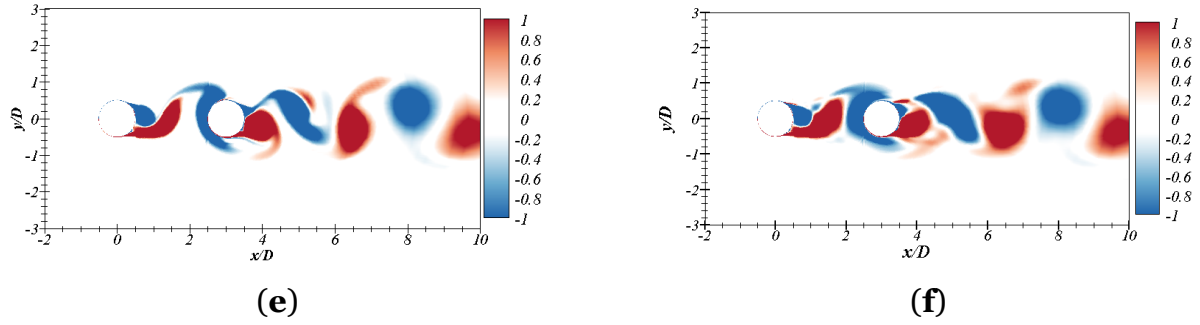
Figure 3.20. A comparison of instantaneous contours of the spanwise vorticity of original simulation and reconstructed flow field using SPDMD modes: (**a**,**b**) $L/D = 1.8$; (**c**,**d**) L/D = 2.5; (**e**,**f**) $L/D = 3$.

Figures 3.21 and 3.22 show the time histories of the lift and drag coefficients of the UC and DC obtained by the numerical simulations and the reduced-order representations. It can be seen that the reduced-order representations with a considerably small number of modes could correctly reproduce the time histories of the lift and drag coefficients. Thus, the frequencies and amplitudes of the dominant DMD modes, which contributed the most to the dynamics, were obtained accurately by the SPDMD algorithm.

(**a**) (**b**) (**c**)

(**d**) (**e**) (**f**)

Figure 3.21. Time histories of (**a**–**c**) the UC lift coefficient and (**d**–**f**) drag coefficient obtained by the simulation results and reconstructed by using the selected DMD modes for $L/D = 1.8, 2.5$ and 3: (**a**,**d**) $L/D = 1.8$; (**b**,**e**) $L/D = 2.5$; (**c**,**f**) $L/D = 3$.

Figure 3.22. Time histories of (**a**–**c**) the DC lift coefficient and (**d**–**f**) drag coefficient obtained by the simulation results and reconstructed by using the selected DMD modes for $L/D = 1.8, 2.5$ and 3: (**a**,**d**) $L/D = 1.8$; (**b**,**e**) $L/D = 2.5$; (**c**,**f**) $L/D = 3$.
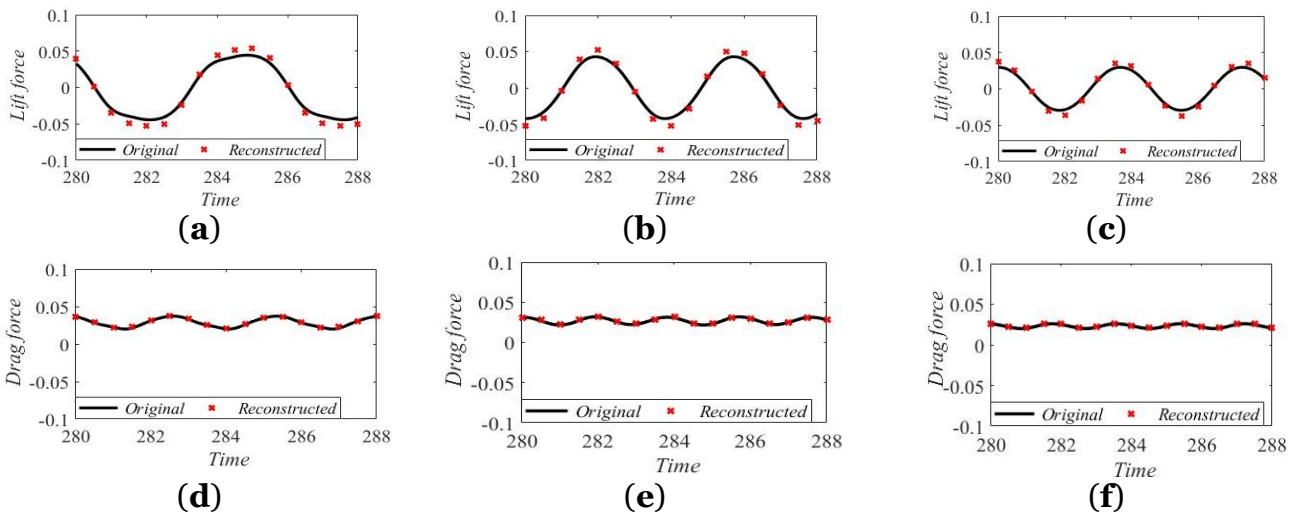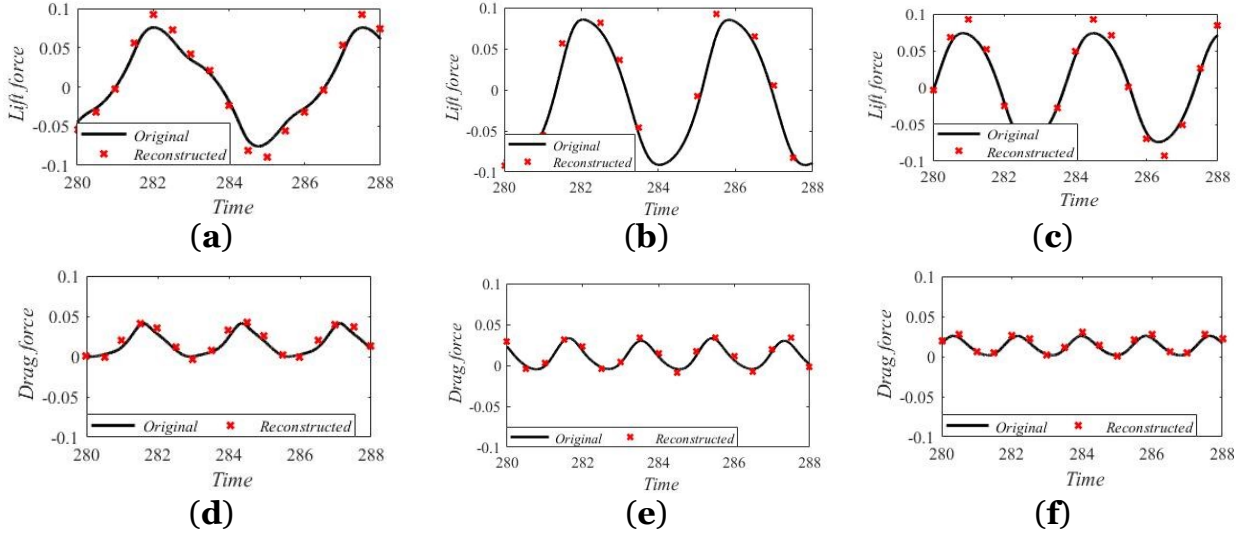
Conclusions

The flow around two tandem cylinders with different horizontal offsets of $L/D = 1.56, 1.8, 2.5, 3, 3.7$ and 4 was investigated numerically at a Reynolds number of 3.6×10^6. The 2D URANS equations with a standard $k - \omega$ SST turbulence model were solved. Verification and validation studies were performed for the flow past a single cylinder and showed that the present numerical model could provide satisfying results compared with the previously published data. Then, the numerical model was used to study the hydrodynamic characteristics of tandem cylinders subjected to high Re incoming flow. Analysis of instantaneous flow structures, hydrodynamic coefficients, St and vortical structures were demonstrated in the present study. In addition, the SPDMD algorithm was implemented to extract dominant modes which contributed the most to the inherent dynamics, and to construct a reduced-order representation of the flow field. The main conclusions can be summarized as follows:

1. With the increasing L/D, flow structures at $Re = 3.6 \times 10^6$ changed in terms of overshoot, FSR, FR, FSR and bi-stable. This relates to the reattachment point of the separated UC shear layers to the surface of the DC.

2. The lower vorticity slice of the reattached shear layer to the surface of the DC contributed to the evolution of the positive vorticity behind the DC. It explains the existence of the third super-harmonic for the cases considered. However, the second

49

harmonic observed in the spectra of the lift forces was only for the case of $L/D = 2.5$. This relates to assistance of the upper vorticity slice of the reattached shear layer to the development of the negative coherent structure behind the DC.

3. The values $C_{L,rms}$, $\overline{C_D}$ and St were influenced by L/D such that $\overline{C_D}$ decreased with a decreasing L/D between two cylinders and achieved a negative value for the DC at $L/D = 1.56$. The negative $\overline{C_D}$ value corresponded to a low pressure at the front surface of the DC caused by the cavity flow between UC and DC at $L/D = 1.56$. Increasing amplitudes of C_L fluctuation were found at $L/D = 2.5$, and this relate to FR flow, which causes significant interaction of shear layers. At $L/D \geq 1.8$, the reattachment flow regime (FR) dominated. It creates a longer after-body length of the combined UC and DC body leading to a sudden reduction of the St value.

4. The SPDMD algorithm was used to extract a few dominant modes which contributed the most to the flow dynamics. It was found that Mode 2 for $L/D = 1.8$ and 3 did not contribute to the lift force. Therefore, there was no peak in the frequency spectra of the lift force at the second harmonic of St for these two cases, although Mode 2 was identified by using SPDMD. In addition, the reduced-order representations of the flow field, which consist of the finite SPDMD modes number, can correctly reconstruct the wake flow at the investigated high Reynolds number.

References

1. Sumer, B.; Fredsøe, J. Hydrodynamics around Cylindrical Structures; World Scientific Publishing Co. Pte. Ltd.: Singapore, **1997**.
2. Ong, M.C.; Utnes, T. Numerical simulation of flow around a smooth circular cylinder at very high Reynolds numbers. *J. Mar. Struct.* **2009**, *22*, 142–153.
3. Nakaguchi, H.; Hashimoto, K.; Muto, S. An experimental study on aero-dynamic drag of rectangular cylinders. *J. Jpn. Soc. Aerospace Sci.* **1968**, *16*, 1–5.
4. Norberg, C. Flow around rectangular cylinders: Pressure forces and wake frequencies. *J. Wind Eng. Ind. Aerodyn.* **1993**, *49*, 187–196.
5. Ohya, Y. Note on a discontinuous change in wake pattern for a rectangular cylinder. *J. Fluids Struct.* **1994**, *8*, 325–330.
6. Okajima, A. Numerical simulation of flow around rectangular cylinders. *J. Wind Eng. Ind. Aerodyn.* **1990**, *33*, 171–180.

7. Tian, X.; Ong, M.C.; Yang, J.; Myrhaug, D. Unsteady RANS simulations of flow around rectangular cylinders with different aspect ratios. *J. Ocean Eng.* **2013**, *58*, 208–216.

8. Dutta, S.; Panigrahi, P.K.; Muralidhar, K. Experimental investigation of flow past a square cylinder at an angle of incidence. *J. Eng. Mech.* **2008**, *134*, 788–803.

9. El-Sherbiny, S. Flow separation and reattachment over the sides of a 90° triangular prism. *J. Wind Eng. Ind. Aerodyn.* **1983**, *11*, 393–403.

10. Nakagawa, T. Vortex shedding mechanism from a triangular prism in a subsonic flow. *J. Fluid Dyn. Res.* **1989**, *5*, 69–81.

11. Cheng, M.; Liu, G.R. Effects of afterbody shape on flow around prismatic cylinders. *J. Wind Eng. Ind. Aerodyn.* **2000**, *84*, 181–196.

12. Tritton, D. Experiments on the Flow past a circular cylinder al low Reynolds numbers. *J. Fluid Mech.* **1959**, *6*, 547–567.

13. Dimopoulos, H.; Hanratty, T. Velocity gradients at the wall for flow around a cylinder for Reynolds numbers between 60 and 360. *J. Fluid Mech.* **2006**, *33*, 303–319.

14. Park, J.; Kwon, K. Numerical solutions of flow past a circular cylinder at Reynolds numbers up to 160. *KSME Int. J.* **1998**, *12*, 1200–1205.

15. Rajani, B.; Kandasamy, A. Numerical simulation of laminar flow past a circular cylinder. *J. Appl. Math. Medel.* **2009**, *33*, 1225–1247.

16. Zdravkovich, M. Review of flow interference between two circular cylinders in various arrangements. *J. Fluids* **1977**, *99*, 618–663.

17. Sumner, D. Two circular cylinders in cross-flow: A review. *J. Fluid Struct.* **2010**, *26*, 849–899.

18. Zdravkovich, M. The effects of interference between circular cylinders in cross flow. *J. Fluids* **1978**, *1*, 239–261.

19. Hori, E. Experiments on flow around a pair of parallel circular cylinders. In Proceedings of the Ninth Japan National Congress for Applied Mechanics, Nagoya, Tokyo, 29 August–1 September 1959; Volume 11, pp. 231–234.

20. Huhe-Aode; Tatsuno, M. Visual studies of wake structure behind two cylinders in tandem arrangement. *Rep. Res. Inst. Appl. Mech.* **1985**, *32*, 1–20.

21. Nishimura, T.; Ohori, Y.; Kawamura, Y. Flow pattern and rate of mass transfer around two cylinders in tandem. *J. Intern. Chem. Engin.* **1986**, *26*, 123–129.

22. Xu, G.; Zhou, Y. Strouhal numbers in the wake of two inline cylinders. *J. Exp. Fluids* **2004**, *37*, 248–256.

23. Alam, A. Two interacting cylinders in cross flow. *J. Phys. Rev. E* **2011**, *84,* 639–654.

24. Catalano, P.; Wang, M.; Iaccarino, G.; Moin, P. Numerical simulation of the flow around a circular cylinder at high Reynolds numbers. *Int. J. Heat Fluid Flow* **2003**, *24*, 463–469.

25. Hu, X.; Zhang, X.; You, Y. On the flow around two circular cylinders in tandem arrangement at high Reynolds number. *J. Ocean Eng*. **2019**, *189*, 106–301.

26. Schmid, P. Dynamic Mode Decomposition of numerical and experimental data. *J. Fluid Mech.* **2010**, *656*, 5–28.

27. Rowley, C.; Mezić, I.; Bagheri, S.; Schlatter, P.; Henningson, D.S. Spectral analysis of nonlinear flows. *J. Fluid Mech.* **2009**, *22*, 142–153.

28. Taira, K.; Brunton, S.L.; Dawson, S.T.; Rowley, C.W.; Colonius, T.; McKeon, B.J. Modal analysis of fluid flows: An overview. *AIAA J.* **2017**, *55*, 4013–4041.

29. Bagheri, S. Koopman-mode decomposition of the cylinder wake. *J. Fluid Mech.* **2013**, *725*, 596–623.

30. Hemati, M.S.; Rowley, C.W.; Deem, E.A.; Cattafesta, L.N. De-biasing the dynamic mode decomposition for applied Koopman spectral analysis of noisy datasets. *Theor. Comput. Fluid Dyn.* **2017**, *31*, 349–368.

31. Schmid, P.; Li, L.; Pust, O. Application of the dynamic mode decomposition. *Theor. Comput. Fluid Dyn.* **2011**, *25*, 249–259.

32. Menter, F.; Kuntz, M.; Langtry, R. Ten years of industrial experience with the SST turbulence model. *J. Heat Mass Transf.* **2003**, *4*, 625–632.

33. Porteous, A.; Habbit, R.; Colmenares, J.; Poroseva, S.; Murman, S.M. Simulations of incompressible separated turbulent flows around two-dimensional bodies with URANS models in OpenFOAM. In Proceedings of the 22nd AIAA Computational Fluid Dynamics Conference 2015, Dallas, TX, USA, 22–26 June 2015.

34. Pang, A.; Skote, M.; Lim, S.Y. Modelling high re flow around a 2D cylindrical bluff body using the k-ω (SST) turbulence model, *J. Prog. Comput. Fluid Dyn.* **2016**, *16*, 48–57.

35. Janocha, M. Numerical simulations of flow-induced vibrations of two rigidly coupled cylinders with uneven diameters in the upper transition Reynolds number regime. *J. Mar. Struct*. **2021**, *105,* 103–332.

36. Jones, G.; Cincotta, J. *Aerodynamic Forces on a Stationary and Oscillating Circular Cylinder at High Reunolds Numbers*; Technical Report TB R-300; NASA: Washington, DC, USA, 1969.

37. Shih, W.C.L.; Wang, C. Experiments on flow past rough circular cylinders at large Reynolds numbers. *J. Wind Eng. Aerodyn.* **1993**, *49*, 351–368.

38. Schmidt, L. *Fluctuating Forcemeasurements upon a Circular Cylinder at Reynolds Number up to 5 × 10⁶*; Technical Report; Langley Research Center: Hampton, VA, USA, 1996.

39. Meyer, J.; Alam, M.M. Reynolds number effect on flow-induced forces on two tandem cylinders. In Proceedings of the International Conference on Mechanical Engineering, Dhaka, Bangladesh, 18–20 December 2011.

40. Jovanović, M.R.; Schmid, P.J.; Nichols, J.W. Sparsity-promoting dynamic mode decomposition. *Phys. Fluids.* **2014**, *26*, 024103.

41. Yin, G.; Ong, M.C. On the wake flow behind a sphere in a pipe flow at low Reynolds numbers. *Phys. Fluids.* **2020**, *32*, 103605.

42. Yin, G.; Ong, M.C. Numerical analysis on flow around a wall-mounted square structure using Dynamic Mode Decomposition. *J. Ocean Eng.* **2021**, *223*, 108–647.

43. Pan, C.; Xue, D. On the accuracy of dynamic mode decomposition in estimating instability of wave packet. *Exp. Fluid.* **2015**, *56*, 164.

Chapter 4.

A Data Driven Reduced Order Model based on Long Short-Term Memory Neural Network for Vortex-Induced Vibrations of a Circular Cylinder.

Anastasiia Nazvanova [a], Muk Chen Ong [a] and Guang Yin (尹光) [a]

[a] Department of Mechanical and Structural Engineering and Material Science, University of Stavanger, N-4036 Stavanger, Norway.

Abstract

A data-driven reduced-order model (ROM) based on long-short-term memory neural network (LSTM-NN) for prediction of the flow past a circular cylinder undergoing two-degree-of-freedom (2DoF) vortex-induced vibration (VIV) in the upper transition Reynolds number regime with different reduced velocities is developed. The proper orthogonal decomposition (POD) technique is utilized to project the high-dimensional spatiotemporal flow data generated by solving the two-dimensional (2D) unsteady Reynolds-averaged Navier-Stokes (URANS) equations to a low-dimensional subspace. The LSTM-NN is applied to predict evolution of the POD temporal coefficients and streamwise and cross-flow velocities and displacements of the cylinder based on the low-dimensional representation of the flow data. This model is referred as POD-LSTM-NN. In addition, the force partitioning method (FPM) is implemented to capture the hydrodynamic forces acting on the cylinder using the surrounding flow field predicted by the POD-LSTM-NN ROM and the predicted time-histories of the lift and drag forces are compared with the CFD simulations.

4.1. Introduction

Investigations of wake flow dynamics behind the circular bluff bodies subjected to high Reynolds number flow has received essential attention during the past decades due to their wide applications in engineering. For example, in the field of offshore engineering, marine risers, power cables, umbilicals, jumpers and pipelines are the examples of the flexible slender bluff bodies which are subjected to high Reynolds number flows. Vortex shedding is one of the commonly observed flow features associated with hydrodynamics of the bluff bodies. For a circular cylinder, shear layers separate from the surface and generate clockwise and counterclockwise vorticities in the wake region. The periodic vortex shedding causes oscillatory lift and drag forces on the bluff body. If a slender structure is flexible or elastically supported, under certain conditions, the vortex-shedding frequency can be synchronized with the natural frequency of the system. This phenomenon is called lock-in which leads to a vortex-induced vibration (VIV) of the body. It is significant to investigate the flow behaviour around the VIV bluff bodies to design devices to mitigate the cyclic loadings and extend fatigue life of the structures. Therefore, extensive studies have been conducted. For example, experiments on VIV of cylinders subjected to a turbulent flow were conducted by Moe et al. (1994) [1], Vikestad (1998) [2], Ding et al. (2004) [3] and Bernitsas & Raghavan (2008) [4]. In addition, numerical studies on VIV bluff body were performed by Hassanpour et al. (2022) [5], Jiang et al. (2023)[6], Verma & De (2022) [7] and Serta et al. (2021) [8] using computational fluid dynamics (CFD). However, investigations of highly chaotic turbulent flows and the flow induced vibration of the structures via the full-order model by numerically solving the Navier-Stokes equations and the equations of structural motions leads to enormous computational costs. Nowadays, one of the most active research topics in the modelling and prediction of the turbulent flows is the development of accurate algorithms with low complexity and reduced computational costs.

The reduced order modelling (ROM) proposes an approach for representing and understanding high-dimensional dynamical systems using a low-dimensional subspace while keeping the relatively high accuracy of the modelling results with a decreasing computational time. There are tremendous number of procedures to build ROM of nonlinear dynamical systems. All these approaches have the common idea to extract the most dominant spatial-temporal coherent structures in the flow field to achieve the modal reduction. For example, proper orthogonal decomposition (POD)

which was proposed by Lumley (1967) [9] is one of the widely used technique for reduced order modelling of the fluid flow since POD modes are mathematically optimal for any given data sets. The main feature of the POD technique is that dominant modes are extracted based on the energy content of the flow. These modes are orthogonal to each other and each POD mode contains continuous frequency spectral. For applications in fluid-structure-interaction (FSI) problems, Janocha et al. (2022) [10] analysed the flow around one degree of freedom (1DoF) VIV cylinder at $Re = 3900$ ($Re = U_\infty D/\nu$, where Re denotes Reynolds number, U_∞ is the free stream flow velocity, D is the cylinder diameter and ν is a kinematic viscosity) and $u_r = 3, 5$ and 7 ($u_r = U_\infty/f_n \cdot D$, where u_r is reduced velocity, f_n denotes the natural frequency of the system in a vacuum) based on multiscale proper orthogonal decomposition (mPOD) proposed by Mendez et al. (2019) [11]. The dominant flow characteristics such as vortex shedding, its super harmonics and the low-frequency modulation of the wake were captured by the mPOD modes. Schubert et al. (2022) [12] implemented spectral proper orthogonal decomposition (SPOD) for analysing the data from particle image velocimetry measurements of a 1DoF VIV cylinder at $Re = 4000$ with $u_r = 8.75$. Eiximeno et al. (2022) [13] investigated the instantaneous flow structures and the wake dynamics of two degree of freedom (2DoF) VIV cylinder by means of POD at $Re = 5300$ with $u_r = 3$ and 5.5. They mentioned that different POD modes have been found in the initial and super-upper branches. Moreover, it was explained that the energy dispersion of the high-order modes is attributed to the cylinder movement in the inline and cross-stream directions. Another popular technique for analysing flow is dynamic mode decomposition (DMD) which was introduced by Schmid (2010) [14]. The extracted DMD modes are characterized by their dynamics and each DMD mode has its own frequency in comparison with other modal decomposition methods. Jovanovic et al. (2014) [15] introduced a sparsity promoting DMD (SPDMD) procedure to select a finite number of dynamically important modes within the time span. Janocha et al. (2021) [16] analysed the coherent structures around vibrating isolated and piggyback cylinders at $Re = 200$ and 3.6×10^6 with $u_r = 5$. They found that for the single VIV cylinder case, the most dynamically important mode is associated with the fundamental shedding frequency. Menon and Mittal (2020) [17] proposed a modified DMD method with a moving frame and applied it for the flow over a sinusoidally pitching airfoil. Yin et al. (2022) [18] investigated hydrodynamic forces acting on the cylinders subjected to VIV with a force partitioning analysis using SPDMD algorithm

combined with a moving frame at $Re = 200$ and 3.6×10^6 with $u_r = 5, 6, 7$ and 12. They concluded that at high Re number flow and $u_r = 6$ the chaotic behaviour of the drag and lift coefficients cannot be represented using only a few dominant modes.

When the dominant modes of the flow are extracted, the most important task is to build a ROM based on these selected modes to predict the temporal evolution of the flow states. To achieve this, Galerkin Projection (GP) approach can be utilized. Barone et al. (2009) [19] summarized that Galerkin approach consists of two steps. The first step is the extraction of the most dominant coherent structures from the flow field by means of POD or DMD. The second step is to project the full-order system dynamics to the selected dominant modes. The result of GP approach gives an approximate description of the real flow dynamics involving in time. The advantage of the discussed method is a saving of computational time and costs as reduced order model is applied. The GP approach has been implemented among different milestone problems (Frère A. et al., 2017 [20], Qi et al., 2023 [21], Carlberg et al., 2011 [22]). Nevertheless, the disadvantages of the GP algorithm exist. For instance, Rempfer (2000) [23] states that the phase space of the POD-Galerkin model may be different from the one of the real flow, even if the POD modes can capture the velocity field with high accuracy. Akhtar et al. (2009) [24] used POD modes of the flow around a fixed cylinder in a Galerkin-projection to obtain the temporal evolution of a nonlinear dynamical system. They mentioned that solution of the original GP approach can drift to some erroneous state even it is initialized with a correct periodic state. Iollo et al. (2000) [25] investigated the reduced order simulation of the Navier-Stokes equations for flow around an airfoil and a square cylinder by implementing the POD-GP. They showed that the accuracy of numerical schemes based on simple Galerkin projection is insufficient and a numerical stabilization is needed. Thus, GP models cannot be equivalent to the solutions of the original Navier-Stokes equations as some features of the flow dynamics may not be captured accurately by using this type of models.

With the development of modern data-driven techniques, a promising alternative method to the GP technique is a neural network based approach to model complex and nonlinear systems, especially turbulent flows (Wang et al., 2022 [26], Maulik & San, 2017 [27], Zhu et al., 2018 [28]). The proposed technique has a crucial benefit to understand and learn correlations between different variables of the dataset with the goal to predict their evolutions. There are neural networks such as multi-layer perceptron (MLP) (Gardner & Dorling, 1998 [29], Orhan et al., 2011 [30]), convolution

neural network (CNN) (Gao et al., 2021 [31], Tong et al., 2019 [32]), recurrent neural network (RNN) (Maulik et al., 2021 [33], Qin et al., 2017 [34]) and long-short-term memory neural network (LSTM-NN) which can be utilized for different purposes. For instance, the CNN can be used to transfer a high-dimensional data into a latent space with low-dimension. The LSTM-NN is able to learn the time series of the data with the strength to overcome the stability issue such as vanishing gradient as outlined by Mohan & Gaitonde (2018) [35]. Therefore, LSTM is a robust method to predict highly chaotic sequential time series as reported by Yeo & Melnyk (2019) [36]. Rahman et al. (2019) [37] developed a LSTM-ROM by using POD to extract dominant modes of a 2D quasigeostrophic turbulence. They showed that LSTM-ROM has significantly higher accuracy in comparison with GP-ROM. Nakamura et al. (2021) [38] constructed ROM based on combination of a three-dimensional convolutional neural network autoencoder (CNN-AE) and LSTM for a turbulence channel flow at $Re_\tau = 100$. They discussed that the large number of latent modes are needed to reproduce the original data with a high accuracy. To tackle this issue, they proposed to use hierarchical autoencoder developed by Fukami (2020) [39] which can achieve a more efficient low-dimensionalization than the conventional AE and POD. Bukka et al. (2021) [40] proposed two hybrid data-driven reduced-order models for prediction of unsteady fluid flow over a single cylinder and the flow past side-by-side cylinders at low Re number: POD-RNN and convolution recurrent autoencoder network (CRAN). They explored two types of RNN which are closed-loop and encoder-decoder RNNs. The LSTM-NN has been utilized for their work to address the issue of long-term dependency in the data. It was reported that CNN-RNN has a good performance for a broader range of nonlinear fluid flow in comparison with POD-RNN. Yousif & Lim (2022) [41] designed POD-LSTM and POD bidirectional LSTM (BLSTM) to predict the temporal evolution of the POD time coefficients of flow around a finite wall-mounted square cylinder at $Re = 12000$. They investigated that the POD-BLSTM model is more accurate for prediction of a complex wake flow behind the finite wall-mounted obstacle in comparison with POD-LSTM. Furthermore, it was mentioned that the error of the POD time coefficients increases as the prediction time window becomes larger.

Despite the fast development of the neural network-based ROMs, their applications in analysis of FSI are still limited. The objective of the present study is designing a novel POD-LSTM-NN ROM for prediction of the temporal behaviours of the flow around a 2DoF VIV cylinder at a high $Re = 3.6 \times 10^6$ with a potential to

replace long-time CFD simulations. To obtain the train data, two-dimensional (2D) Unsteady Reynolds-Averaged-Navier-Stokes (URANS) equations combined with the standard $k - \omega\ SST$ turbulence model, are solved with $u_r = 3, 6,$ and 11. The values of the reduced velocities are chosen in a way to cover the three major VIV branches (Initial Branch (IB), Upper Branch (UB) and Lower Branch (LB)). The mass ratio is set as $m^* = 2$ and the damping ratio as $\zeta = 0$ for all cases to allow maximum amplitude oscillations. The predicted streamwise and cross-flow velocities and displacements of the moving cylinder are used to evaluate the performance of the designed ROM. Furthermore, the designed ROM is used to estimate the lift and drag forces on the cylinder by using a force partitioning method (FPM) proposed by Chang (1992) [42].

The paper is organized as follows. Section 4.2 provides the information about the case geometry and a brief introduction to the numerical method utilized in the present study to generate the training and test data sets. In addition, methodology of creating POD-LSTM-NN model is explained. In Section 4.3, the application of the POD-LSTM-NN ROM for the flow over 2DoF VIV cylinder is discussed. The force partitioning method for estimation of the drag and lift forces is performed also. Finally, conclusions are presented in Section 4.4.

4.2. Methods

4.2.1. Mathematical formulation

The 2D incompressible URANS equations of mass and momentum conservation are given by:

$$\frac{\partial u_i}{\partial x_i} = 0, \tag{4.1}$$

$$\frac{\partial u_i}{\partial t} + u_j \frac{\partial u_i}{\partial x_j} = -\frac{1}{\rho}\frac{\partial P}{\partial x_i} + \nu \frac{\partial^2 u_i}{\partial x_j \partial x_j} - \frac{\partial \overline{(u_i' u_j')}}{\partial x_j}, \tag{4.2}$$

where i, j= 1, 2; x_1, x_2 are the streamwise and cross-flow directions, respectively; u_1 and u_2 are the corresponding mean velocity components; $\overline{u_i'\ u_j'}$ is the Reynolds stress component; u_i' is the fluctuating part of the velocity components; P is the dynamic pressure; ρ is the density of the fluid; ν denotes the kinematic viscosity of the fluid. The Reynolds stress tensor is resolved by applying $k - \omega\ SST$ turbulence model (Menter et al., 2003 [42]) which is a combination of the $k - \omega$ and $k - \varepsilon$ models. The $k - \omega\ SST$ turbulence model incorporates the advantages of the $k - \omega$ model to predict the separation of the shear layers in the near-wall regions under adverse pressure gradient

conditions and $k - \varepsilon$ model to simulate the free-stream flow. The $k - \omega\ SST$ turbulence model has been successfully implemented by Serta et al. (2021) [8], Nieto et al. (2015) [43], Pang et al. (2016) [6] and Janocha & Ong (2021) [44].

The 2DoF VIV cylinder is modelled as a system elastically supported by dampers and springs in the present study. The cylinder is free to oscillate in the in-line (x-axis) and cross-flow (y-axis) paths. The structural stiffness ($k = 89.3, 22.3, 6.6\ kN/m$ for the three investigated u_r respectively) and damping ratio ($\zeta = 0$) are assumed to be the same in both directions. A sketch of the physical system is presented in   Figure 4.1.
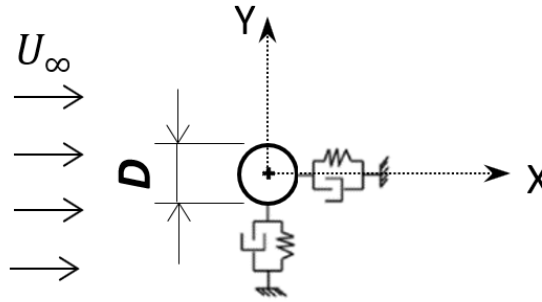

Figure 4.1. Sketch of the modelled physical system.

Gsell et al. (2016) [45] described the physical system of 2DoF VIV cylinder as follow:

$$\ddot{\xi}_i + \frac{4 \cdot \pi \cdot \zeta}{u_r}\dot{\xi}_i + \left(\frac{2 \cdot \pi}{u_r}\right)^2 \xi_i = \frac{C_i}{2 \cdot m^*}, \tag{4.3}$$

where the non-dimensional cylinder displacement, velocity and acceleration in the i-direction (x or y) are denoted as $\xi_i, \dot{\xi}_i$ and $\ddot{\xi}_i$, respectively; the force coefficient in i-direction is defined as $C_i = F_i/0.5\rho DU_\infty{}^2$, where F_i is the force acting on the cylinder in streamwise or cross-stream directions, ρ is the flow density.

4.2.2. Computational overview

The open source CFD toolbox OpenFOAM v2012 is utilized to conduct all simulations in the present study. The PIMPLE algorithm is implemented to solve the governing Eq. (4.1) and (4.2). The PIMPLE algorithm is a combination of the Semi-Implicit Method for Pressure Linked Equations (SIMPLE) and the Pressure Implicit with Split Operators (PISO) method. The second-order Crank-Nicolson time integration scheme is used. The divergence and gradient terms are discretized using the Gauss linear integration scheme. In addition, Gauss linear integration with limited non-orthogonal correction 0.5 is used to discretize the Laplacian term.

The computational domain is shown in Figure 4.2. The centre of the cylinder is located at a distance 10 D from the inlet boundary and 30 D from the outlet boundary. The upper and lower boundaries are placed at the distance 10 D to the centre of the cylinder. The computational domain is shown in Figure 4.1.
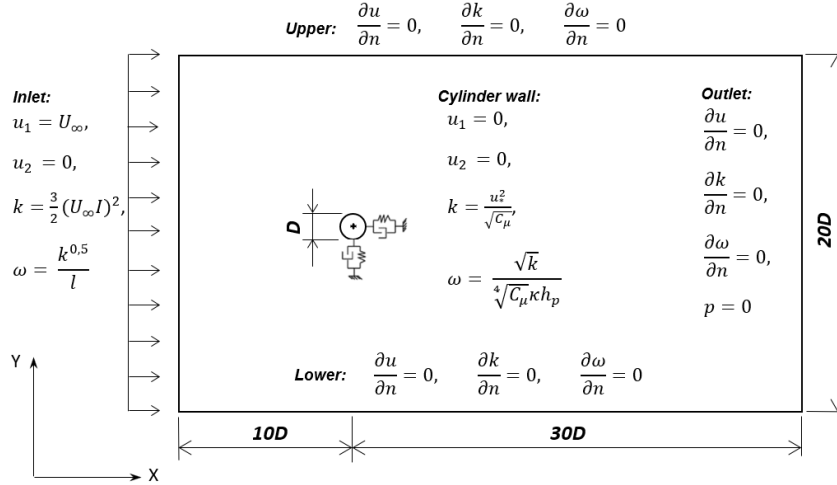

Figure 4.2. The computational domain for the single cylinder configuration.

The boundary conditions for the numerical simulations are given as follow:

1. A uniform flow at the inlet boundary is specified as follow:

$$u_1 = U_\infty \tag{4.4}$$

$$u_2 = 0, \tag{4.5}$$

$$k = \frac{3}{2}(U_\infty I)^2, \tag{4.6}$$

$$\omega = \frac{k^{0,5}}{l} \tag{4.7}$$

where turbulence intensity $I = 1\%$ and the turbulent length scale $l = D$.

2. At the outlet boundary of the domain, streamwise and cross-flow velocities, k and ω are set as zero normal gradient condition, while the pressure is zero.

3. At the upper and lower boundaries, zero normal gradient is imposed for the velocities, the pressure, k and ω.

4. At the cylinder surface, the no-slip condition is applied ($u_1 = u_2 = 0$). A standard wall functions are used to resolve the near-wall boundary layer. Therefore, a criterion of $30 < y^+ < 40$ is used (where $y^+ = h_p \cdot u_*/\nu$). The standard wall functions are specified:

$$k = \frac{u_*^2}{\sqrt{C_\mu}}, \tag{4.8}$$

$$\omega = \frac{\sqrt{k}}{\sqrt[4]{C_\mu} \kappa h_p} \tag{4.9}$$

where u_* is a friction velocity, the modal constant $C_\mu = 0.09$, the Karman constant is $\kappa = 0.41$ and h_p is the distance between the cylinder surface and the centre of the first cell adjacent to the cylinder wall. An example of the mesh used in the present study is shown in Figure 4.3. The mesh near the cylinder surface is refined to accurately capture the separation of the shear layers.
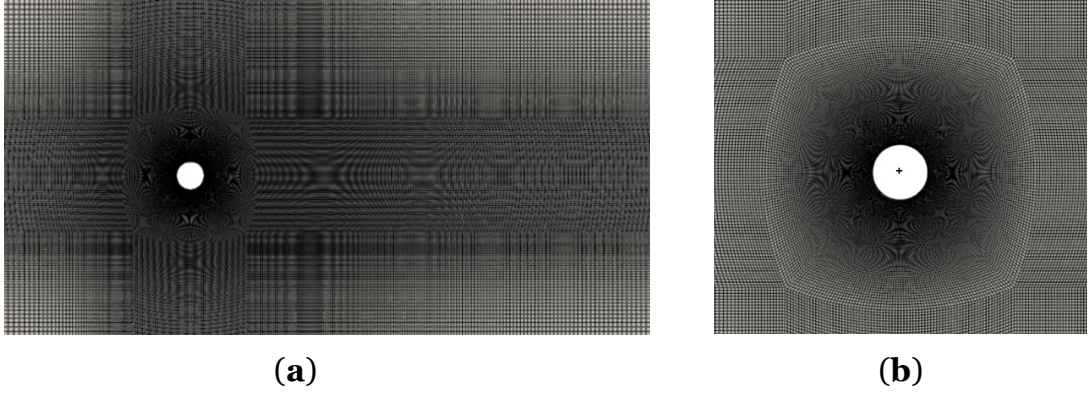

(a)　　　　　　　　　　　　　　　　**(b)**

Figure 4.3. The mesh used in the present study (**a**) an overall view and (**b**) a zoom-in view of the mesh close to the cylinder.

Detailed mesh and time step convergence studies to determine the optimal grid and time step resolutions and the validation of the numerical model for the presented above computational domain and boundary conditions have been performed by Serta et al. (2021) [8]. Therefore, these studies are not repeated in detail here. According to Serta et al. (2021) [8], the mesh with 104536 elements and $Co_{max} = 0.5$ provide sufficient grid and time step convergence. These settings are applied for the numerical simulations in the present study.

4.2.3. POD-LSTM-NN based ROM

In the present study, a POD-LSTM-NN based ROM is designed for 2DoF VIV cylinder. It is a combination of POD and LSTM approaches for the prediction of the temporal evolution of the flow field. The POD technique is widely used in fluid dynamics to extract the most dominant coherent flow structures of the flow field and to create low-dimensional subspace for the flow data. The POD method represents the flow field velocity components in terms of spatial orthogonal modes ϕ_m and their corresponding time coefficients $a_m(t)$. The most energetic modes which capture the

main features of the flow field are extracted and analysed. Therefore, a reduced order approximation of the flow field by using the most energetic modes can be represented as:

$$u(x, y, t) \approx \sum_{n=1}^{N} a_n(t) \cdot \phi_n(x, y), \qquad (4.10)$$

where $u(x, y, z, t)$ denotes the spatial-temporal flow data with the added values of the cylinder velocities and displacements at each time step, and N is the number of the chosen modes.

The temporal evolution of the time coefficients of the dominant modes extracted by the POD approach can be predicted by using the LSTM-NN. LSTM-NN is one of the most successful RNN which can train a model based on temporal sequential histories of time series and predict the future evolutions of the time series. Compared with other RNNs, the LSTM-NN can avoid the problems of vanishing gradient. The basic architecture of the LSTM network is briefly outlined in Figure 4.4a. The input vector that contains the sequential data x is received by the hidden layer which creates an output vector of hidden state h. Based on the new input data and the information from the previous time steps (the previous hidden state and the cell state (C)), the hidden state is maintained and renewed by the hidden layer each iteration. The main feature of the LSTM network is that LSTM cell contains three gates: the input (i), the output (o) and the forget gates (f). The LSTM cell architecture is presented in Figure 4.4b. The input and output gates are responsible for the input and output information of the LSTM cell, respectively. The forget gate allows to minimize the problem of over-fitting by deciding which information from the previous time step should be abandoned. Gers et al. (1999) [46] outlined the equations which are used to compute the outputs of the gates:

$$i_t = \sigma(W_i x_i + U_i h_{t-1} + b_i), \qquad (4.11)$$
$$f_t = \sigma\big(W_f x_i + U_f h_{t-1} + b_f\big), \qquad (4.12)$$
$$\widetilde{C}_t = \tanh(W_C x_t + U_C h_{t-1} + b_c), \qquad (4.13)$$
$$C_t = i_t \otimes \widetilde{C}_t + f_t \otimes C_{t-1}, \qquad (4.14)$$
$$o_t = \sigma(W_o x_t + U_o h_{t-1} + b_o), \qquad (4.15)$$
$$h_t = o_t \otimes \tanh(C_t), \qquad (4.16)$$

where W_i, W_f, W_C and W_o are the weights that map the input to each of the gates; U_i, U_f, U_C and U_o are the weights related to the hidden state at the previous time step; $\widetilde{C}_t$ is the updated cell state. A more detailed information about LSTM architecture can be found in Mohan & Gaitonde (2018) [34] and Yousif & Lim (2022) [40].
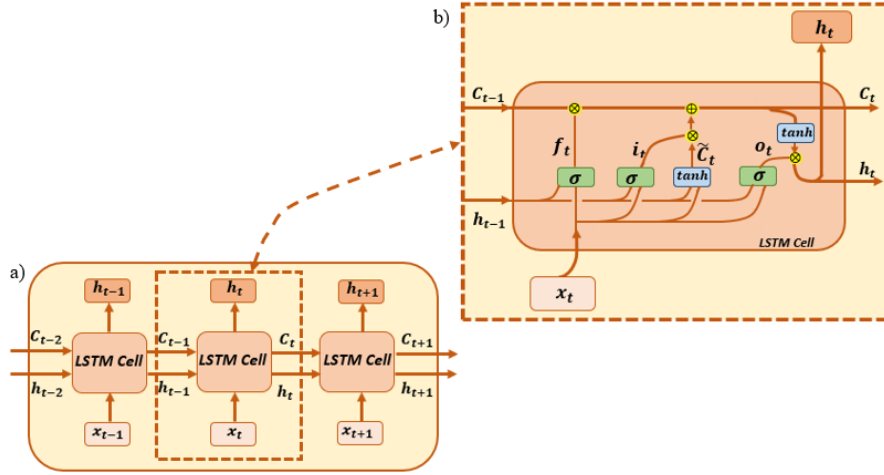

Figure 4.4. Architecture of the (**a**) LSTM NN and (**b**) LSTM cell.

The procedure applied in the present study to build the POD-LSTM-NN ROM is shown in Figure 4.5 and outlined as:

1. The POD analysis is performed on the datasets of the numerical simulations to define the spatial orthogonal modes ϕ_n and their temporal coefficients $a_n(t)$. The number of selected dominant modes N which capture the main flow features should be chosen for future work. Since N is much smaller than the dimension M of $\phi_n \in R^M$ (where M is the number of flow data to represent the flow field), the subspace expanded by ϕ_n ($n = 1,2 \dots N$) can be regarded as the low-dimensional representation of the flow field. The obtained $a_n(t)$ are datasets for training in the LSTM-NN.

2. The time series of the temporal coefficients $a_n(t)$ are divided into several time windows and each time window is further splitted into input (last 0.1s) and output (last 0.1s) parts.

3. The time coefficients of the dominant POD modes should be splitted into the training (70%) and the test (30%) datasets. The test data are used to validate the time coefficients predicted by LSTM.

4. The LSTN-NN needs to be trained. The idea of the training strategy is to teach the neural network the general relationships between the input and output pairs.

5. The validation of the LSTN-NN should be performed afterwards as follow: the predicted time coefficients of the future time steps are compared with the test datasets gained by the POD analysis at the same time steps using the numerical simulations results.

6. The flow field can be further reconstructed by using the dominant POD modes and the predicted time coefficients obtained by LSTM-NN by applying Eq. (4.10).

In the present study, the LSTM-NN is designed based on the open-source toolbox TensorFlow and Keras. The LSTM-NN parameters are presented in Table 4.1. An ADAM optimizer is applied to obtain the parameters in each LSTM cell. The total number of snapshots used for the cases with $u_r = 3, 6$ and 11 are 1145 (lasting 22.9s), 1752 (lasting 35.04s) and 1200 (lasting 24s), respectively.

Table 4.1. Parameters of LSTM-NN.

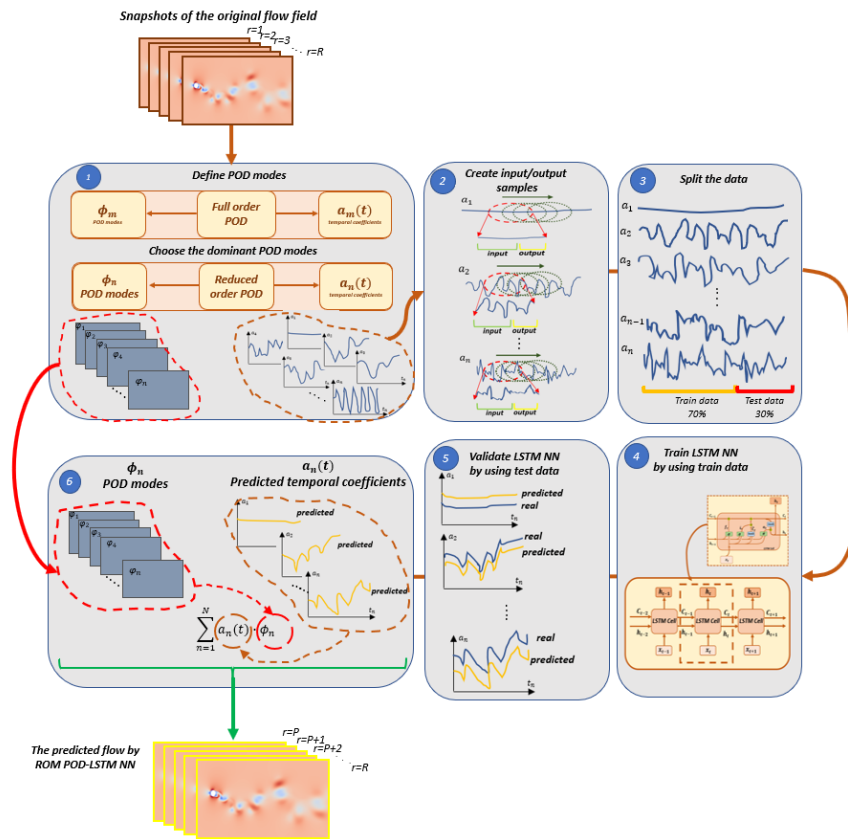| Batch size	Number of hidden layers	Number of cells	Epoch	Learning rate	Input size	Output size
32	1	250	40	0.0001	5	5

Figure 4.5. The procedure of building the POD-LSTM-NN ROM.

4.3. Results

The objective of the present section is to build POD-LSTM-NN ROMs for the flow over 2DoF VIV cylinder at $Re = 3.6 \times 10^6$ with $u_r = 3, 6,$ and 11 ($u_r = U_\infty / f_n \cdot D$, where u_r is reduced velocity, U_∞ is the free stream flow velocity, D is the cylinder diameter, f_n denotes the natural frequency of the system in a vacuum) to predict the instantaneous flow structures as well as the cross-flow and streamwise velocities and displacements of the cylinder. Furthermore, FPM is applied to define the lift and drag forces acting on the cylinder by using the flow field predicted by the POD-LSTM-NN ROMs.

It is worth mentioning that the application of the POD-LSTM-NN ROM for the flow field around a 2DoF cylinder has more challenges than for the flow over a fixed cylinder case. Firstly, when applying the POD technique, there is difficulty in dealing with the moving boundary of the flexible supported cylinder as reported by Yin et al. (2022) [18]. Secondly, the flow field around a 2DoF cylinder is more complicated in comparison with the flow structures around a fixed bluff body. Initial, upper and lower branches which are characterized by the various flow topologies are considered for the moving cylinder. Therefore, a large number of POD modes should be used to achieve a high-quality model for the prediction of the flow field over a VIV cylinder. This has been shown through a comparison of the mode behaviour and the evaluation of the reconstruction flow field by using the modes for a VIV and stationary cylinder in Janocha et al. (2021) [16].

4.3.1. Proper Orthogonal Decomposition Analysis

The goal of the POD method is to create a low-dimensional representation of the data while still keeping the dominant information such as the coherency and a large portion of the total energy of the full model. The singular value decomposition (SVD) is used to decompose the flow field data into the spatial modes which represent the coherent structures and their temporal coefficients. In the present study, the POD analysis is applied for datasets consisting of the flow velocities and the structural velocities of the cylinder obtained by using the CFD simulations for flow over a 2DoF VIV cylinder with $u_r = 3, 6$ and 11 at $Re = 3.6 \times 10^6$. To achieve a high-quality representation of the chaotic and irregular surrounding flow, the number of modes which contains 90% of the total energy are chosen to build the ROMs.

Figure 4.6 shows the contribution of the energy of each mode to the total energy and the cumulative energy of the POD modes for $u_r = 3, 6$ and 11. According to Figure 4.6a, the first mode which corresponds to the time-averaged flow contributes the most to the total kinetic energy. The distribution of the eigenvalues for $u_r = 11$ has more rapid decay in comparison with $u_r = 3$ and 6. It indicates that the lower number of modes are needed to capture the main flow features for $u_r = 11$ than for the other two cases. A possible reason is that the flow field for $u_r = 11$ is characterized by more organized large-scale flow structures compared with the vorticity features of the flow fields for $u_r = 3$ and 6. Therefore, fewer POD modes are required to capture the same level of energy for $u_r = 11$ than for two other cases. This has also been reported in Yin et al. (2022) [18]. Table 4.2 provides the number of modes which are used to build the ROMs with up to 90% of the flow energy for $u_r = 3, 6$ and 11.
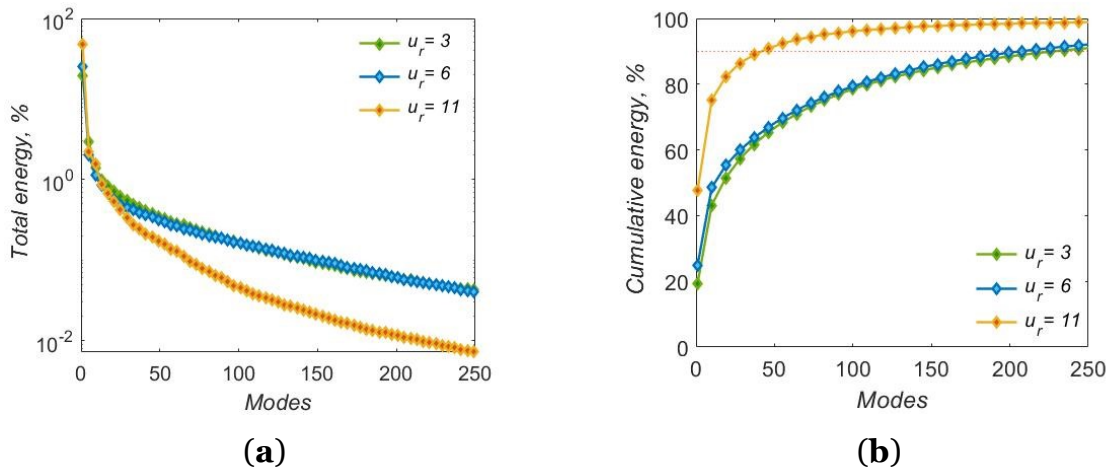

Figure 4.6. POD of the flow field past 2DoF VIV cylinder: (**a**) energy contribution by each mode and (**b**) cumulative energy.

Table 4.2. The number of modes used to build ROMs to capture 90% of total flow energy.

	$u_r = 3$	$u_r = 6$	$u_r = 11$
Number of modes	229	208	42

Figure 4.7 shows the spatial structures and the length scale features of the crossflow velocity extracted by the POD approach for $u_r = 3$ which refers to the initial branch of VIV lock in. The cumulative energy of each mode is also shown in Figure 4.7. The initial branch is characterized by the formation of two single counter-rotating vortices (2S) per shedding cycle, similar to the von-Karman vortex street observed

behind a stationary cylinder. Modes 1 and 2 contribute to the formation of the main flow behaviour where separated shear layers are aligned with the wake centreline. The contribution of the small-scale flow structures which represent the nonlinear nature of the flow can be captured by increasing the number of pair modes. According to Figures 4.7f and 4.7g, a large number of the small vorticity structures are located close to the bluff body near its front and back surfaces. Such compact arrangement of the coherent structures causes a suppression of the high cylinder vibration amplitudes.
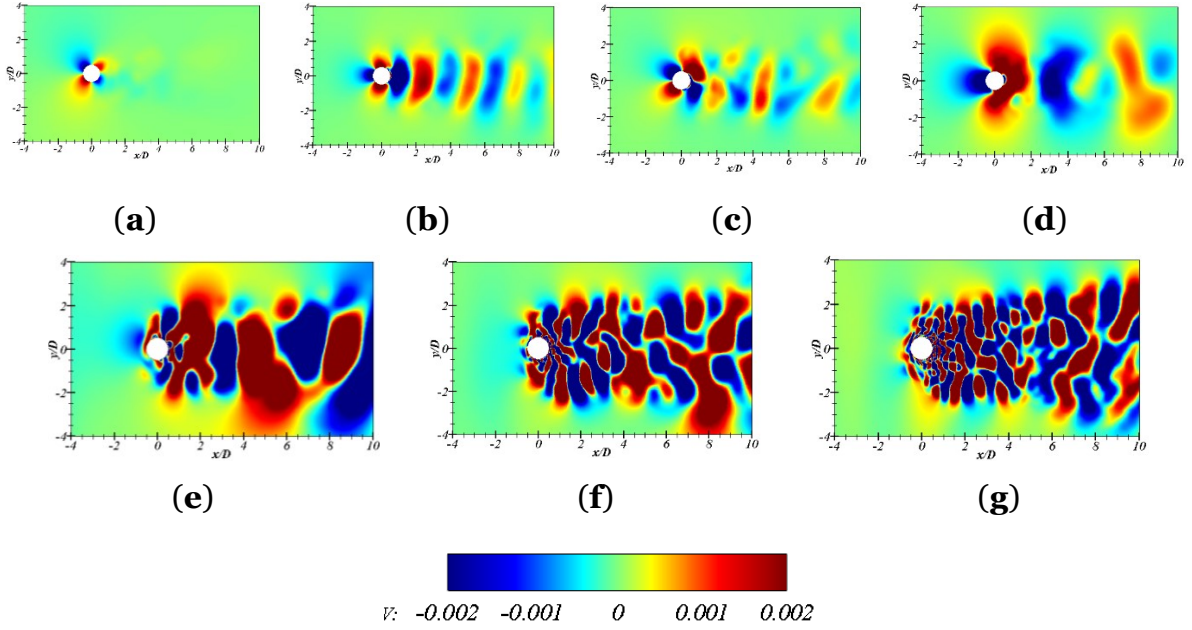

Figure 4.7. Spatial structures of the cross-flow velocity for $u_r = 3$: (**a**) Mode 1 (19%), (**b**) Mode 2 (24%), (**c**) Mode 3 (28 %), (**d**) Mode 4 (31%), (**e**) Mode 38 (60%), (**f**) Mode 118 (80%), (**g**) Mode 228 (90%).

Figure 4.8 shows the cross-flow velocities of the POD modes for $u_r = 6$ which belongs to the upper branch of the VIV lock-in. The main distinctive property of the upper branch flow pattern is the separation of two triplets (2T) of vortices per shedding cycle which causes a highly chaotic flow around the cylinder. The obvious difference between the initial and upper branches which can be depicted from the contour plots shown in Figure 4.8 is that spatial structures are in a broader distribution away from the wake centreline due to a larger vibration amplitude of the cylinder. Nevertheless, the number of modes to capture 90% of the flow energy for $u_r = 6$ (208 modes) is a slightly lower than for $u_r = 3$ (228 modes). The possible reason is that coherent flow structures of the upper branch are comparatively more spatially organized compared with the initial branch.
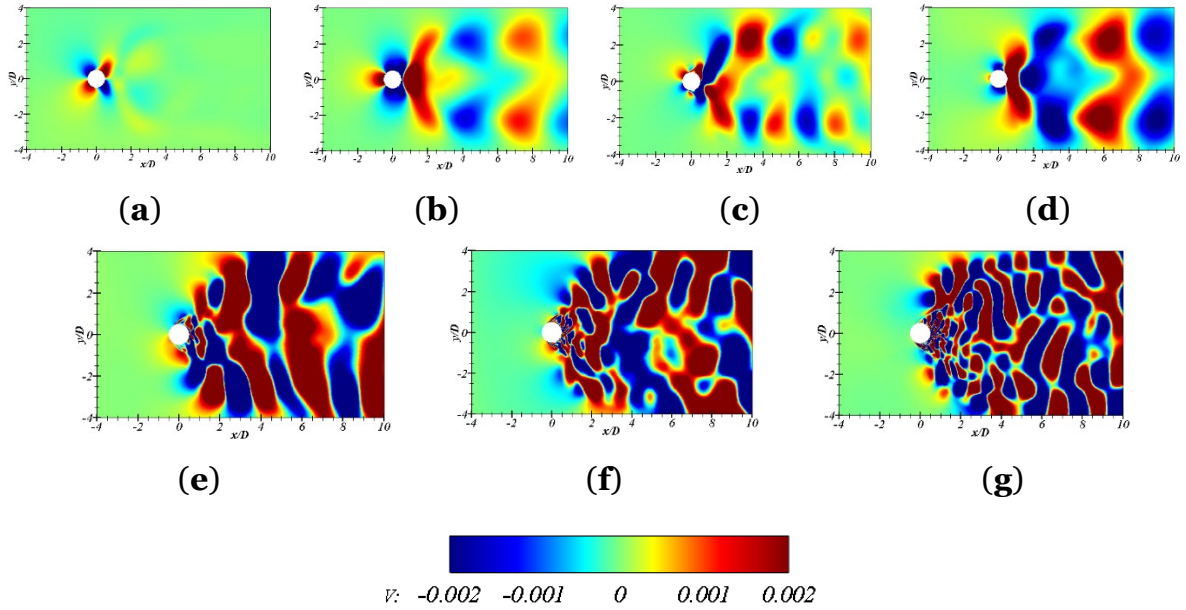
Figure 4.8. Spatial structures of the cross-flow velocity for $u_r = 6$: (**a**) Mode 1 (25%), (**b**) Mode 2 (32%), (**c**) Mode 3 (35%), (**d**) Mode 4 (38%), (**e**) Mode 30 (60%), (**f**) Mode 108 (80%), (**g**) Mode 208 (90%).

The spatial structures of the cross-flow velocity component for $u_r = 11$ which is referred to the lower branch of the VIV lock-in are shown in Figure 4.9. The lower branch is indicated by the separation of the two pairs (2P) of the counter-rotating vorticities per shedding cycle. According to Figure 4.9, the spatial structures of the lower branch are placed narrower around the cylinder centreline in comparison with the upper branch. Furthermore, the highly energetic coherent structures of the lower branch occupy larger space in a far wake region in comparison with a near wake area. The near-wake region is characterized by the tightly distributed spatial structures largely placed near the back cylinder surface as shown in Figure 4.9f.
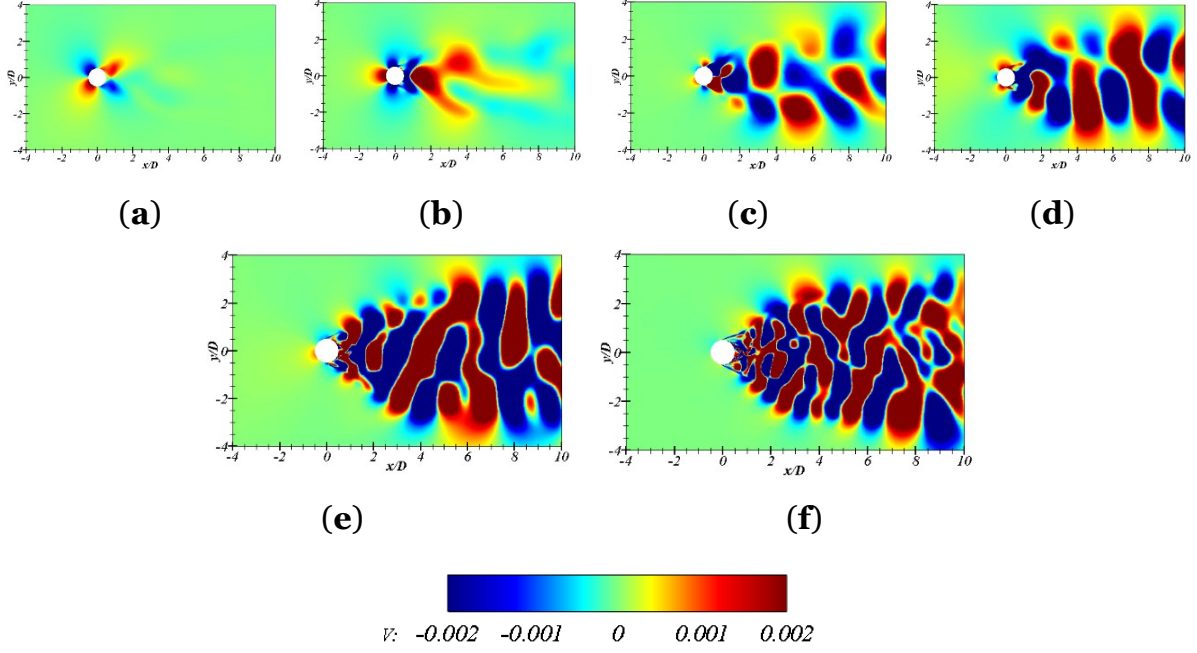
Figure 4.9. Spatial structures of the cross-flow velocity for $u_r = 11$: (**a**) Mode 1 (48%), (**b**) Mode 2 (57%), (**c**) Mode 3 (60%), (**d**) Mode 4 (63%), (**e**) Mode 20 (80%), (**f**) Mode 42 (90%).

4.3.2. Implementation of the POD-LSTM-NN ROM

The temporal coefficients of the POD modes defined in the previous section are used to train the LSTM-NN. In the present study, a direct approach to train the LSTM-NN is used, i.e., each POD mode has its own LSTM-NN model. Therefore, if n dominant POD modes are chosen to build the ROM, n LSTM-NN models are needed to be created. The same parameters to train the LSTM-NN models for all selected POD modes are used to save computational time. When the designed LSTM-NN model is tested, the input parameters for the model should be chosen from the temporal coefficients of the relevant mode from the test dataset. The LSTM-NN model predicts the values of the temporal coefficients which follow directly after chosen input samples.

The comparison of performances of the LSTM-NN models for the train and test datasets for the cases with $u_r = 3, 6$ and 11 are presented in Table 4.2. The mean absolute scaled error (MASE) allows to evaluate how good the model is compared with the real data. The mean MASE is calculated as follow:

$$MASE = \frac{1}{n} \sum_{i=1}^{n} \left| \frac{A(i) - B(i)}{\sum_{j=2}^{n} \frac{A(j) - A(j-1)}{n-1}} \right|, \tag{4.17}$$

where n is the total number of the time instants; $A(i)$ denotes the real value at the time instant i; $B(i)$ is the forecasted value at the time instant i. If the value of MASE is close or lower than one, the model can be considered as a high-quality model. Otherwise, if MASE is larger than one, it means that the model gives poor representation of the real data. According to Table 4.2, the first order mode of each case gives the greatest mean and STD MASE for both train and test datasets. Since the first mode is the most energetic it leads to higher negatively impact the flow field accuracy. For example, the mean MASE of the first mode of the train/test datasets is 8.3/11.9, 23.6/17.4 and 42.0/27.4 for $u_r = 3, 6$ and 11, respectively.

Table 4.2. Performance of LSTM-NN model for $u_r = 3, 6$ and 11 for train and test datasets.

	Mean MASE Train/Test	STD MASE Train/Test	Accuracy Train/Test	Final loss Train/Test
		$u_r = 3$		
Mode 1 (19%)	8.3/11.9	7.7/15.2	0.3132/0.3109	0.0013/0.0011
Mode 2 (24%)	1.7/1.7	2.7/2.4	0.8264/0.8534	0.0029/0.0024
Mode 3 (28%)	1.2/1.3	1.8/1.7	0.8465/0.8152	0.0027/0.0028
Mode 4 (31%)	1.6/2.1	1.6/2.9	0.7918/0.7507	0.0023/0.0016
Mode 38 (60%)	2.9/2.3	2.9/1.9	0.4893/0.4487	0.0112/0.0084
Mode 118 (80%)	2.2/1.8	4.7/1.3	0.4403/0.4076	0.0207/0.0207
Mode 228 (90%)	1.5/1.5	1.2/1.0	0.3723/0.3988	0.0217/0.0196
		$u_r = 6$		
Mode 1 (25%)	23.6/17.4	60.5/28.7	0.1803/0.3021	0.0004/0.0004
Mode 2 (32%)	3.5/1.2	8.5/1.1	0.7738/0.8279	0.0016/0.0014
Mode 3 (35%)	1.7/1.2	2.1/1.3	0.7975/0.8432	0.0023/0.0024
Mode 4 (38%)	1.7/1.5	2.4/2.2	0.7598/0.7533	0.0021/0.0017
Mode 30 (60%)	2.3/2.1	2.3/2.2	0.6230/0.6577	0.0058/0.0056
Mode 108 (80%)	2.5/2.4	2.1/1.7	0.4189/0.4073	0.0123/0.0124
Mode 208 (90%)	1.7/1.8	1.7/1.5	0.4074/0.4340	0.0169/0.0158
		$u_r = 11$		
Mode 1 (48%)	42.0/27.4	60.5/29.3	0.2209/0.2067	0.0004/0.0004
Mode 2 (57%)	6.5/2.9	15.6/4.8	0.6711/0.8324	0.0011/0.0011
Mode 3 (60%)	2.8/2.5	3.9/4.7	0.8163/0.8212	0.0018/0.0017
Mode 4 (63%)	1.3/0.88	1.5/1.0	0.8307/0.7151	0.0016/0.0013
Mode 20 (80%)	1.1/0.8	1.2/1.7	0.8427/0.8128	0.0037/0.0033
Mode 42 (90%)	1.8/1.7	2.9/2.4	0.6639/0.6201	0.0086/0.0069

There is a tendency of decreasing the mean and STD MASE and increase of the model accuracy up to 85% with increasing the rank of the POD mode. For instance, the mean MASE of the fourth mode of the train/test datasets are 1.6/2.1, 1.7/1.5 and 1.3/0.88 for $u_r = 3, 6$ and 11, respectively. However, when the POD mode order is high, the LSTM-NN with the set parameters cannot represent the temporal coefficient

fluctuation properly. For example, Modes 118, 108 and 42 of $u_r = 3, 6$ and 11, respectively, have enragement of the mean MASE up to 2.2/1.8, 2.5/2.4 and 1.8/1.7 for train/test datasets. The gap between the training and test datasets is a clear indication of over-fitting (training accuracy is large than the test accuracy) or under-fitting (training accuracy is smaller than the test accuracy) behaviour of the LSTM-NN model. According to Table 4.2, there are slight deviations between the train and test accuracies at the different POD modes. The possible solution to overcome over- and under-fitting is to set different LSTM-NN parameters for low and high order POD modes. The training loss indicates how well the model is fitting the training data while the test loss indicates how well the model fits new data. According to Table 4.2, there is a trend of increasing final loss values with rising order POD mode for both train and test datasets. Nevertheless, the final loss is less than 0.1 for all presented cases, which proves that the LSTM-NN model performance can be accepted.

Figures 4.10-4.12 show the comparison of the temporary coefficients obtained by the CFD simulations and predicted by the LSTM-NN models for $u_r = 3, 6$ and 11. LSTM-NN can still show a good performance for prediction of the low order POD modes up to Mode 38 as shown in Figures 4.10e, 4.11e and 4.12e. However, the trained LSTM-NN underestimates the real data and cannot accurately capture the original fluctuation of the high rank POD mode temporal coefficients for $u_r = 3$ and 6 as shown in Figures 4.10f-g and 4.11f-g.
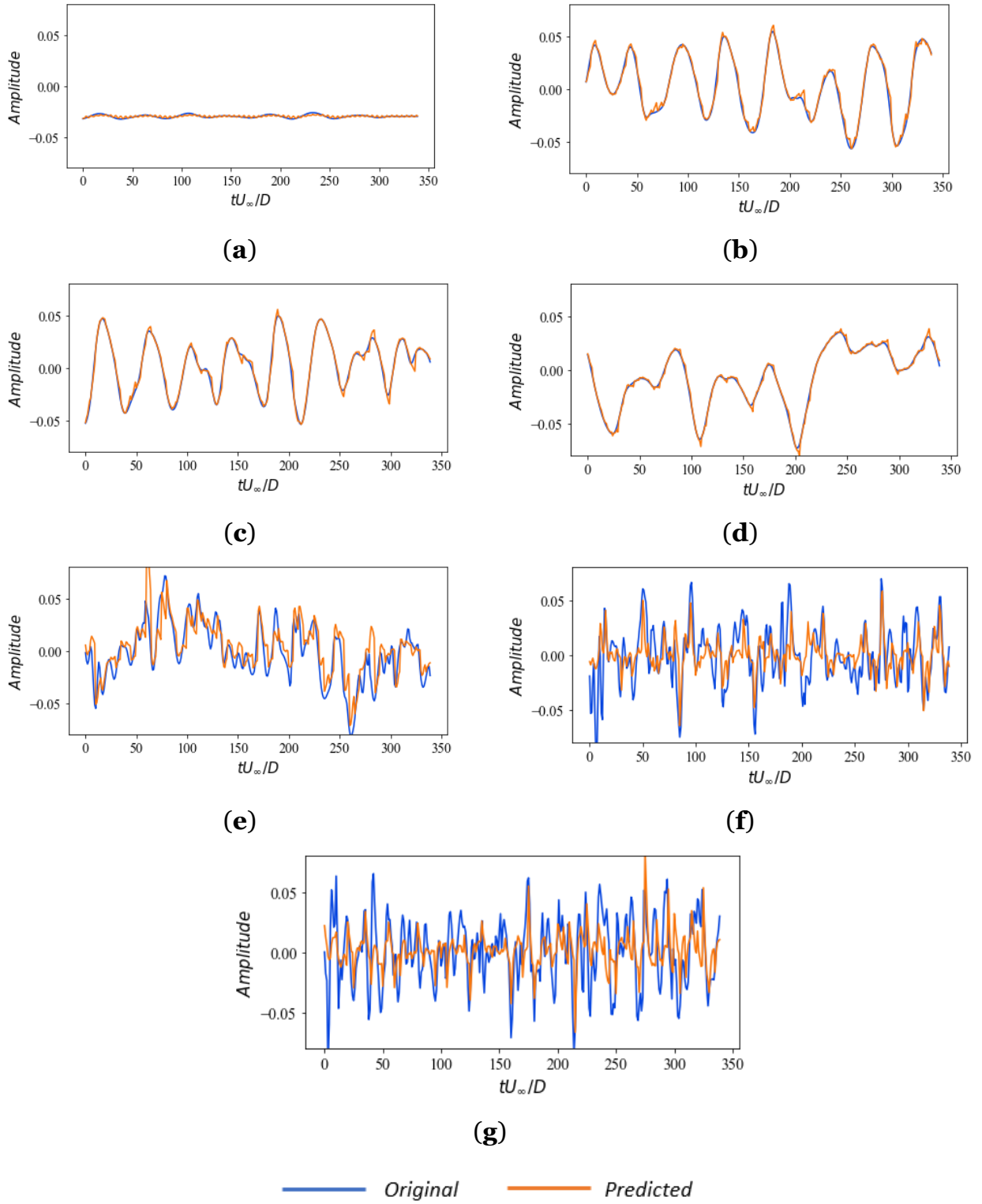
Figure 4.10. The real and predicted temporary coefficients for $u_r = 3$: (**a**) Mode 1 (19%); (**b**) Mode 2 (24%); (**c**) Mode 3 (28%); (**d**) Mode 4 (31%); (**e**) Mode 38 (60%); (**f**) Mode 118 (80%); (**g**) Mode 228 (90%).
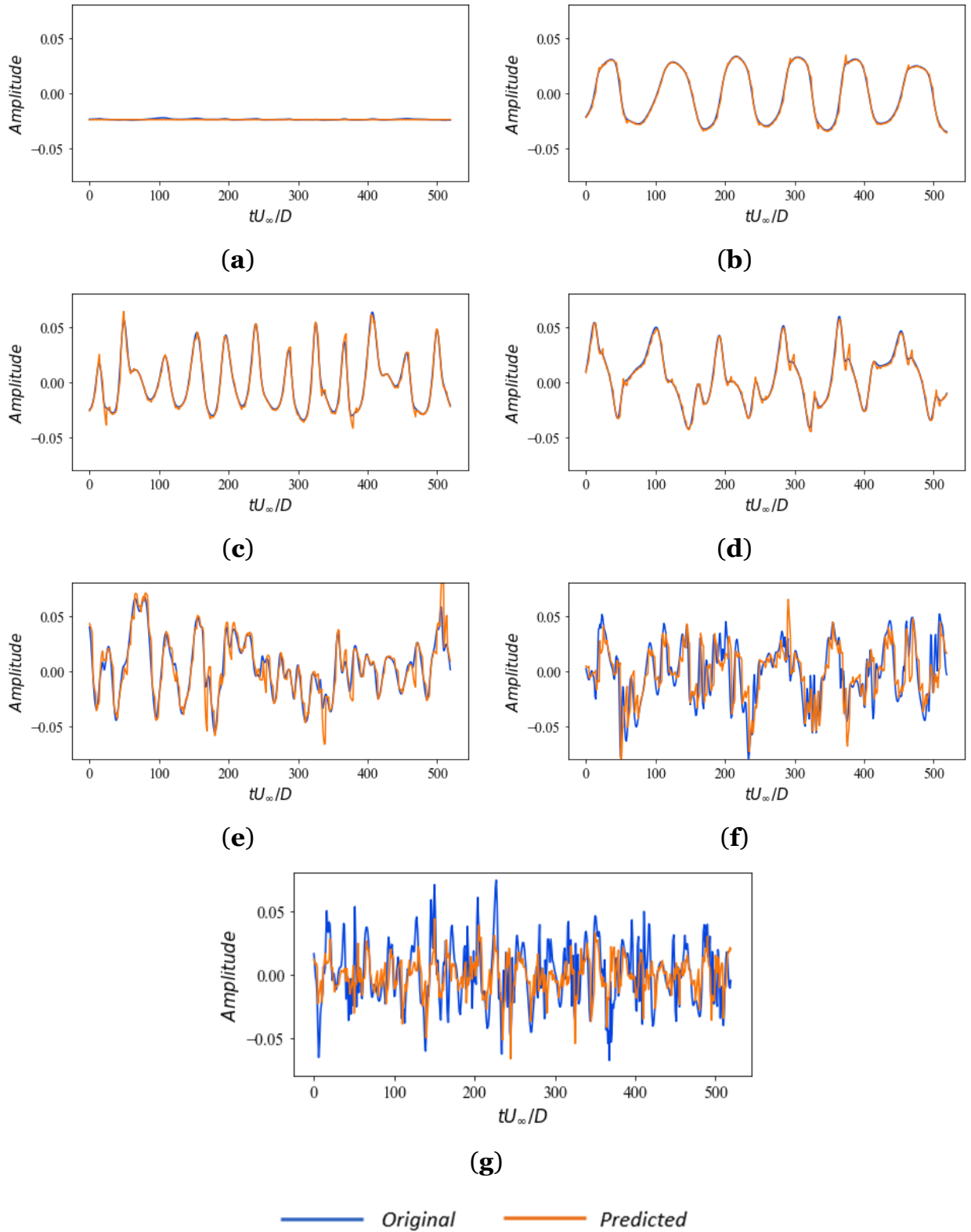
Figure 4.11. The real and predicted temporary coefficients for $u_r = 6$: (**a**) Mode 1 (25%); (**b**) Mode 2 (32%); (**c**) Mode 3 (35%); (**d**) Mode 4 (31%); (**e**) Mode 30 (60%); (**f**) Mode 108 (80%); (**g**) Mode 208 (90%).
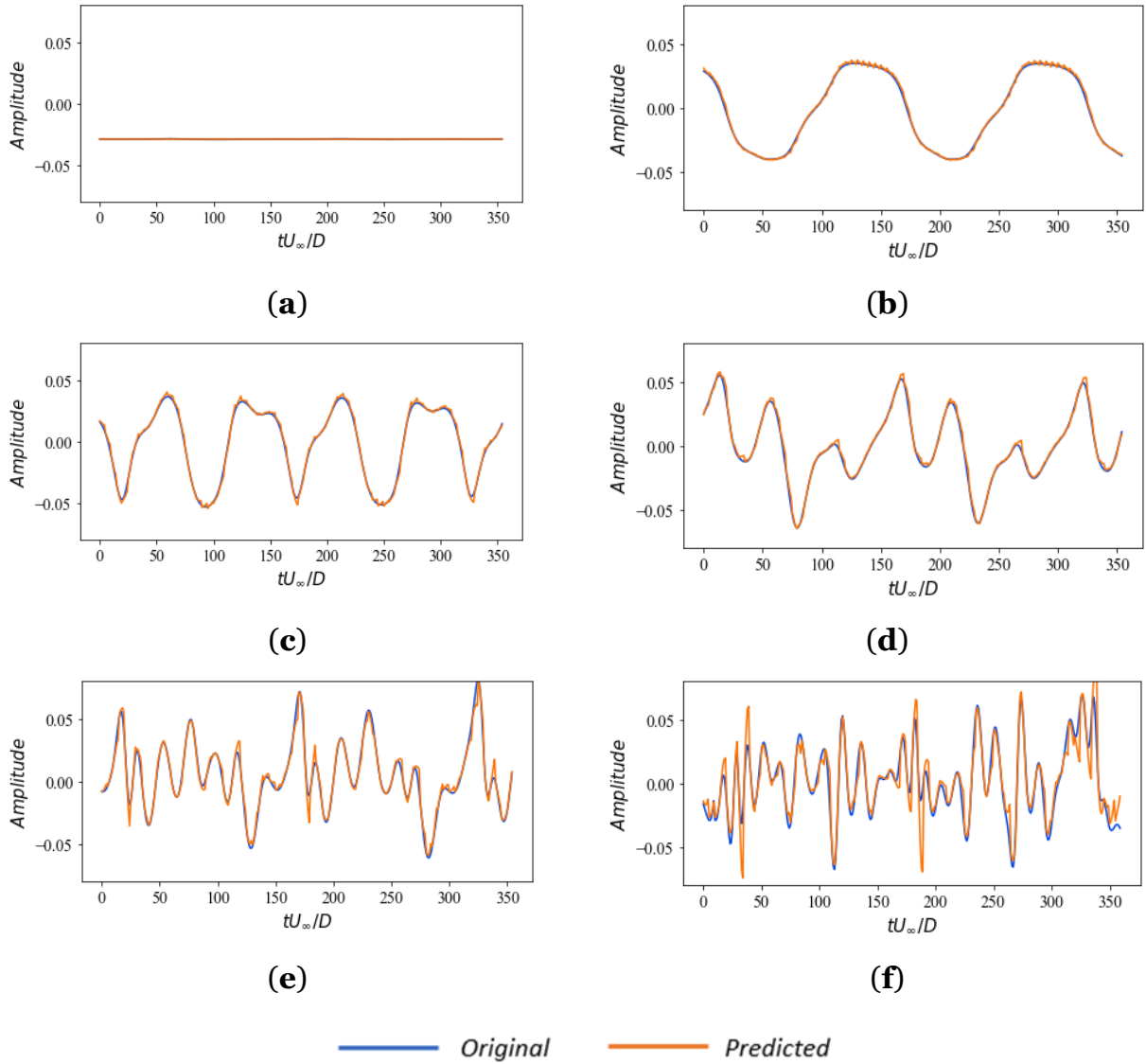
Figure 4.12. The real and predicted temporary coefficients for $u_r = 11$: (**a**) Mode 1 (48%); (**b**) Mode 2 (57%); (**c**) Mode 3 (60%); (**d**) Mode 4 (63%); (**e**) Mode 20 (80%); (**f**) Mode 42 (90%).

When the LSTM-NN models are trained and the temporal coefficients for each chosen POD mode are calculated, then the flow field can be reconstructed by using Eq. (4.10). The cross-flow velocity obtained by using CFD simulations and predicted by the POD-LSTM-NN ROMs are shown in Figure 4.13 for $u_r = 3, 6$ and 11 . The instantaneous predicted flow fields using the POD-LSTM-NN ROMs which capture 60%, 80% and 90% of the total energy are compared. An increasing accuracy of the predicted flow is achieved by using more POD modes to build the POD-LSTM-NN ROMs. The including of high order POD modes allows to capture the contribution of the small-scale flow structures, which can be clearly seen from Figures 4.13f, 4.13i and

4.13l. However, there is need to find a balance between the quality of the ROM LSTM-NN and its complexity, i.e., the number of modes used to build ROM, to save computational resources.
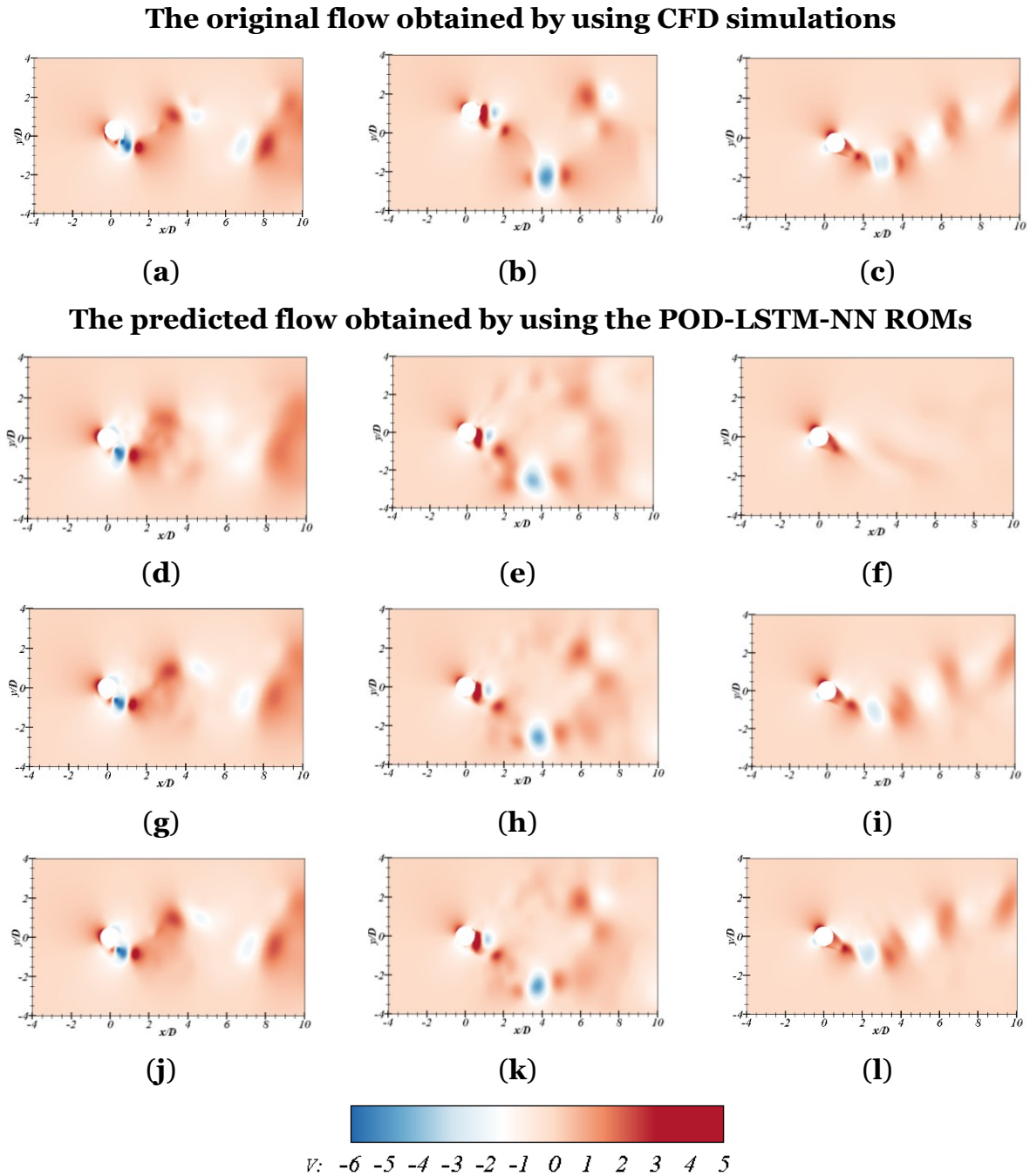
The original flow obtained by using CFD simulations

(a)   (b)   (c)

The predicted flow obtained by using the POD-LSTM-NN ROMs

(d)   (e)   (f)

(g)   (h)   (i)

(j)   (k)   (l)

V: -6   -5   -4   -3   -2   -1   0   1   2   3   4   5

Figure 4.13. A comparison of the cross-flow velocity of the original CFD simulations and the predicted flow field using POD-LSTM-NN ROM at $u_r = 3$: (**a**) the CFD simulations, (**d**) sum of 39 modes – 60% of the total energy, (**g**) sum of 118 modes – 80% of the total energy, (**j**) sum of 229 modes – 90% of the total energy; $u_r = 6$: (**b**) the CFD simulations, (**e**) sum of 30 modes – 60% of the total energy, (**h**)

sum of 108 modes – 80% of the total energy, (**k**) sum of 208 modes – 90% of the total energy; $u_r = 11$: (**c**) the CFD simulations, (**f**) sum of 3 modes – 60% of the total energy, (**i**) sum of 20 modes – 80% of the total energy, (**l**) sum of 42 modes – 90% of the total energy.

Figure 4.14 shows the comparison of the instantaneous contours of the spanwise vorticity of the original CFD simulations and the flow fields predicted by the POD-LSTM-NN ROMs with 90% of the flow energy. It can be seen that the dominant large-scale features of the coherent flow structures are successfully reconstructed by the POD-LSTM-NN ROMs for $u_r = 3, 6$ and 11. Nevertheless, there is a small-scale noise in the wake region for the predicted flows which can be eliminated by adding more high order POD modes as shown in Yin et al. (2022) [18]. To further explain this, the reconstructed flow fields using different number of POD modes for $u_r = 11$ are selected as an example. Figure 4.15 shows the comparison of the instantaneous contours of the spanwise vorticity reconstructed by the POD-LSTM-NN ROMs using 42, 90 and 170 POD modes at $u_r = 11$. According to Figure 4.15, with an increasing number of high order POD modes, the small-scale noisy structures in the wake region can be progressively eliminated since high order modes allow to capture the small-scale structures. Adding more high order modes will increase the reconstruction accuracy of the spatial-temporal coherent structures.
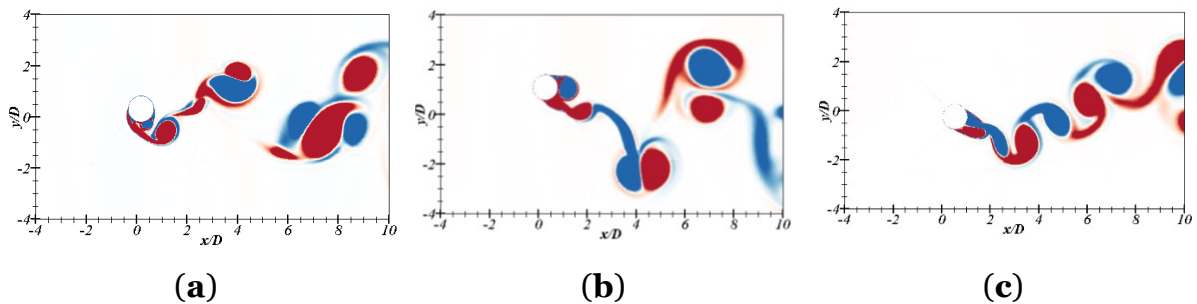
The original flow obtained by using CFD simulations

(**a**) (**b**) (**c**)

Figure 4.14. *Cont.*

The predicted flow obtained by using the POD-LSTM-NN ROMs
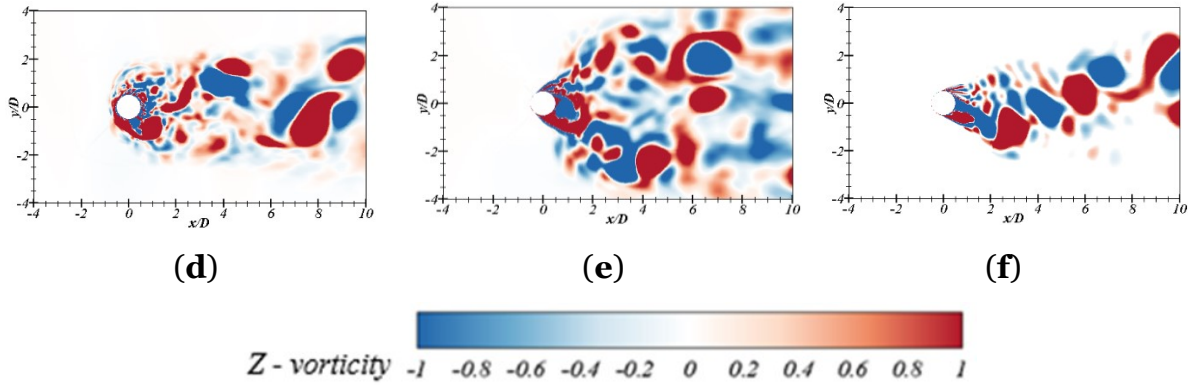

(d)   (e)   (f)

Figure 4.14. A comparison ot the instantenous contours of the spanwise vorticity of the original CFD simulations and the predicted flow field using POD-LSTM-NN ROM at $u_r = 3$: (**a**) the CFD simulations, (**d**) sum of 229 modes – 90% of the total energy; $u_r = 6$: (**b**) the CFD simulations, (**e**) sum of 208 modes – 90% of the total energy; $u_r = 11$: (**c**) the CFD simulations, (**f**) sum of 42 modes – 90% of the total energy.
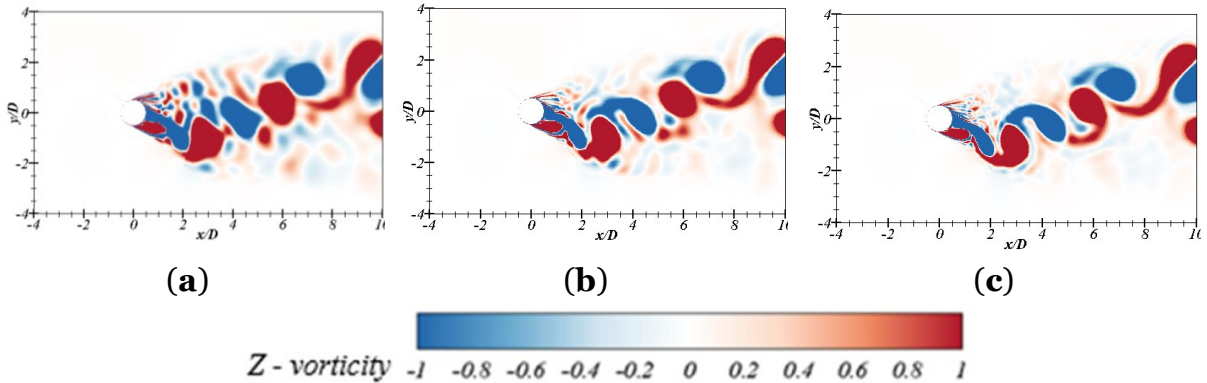

(a)   (b)   (c)

Figure 4.15. A comparison ot the instantaneous contours of the spanwise vorticity of the flow fields predicted by using POD-LSTM-NN ROMs with different numbers of POD modes for $u_r = 11$: (**a**) sum of 42 modes – 90% of the total energy, (**b**) sum of 90 modes – 95% of the total energy, (**c**) sum of 170 modes – 98% of the total energy.

    Figure 4.16 shows the time histories of the streamwise and cross-flow velocities of the 2DoF cylinder obtained by the CFD simulations and predicted by the POD-LSTM-NN ROMs which represents 90% of the total flow energy. The coefficients of the

determination (R^2) are used to define how good the predicted time histories approximate the actual data. R^2 can be calculated as follow:

$$R^2 = 1 - \frac{\sum_{i=1}^{n}\bigl(A(i) - B(i)\bigr)^2}{\sum_{i=1}^{n}(A(i) - \sum_{i=1}^{n} A(i)/n)^2}, \tag{4.18}$$

where n is the total number of the time instants; $A(i)$ denotes the real value in the time instant i; $B(i)$ is the forecasted value in the time instant i. The parameter takes the values between 0 (poor approximation) and 1 (good approximation). According to Figure 4.16, the values of the determination coefficients are close to 1 for $u_r = 3, 6$ and 11. It confirms a high capability of the POD-LSTM-NN ROMs to predict cylinder motions subjected to the highly chaotic turbulent flow.
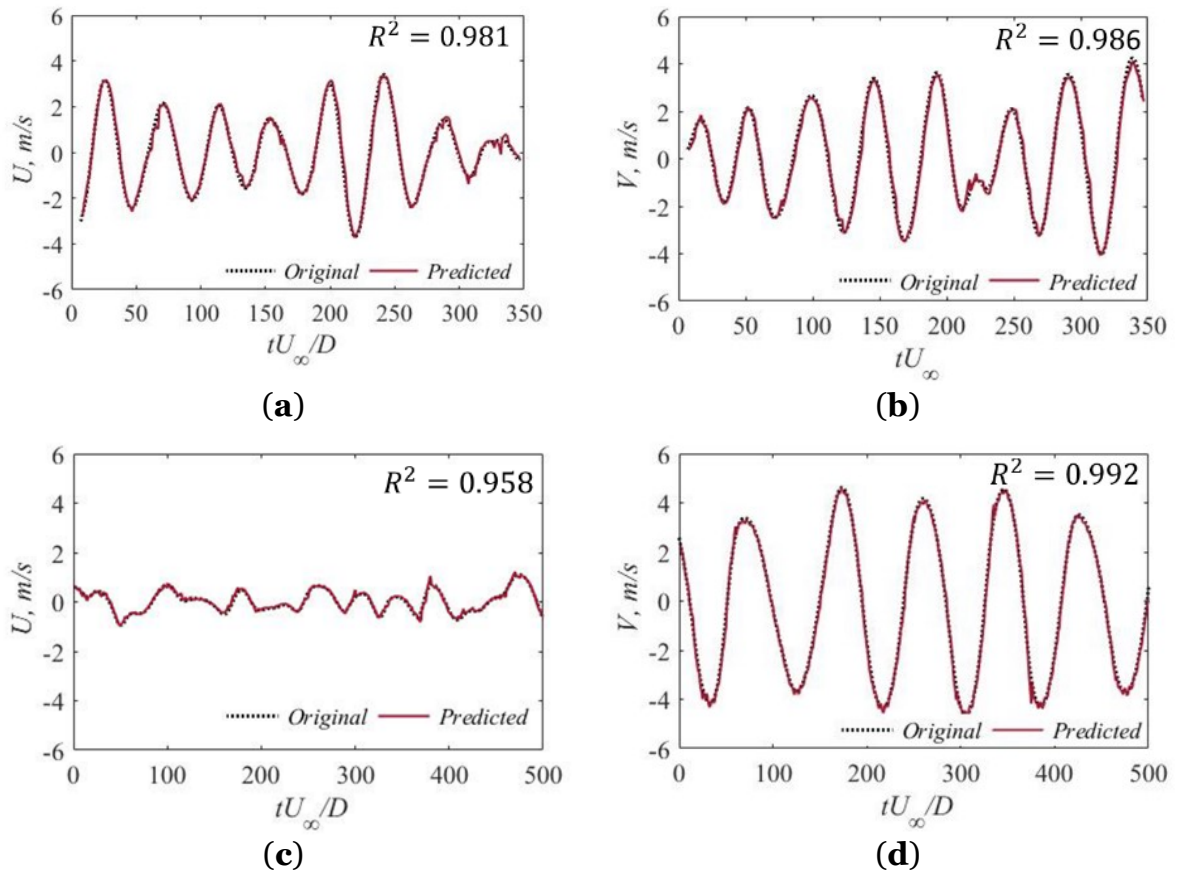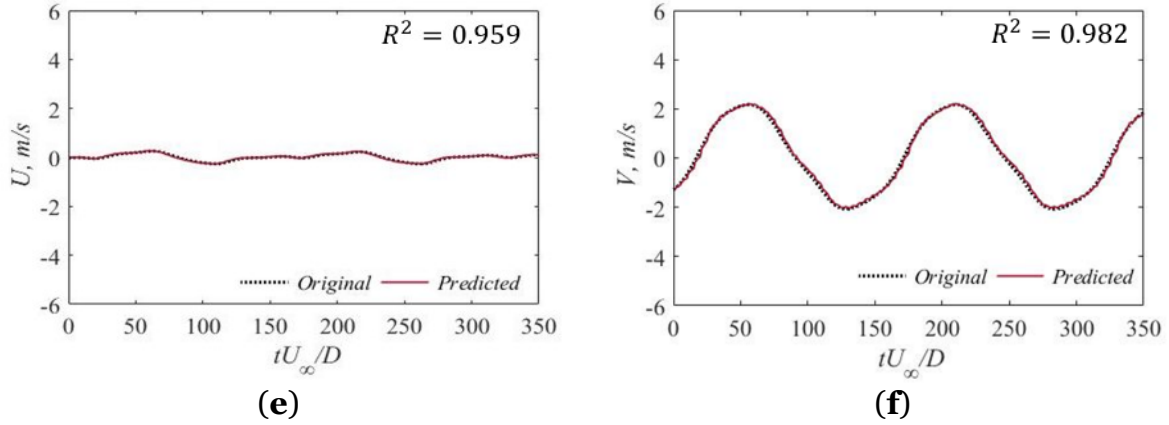

Figure 4.16. *Cont.*

80

(e)   **(f)**

Figure 4.16. The time histories of (**a, c, e**) the streamwise and (**b, d, f**) the cross-flow velocities of the cylinder obtained by the CFD simulations and predicted by the POD-LSTM-NN ROMs for (**a, b**) $u_r = 3$, (**c, d**) $u_r = 6$ and (**e, f**) $u_r = 11$.

Furthermore, the comparison of the streamwise, cross-flow displacements and the trajectories of the cylinder obtained by the CFD simulations and the POD-LSTM-NN ROMs are also shown in Figure 4.16. In general, the POD-LSTM-NN ROMs predict the cross-flow displacement of the cylinder better than the streamwise displacement for all considered cases. According to Figure 4.17, the prediction of the cylinder displacement in both directions is the most accurate for the case with $u_r = 11$ which is confirmed by the relatively high values of the determination coefficients. The cylinder trajectory for $u_r = 11$ is also more organized in comparison with $u_r = 3$ and 6.
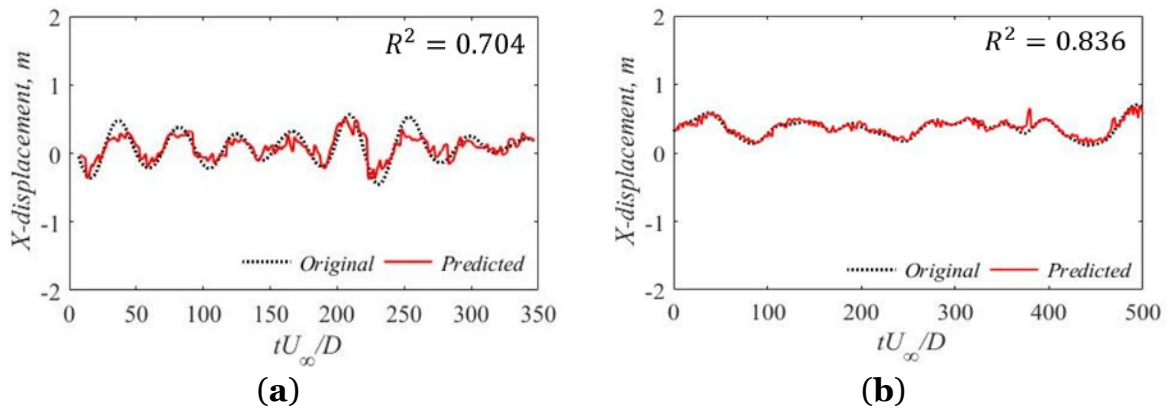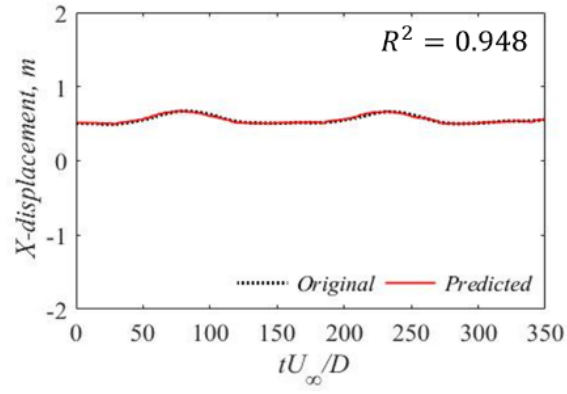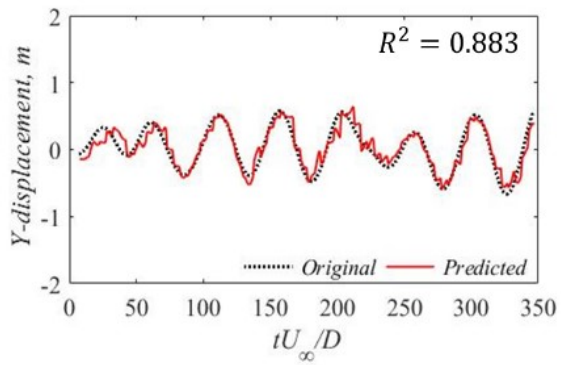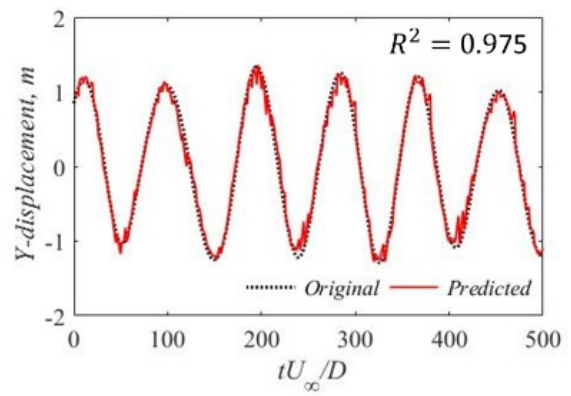

(a)   **(b)**

Figure 4.17. *Cont.*
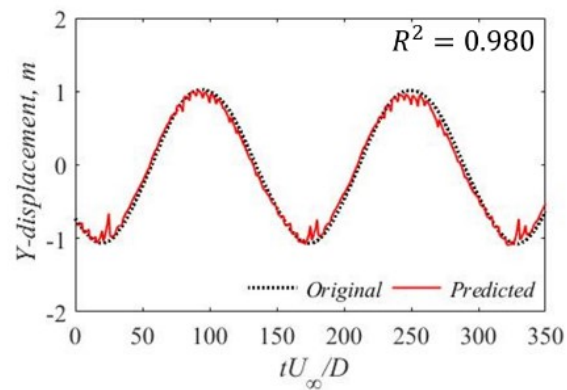
(**c**)

(**d**)

(**e**)

(**f**)

Figure 4.17. *Cont.*
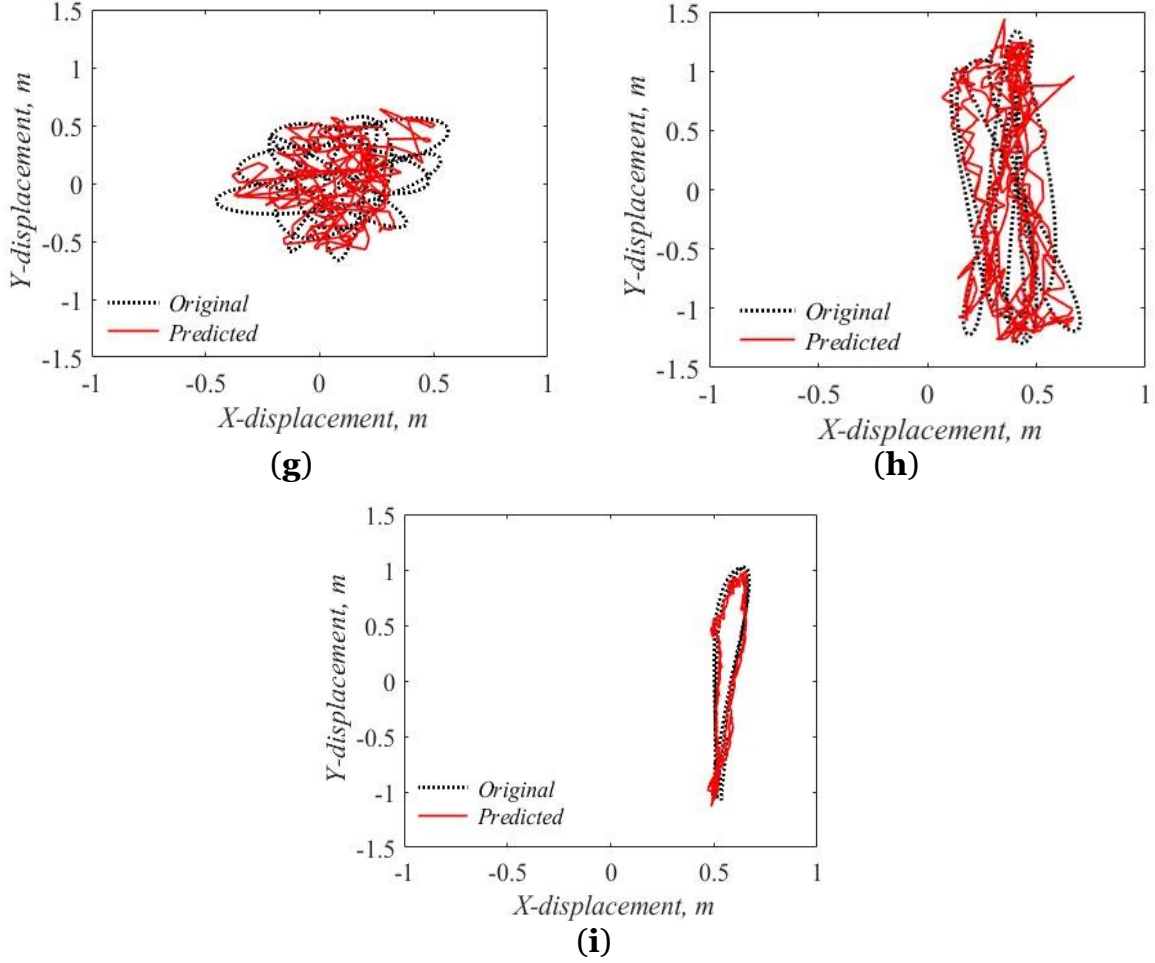
Figure 4.17. The (**a-c**) streamwise, (**d-f**) cross-flow and (**g-i**) 2DoF cylinder displacements obtained by original CFD simulations and POD-LSTM-NN ROM for (**a, d, g**) $u_r = 3$, (**b, e, h**) $u_r = 6$ and (**c, f, i**) $u_r = 11$.

4.3.3. Force Partitioning method

The FPM was widely adopted to estimate the lift and drag forces acting on the body by solely using the surrounding flow field instead of a direct integration of the pressure and viscous stresses on the body surface (Yin et al. (2022) [17], Menon & Mittal (2021) [47], Moriche et al. (2017) [48]). The first step of the FPM is to define the auxiliary potential field, ϕ_i. It is only determined by the instantaneous position and the shape of the immersed body as well as the outer domain boundary. The potential field ϕ_i satisfies the Laplacian equation and boundary conditions as:

$$\text{In the fluid domain: } \nabla^2 \phi_i = 0, \tag{4.19}$$

$$\text{At the surface of the immersed body: } \nabla \phi_i \cdot n = e_i \cdot n, \tag{4.20}$$

At the outer boundaries of the fluid domain: $\nabla\phi_i \cdot n = 0,$ (4.21)

where n is the normal vector towards the body surface and e_i denotes a unit vector; $i = 1$ and 2 correspond to the streamwise and cross-flow directions, respectively.

The second and third steps of the FPM are to project the original Navier-Stokes equation onto the gradient of the auxiliary potential and integrate over the volume of the fluid domain. According to Chang (1992) [41], the force acting on the oscillating body in a constant stream can be found by using the following equation:

$$F_i = -\underbrace{\oint \phi_i \frac{\partial \boldsymbol{u}}{\partial t} \cdot n dA}_{I} + \underbrace{\frac{1}{2}\oint \boldsymbol{u}^2 n \cdot e_i dA}_{II} - \underbrace{\int (\boldsymbol{u} \times \boldsymbol{\omega}) \cdot \nabla\phi_i dV}_{III} + \underbrace{\nu \oint (\boldsymbol{\omega} \times n) \cdot (\nabla\phi_i + e_i) dA}_{IV}$$ (4.22)

where $\boldsymbol{u}$ and $\boldsymbol{\omega}$ are the velocity and vorticity of the flow field, respectively; dA denotes the surface area of the cylinder; ν is a kinematic viscosity.

The first term (I) of Eq. (4.22) represents the contribution of the body acceleration while the second term (II) indicates the contribution of the body kinetic energy. The third (III) and fourth (IV) terms are induced by the influence of the surrounding flow within the whole flow field and the body surface, respectively. The term which is related with Reynolds shear stress in not included in Eq. (4.22) as its contribution is negligible for the high Reynolds number flow as reported in Yin et al. (2022) [17]. In the present study, FPM is applied to estimate the lift and drag forces acting on the 2DoF VIV cylinder at high Re number using the predicted surrounding flow and the cylinder motion by the POD-LSTM-NN ROMs. Figure 4.18 shows the comparison of the time histories of the lift and drag coefficients predicted by the POD-LSTM-NN ROMs and the original CFD simulations by using the sum of the I related to the body motion and III terms related to the surrounding flow of Eq. (4.22). The II and IV terms of Eq. (4.22) are not included into consideration as their contribution is much smaller in comparison with two other components. According to Figure 4.18, the POD-LSTM-NN ROMs with 90% of the flow energy can predict the fluctuation amplitudes of the lift and drag coefficients with a high accuracy. The calculated values of the determination coefficients confirm it. The more precise reconstruction of the lift and drag coefficient time histories is obtained for $u_r = 3$ and 6. These two cases distinct by

the edgy and high fluctuation amplitudes of the lift and drag coefficients in comparison with $u_r = 11$

(a)

(b)

(c)

(d)

(e)

(f)
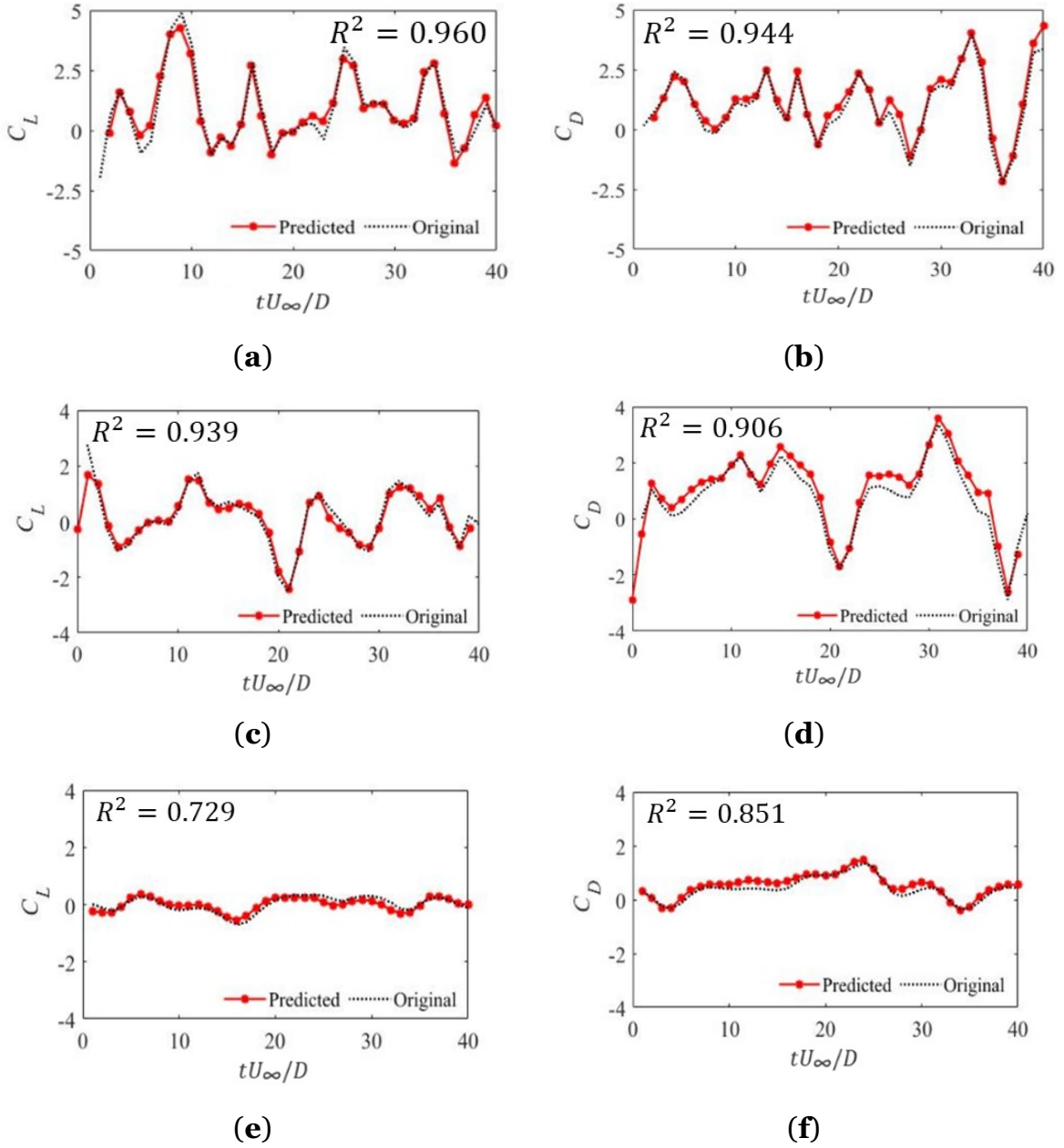
Figure 4.18. Time histories of (**a-c**) the lift and (**d-f**) drag coefficients obtained by means of the force partitioning method by using sum of the *I* and *III* terms of Eq. (4.22) for the flow field predicted by POD-LSTM-NN ROM and the original CFD simulations for (**a, b**) $u_r = 3$, (**c, d**) $u_r = 6$ and (**e, f**) $u_r = 11$.

Moreover, to further reveal the ROM predicted wake flow and uncover the correlation between the dominant flow structures and the hydrodynamic forces on the vibrating cylinder, a close inspection of the predicted term *III*, $C_{L,\mathbf{u}\times\boldsymbol{\omega}}$, using modes with 90% of the flow energy for $u_r = 11$ and the predicted wake flow structures at three

representative time steps corresponding to the peak and zero values are displayed in Figure 4.19. Both the contours of the predicted spanwise vorticity and the force density are shown. The alternative vortex shedding process denoted as vortex A, B, C in Figure 4.19b, as well as the vortices pairs (denoted in Figure 4.19b) and the meandering vortex street in the far-wake is well-captured. It can be seen from the contours of $-(\mathbf{u} \times \boldsymbol{\omega}) \cdot \nabla \phi_y$ (ϕ_y is the lift potential) that near-wake flow structures make a dominant contribution to $C_{L,\mathbf{u} \times \boldsymbol{\omega}}$ and the contributions from the shedding vortices are quickly dissipated. At the two peak values of $C_{L,\mathbf{u} \times \boldsymbol{\omega}}$, the vortex from one side begins to grow and draw the vortex from the other side. Both the two vortices make positive contributions to $C_{L,\mathbf{u} \times \boldsymbol{\omega}}$ and suppress the negative contribution from the shedding vortex from the previous cycle (denoted as C in Figure 4.19c). At the zero value of $C_{L,\mathbf{u} \times \boldsymbol{\omega}}$, the shear layers from the two sides are almost of similar strengths and there is an opposite contribution from the regions between the two shear layers (denoted as D in Figure 4.19e), which leads to the zero value of $C_{L,\mathbf{u} \times \boldsymbol{\omega}}$. In addition, it is obvious that the influences of small-scale noisy structures (denoted in Figure 4.19d as an example) resulting from the mode truncation can be only observed around the shear layer. However, their net contributions to the $C_{L,\mathbf{u} \times \boldsymbol{\omega}}$ values are canceled due to their equal strengths of positive and negative signs.
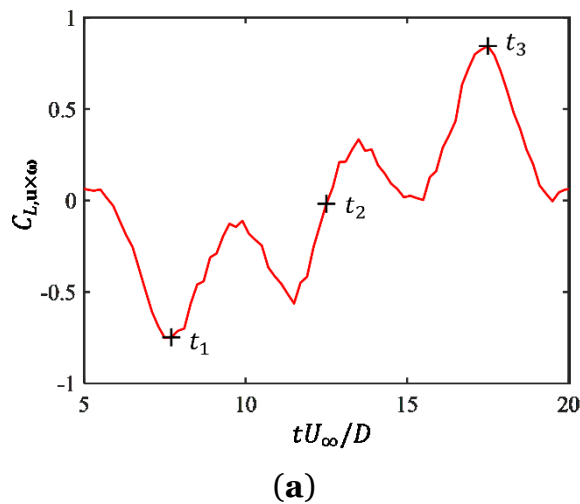

(a)
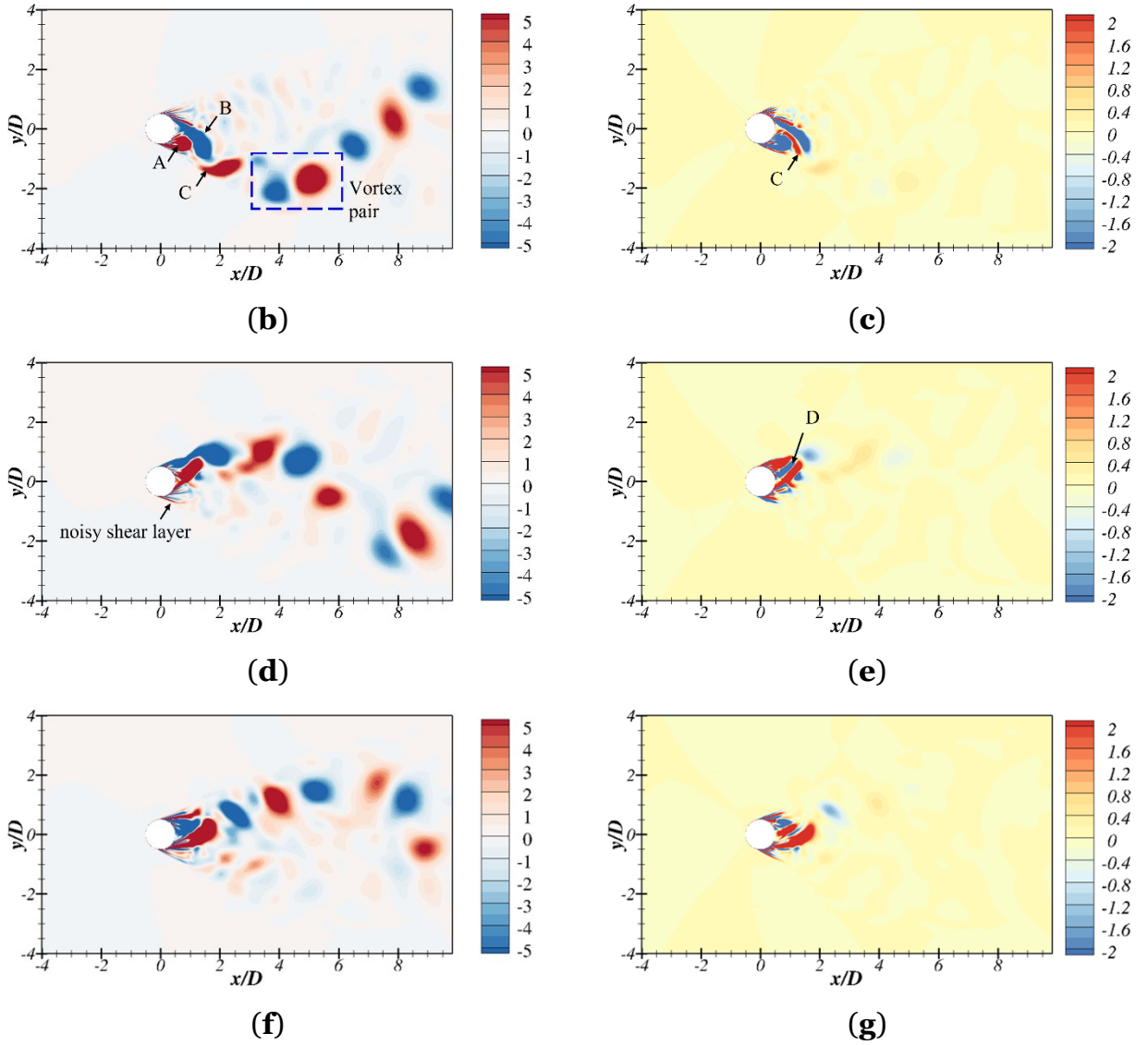
Figure 4.19. *Cont.*

Figure 4.19. (a) Three representative time steps corresponding to two peak values (t_1 and t_3) and a zero value of $C_{L,\mathbf{u}\times\boldsymbol{\omega}}$ (t_2); **(b, d, f)** the contours of the spanwise vorticity at t_1, t_2, t_3, respectively; **(c, e, g)** the contours of the force density $-(\mathbf{u}\times\boldsymbol{\omega})\cdot\nabla\phi_y$.

Conclusions

The ROMs based on LSTM and POD analysis are designed in the present study to predict the instantaneous wake flow evolution of a 2DoF VIV circular cylinder in the upper transition Reynolds number regime ($Re = 3.6 \times 10^6$) with $u_r = 3, 6$ and 11. The datasets of the flow field for training are generated by solving the 2D URANS equations with the standard $k - \omega\ SST$ turbulence model. The POD analysis is applied for the flow field generated by the CFD simulations to extract the dominant modes and their

temporal coefficients. Then, the LSTM-NN is built to predict the instantaneous POD coefficients for future time steps. As a result, the combination of the POD modes and the temporal coefficients predicted by the LSTM-NN allowed to create a reduced-order representation of the high-dimensional datasets and to predict the evolution of the coherent flow structures around the bluff body at the future time instants. Moreover, FPM was introduced to characterize the lift and drag forces acting on the cylinder by using a surrounding flow fields predicted by the POD-LSTM-NN ROMs. The main conclusions can be summarized as follows:

1. In order to create the highly quality ROMs which can represent up to 90% of the flow energy, 228, 208 and 42 POD modes were used for $u_r = 3, 6$ and 11, respectively. The high number of modes for the ROMs is caused by the highly chaotic turbulent flow field. Therefore, it is recommended to test different decomposition techniques and evaluate the performance of the reduced-order representation of the required dominant flow features.

2. In the present study, the same LSTM-NN model parameters are used to train all POD modes to save computational time. Therefore, there is an issue related to incapability of the LSTM-NN to accurately represent the high order POD modes. The possible solution can be to adjust different setting parameters for the low and high order POD modes. However, it leads to a more complexity and less autonomous of the LSTM-NN parameter selection.

3. The temporal evolutions of the dominant POD coefficients can be well-predicted by the designed POD-LSTM-NN ROMs. The good performance of the POD-LSTM-NN ROMs in prediction of the streamwise and cross-flow velocities and the cross-flow displacements is also highlighted for all cases, especially for $u_r = 11$.

4. A good performance of the POD-LSTM-NN ROMs is also confirmed by comparing the estimated forces combined with the FPM applied for the predicted and the CFD simulated flow fields. The forces acting on the cylinder surface subjected to a chaotic turbulent flow predicted by the POD-LSTM-NN ROMs are captured with a high accuracy.

References

1. Moe, G; Holden, K; Yttervoll, P. Motion of spring supported cylinders in subcritical and critical water flows. In *The Fourth International Offshore and Polar Engineering Conference*. OnePetro **1994**.

2. Vikestad, K. Multi-frequency response of a cylinder subjected to vortex shedding and support motions **1998**.

3. Ding, Z; Balasubramanian, S; Lokken, R; & Yung, T. Lift and damping characteristics of bare and straked cylinders at riser scale Reynolds numbers. In *Offshore Technology Conference*. OnePetro **2004**.

4. Bernitsas, M. M., & Raghavan, K. Reduction/suppression of VIV of circular cylinders through roughness distribution at 8× 103< Re< 1.5× 105. In *International Conference on Offshore Mechanics and Arctic Engineering*. **2008**, 48227. 1001-1005.

5. Hassanpour, M; Morton, C; Martinuzzi, R. Effect of harmonic inflow perturbation on the wake vortex dynamics of a cylinder undergoing two-degree-of-freedom vortex-induced vibration near a plane boundary. *Fluids*, **2022**, *34*(10), 103618

6. Jiang, Z; Gao, Y; Fu, S; Chai, S; Shi, C. Effects of surface roughness on two-degree-of-freedom vortex-induced vibration of a circular cylinder in oscillatory flow. *Fluids*, **2023**, *35*(1), 015154.

7. Verma, M; De, A. Three-Dimensionality in the flow of an elastically mounted circular cylinder with two-degree-of-freedom vortex-induced-vibrations. *Fluids*, **2022**, *34*(10), 103616.

8. Serta, C; Janocha, M; Yin, G; Ong, M. C. Numerical simulations of flow-induced vibrations of two rigidly coupled cylinders with uneven diameters in the upper transition Reynolds number regime. *J. Fluid Struct*. **2021**, *105*, 103332.

9. Lumley, J. The structure of inhomogeneous turbulent flows. *Atmospheric turbulence and radio wave propagation*. **1967**, 166-178.

10. Janocha, M; Ong, M; Yin, G. Large eddy simulations and modal decomposition analysis of flow past a cylinder subject to flow-induced vibration. J. *Phys. Fluids*. **2022**, *34*(4), 045-119.

11. Mendez, M. A., Balabane, M., & Buchlin, J. M. (2019). Multi-scale proper orthogonal decomposition of complex fluid flows. *J. Fl. Mech*. **2019**, 870, 988-1036

12. Schubert, Y; Sieber, M; Oberleithner, K; Martinuzzi, R. Towards robust data-driven reduced-order modelling for turbulent flows: application to vortex-induced vibrations. *J. Theor. Comp. Fluid Dyn*. **2022**, *36*(3), 517-543.

13. Eiximeno, B; Miró, A; Cajas, J; Lehmkuhl, O; Rodriguez, I. On the Wake Dynamics of an Oscillating Cylinder via Proper Orthogonal Decomposition. *Fluids*. **2022**, *7*(9), 292.

14. Schmid, P. Dynamic mode decomposition of numerical and experimental data. *J. Fluid Mech*. **2010**, *656*, 5-28.

15. Jovanović, M; Schmid, P' Nichols, J. Sparsity-promoting dynamic mode decomposition. *Physics of Fluids*. **2014**, *26*(2), 024-103

16. Janocha, M; Yin, G; Ong, M. Modal Analysis of Wake Behind Stationary and Vibrating Cylinders. *J. Offshore Mech. and Arctic Engin*. **2021**, *143*(4).

17. Menon, K; Mittal, R.. Dynamic mode decomposition based analysis of flow over a sinusoidally pitching airfoil. *J. Fluid Struct.*. **2020**, *94*, 102-886.

18. Yin, G; Janocha, M; Ong, M. Estimation of Hydrodynamic Forces on Cylinders Undergoing Flow-Induced Vibrations Based on Modal Analysis. *Journal of Offshore Mechanics and Arctic Engineering*. **2022,** *144*(6), 060-904.

19. Barone, M; Kalashnikova, I; Segalman, D; Thornquist, H. Stable Galerkin reduced order models for linearized compressible flow. *J. Com. Physics*. **2009**, *228*(6), 1932-1946.

20. Frère, A; Carton de Wiart, C; Hillewaert, K; Chatelain, P; Winckelmans, G. Application of wall-models to discontinuous Galerkin LES. *Fluids*. **2017**, 29(8), 085111.

21. Qi, X; Wang, Z; Zhu, J; Tian, L; Zhao, N. (2023). A high-order nonlinear limiter for discontinuous Galerkin method on parallel adaptive Cartesian grids. *Fluids*. **2023**, *35*(3), 036108.

22. Carlberg, K; Bou-Mosleh, C; Farhat, C. Efficient non-linear model reduction via a least-squares Petrov–Galerkin projection and compressive tensor approximations. *J. Num. Methods in Engin*. **2011**, *86*(2), 155-181.

23. Rempfer, D. On low-dimensional Galerkin models for fluid flow. *J. Theor. and Comp. Fluid Dyn*. **2000**, *14*(2), 75-88.

24. Akhtar, I; Nayfeh, A; Ribbens, C. On the stability and extension of reduced-order Galerkin models in incompressible flows: a numerical study of vortex shedding. *J. Theor. and Comp. Fluid Dyn*. **2009**, *23*, 213-237.

25. Iollo, A; Lanteri, S; Désidéri, J. Stability properties of POD–Galerkin approximations for the compressible Navier–Stokes equations. *J. Theor. and Comp. Fluid Dyn*. **2000**, *13*(6), 377-396.

26. Wang, Z; Li, X; Liu, L; Wu, X; Hao, P; Zhang, X; He, F. Deep-learning-based super-resolution reconstruction of high-speed imaging in fluids. *Fluids*. **2022**, *34*(3), 037107.

27. Maulik, R; San, O. A neural network approach for the blind deconvolution of turbulent flows. *J. Fluid Mech.* **2017**, *831*, 151-181.

28. Zhu, L; Zhang, W; Kou, J; Liu, Y. Machine learning methods for turbulence modeling in subsonic flows around airfoils. *Fluids*. **2019**, *31*(1), 015105.

29. Gardner, M; Dorling, S. Artificial neural networks (the multilayer perceptron)—a review of applications in the atmospheric sciences. *J. Atmospheric environment*. **1998**, *32*(14-15), 2627-2636.

30. Orhan, U; Hekim, M; Ozer, M. EEG signals classification using the K-means clustering and a multilayer perceptron neural network model. *J. Expert Systems with Applications*. **2011**, *38*(10), 13475-13481.

31. Gao, H; Sun, L; Wang, J. Super-resolution and denoising of fluid flow using physics-informed convolutional neural networks without high-resolution labels. Fluids. **2021**, *33*(7), 073603.

32. Tong, W; Wang, S; Yang, Y. Estimating forces from cross-sectional data in the wake of flows past a plate using theoretical and data-driven models. *Fluids*, **2022**, *34*(11), 111905.

33. Maulik, R; Lusch, B; Balaprakash, P. Reduced-order modeling of advection-dominated systems with recurrent neural networks and convolutional autoencoders. *Fluids*, **2021**, *33*(3), 037106.

34. Qin, Y; Song, D; Chen, H; Cheng, W; Jiang, G; Cottrell, G. A dual-stage attention-based recurrent neural network for time series prediction. **2017,** *arXiv preprint arXiv:1704.02971*.

35. Mohan, A; Gaitonde, D. A deep learning based approach to reduced order modeling for turbulent flow control using LSTM neural networks. **2018**, arXiv preprint arXiv:1804.09269.

36. Yeo, K; Melnyk, I. Deep learning algorithm for data-driven simulation of noisy dynamical system. *J. Comp. Physics*. **2019**, *376*, 1212-1231.

37. Rahman, S; Pawar, S; San, O; Rasheed, A; Iliescu, T. Nonintrusive reduced order modeling framework for quasigeostrophic turbulence. *Physical Review E*. **2019**, *100*(5), 053306.

38. Nakamura, T; Fukami, K; Hasegawa, K; Nabae, Y; Fukagata, K. Convolutional neural network and long short-term memory based reduced order surrogate for minimal turbulent channel flow. *Physics of Fluids*. **2021**, *33*(2), 025116.

39. Fukami, K; Nakamura, T; Fukagata, K. Convolutional neural network based hierarchical autoencoder for nonlinear mode decomposition of fluid field data. *J. Phys. Fluids.* **2020**, *32*(9), 095110.

40. Bukka, S; Gupta, R; Magee, A; Jaiman, R. Assessment of unsteady flow predictions using hybrid deep learning based reduced-order models. *J. Phys. Fluids*. **2021**, *33*(1), 013601.

41. Yousif, M; Lim, H. Reduced-order modeling for turbulent wake of a finite wall-mounted square cylinder based on artificial neural network. *J. Phys. of Fluids*. **2022**, *34*(1), 015116.

42. Chang, C. Potential flow and forces for incompressible viscous flow. *Proceedings of the Royal Society of London. Series A: Mathematical and Physical Sciences*. **1992**, *437*(1901), 517-525.

43. Menter, F; Kuntz, M; Langtry, R. Ten years of industrial experience with the SST turbulence model. *Turbulence, heat, and mass transfer*. **2003**, *4*(1), 625-632.

44. Nieto, F; Hargreaves, D; Owen, J; Hernández, S. On the applicability of 2D URANS and SST k-ω turbulence model to the fluid-structure interaction of rectangular cylinders. *J. Engineering Applications of Comp. Fluid Mechanics*. **2015**, *9*(1), 157-173.

45. Janocha, M; Ong, M. Vortex-induced vibrations of piggyback pipelines near the horizontal plane wall in the upper transition regime. *Marine Structures*. **2021**, *75*, 102872.

46. Gsell, S., Bourguet, R., & Braza, M. Two-degree-of-freedom vortex-induced vibrations of a circular cylinder at $Re = 3900$. *J. Fluids and Struct*. **2016**, *67*, 156-172.

47. Gers, F. A; Schmidhuber, J; Cummins, F. Learning to forget: Continual prediction with LSTM. *Neural computation*. **2000**, *12*(10), 2451-2471.

48. Menon, K; Mittal, R. Significance of the strain-dominated region around a vortex on induced aerodynamic loads. *J. Fluid Mech*. **2021**, *918*, R3.

49. Moriche, M; Flores, O; García-Villalba, M. On the aerodynamic forces on heaving and pitching airfoils at low Reynolds number. *J. Fl. Mech*. **2017**, *828*, 395-423.

Chapter 5.

Conclusions

5.1. Summary of the key findings

In the present master's thesis, modern techniques for analysing the flow field over cylindrical bluff bodies undergoing a high Reynolds number regime flow are implemented. The combination of the reduced order modelling and neural network allows to decrease the complexity of the performed calculations and minimize computational costs. In the present study, the circular cylinders represent the subsea slender structures such as production flowlines, umbilicals, risers, jumpers. Two different subsea operational conditions are analysed: two tandem circular cylinders and a single 2DoF VIV circular bluff body. The open source CFD toolbox OpenFOAM v2012 is utilized to conduct all simulations in the present study. The 2D URANS equations with the standard $k - \omega$ SST turbulence model are solved. The ROMs are designed by implementing modal decomposition techniques as SPDMD and POD for tandem circular cylinders case and the 2DoF VIV bluff body, respectively. The dominant modes which capture the dominant spatial-temporal coherent structures of the flow field are chosen to build ROMs. The LSTM-NN are applied to predict the evolution of the POD modes temporal coefficients as well as the streamwise and cross-flow velocities and displacements of the cylinder at the future time instances. In the present study, the LSTM-NN is designed based on the open-source toolbox TensorFlow and Keras.

The main findings of Chapter 3 can be summarized as flow:

1. The flow field over tandem circular cylinders at $Re = 3.6 \times 10^6$ significantly depends on the relative distance between the bluff bodies. With increasing L/D between the circular cylinders, the reattachment point of the separated UC shear layers constantly changes the position on the surface of the DC leading to overshoot, FSR, FR, FSR and bi-stable the flow regimes transformations.

2. Existing of the third super-harmonic for considered cases can be explained by the reattachment of the shear layer of the lower vorticity slice on DC surface. While the appearance of the second super-harmonic for $L/D = 2.5$ is connected with the assistance of the upper vorticity slice of the reattached shear layer to the development of the negative coherent structure behind the DC.

93

3. The relative distance between the two cylinders influences on such parameters as $\overline{C_D}$, $C_{L,rms}$ and St. For example, with the decreasing L/D between the two bluff bodies, $\overline{C_D}$ constantly reduces and archives the negative value at $L/D = 1.56$. It happens due to a low pressure at the surface of the DC caused by the cavity flow between UC and DC. The enlargement of the C_L fluctuation amplitude at $L/D = 2.5$ is connected with the FR flow regime which characterized by the significant interactions of the shear layers. A sudden reduction of the St values is observed at $L/D \geq 1.8$ when the reattachment flow regime dominates.

4. The SPDMD approach has been applied for the modal analysis of the flow field and construction of the ROMs. The modal decomposition analysis reveals that Mode 2 for $L/D = 1.8$ and 3 does not contribute to the lift force. Therefore, there is no peak in the frequency spectra of the lift force at the second harmonic of St for these two cases. Furthermore, the ROMs have been designed based on the SPDMD modes which contribute the most to the flow field dynamics. The reduced order representations of the flow field at the high Reynolds number flow could correctly reconstruct the wake dynamics behind the two tandem cylinders at the different L/D between them.

The main findings of Chapter 4 can be summarized as flow:

1. In order to design the high-quality ROMs for the turbulent flow field around 2DoF VIV cylinder, 228, 208 and 42 POD modes are used for $u_r = 3, 6$ and 11, respectively, to capture 90% of the flow energy.

2. In the present study, there is an issue related to incapability of the LSTM-NN to accurately capture the high order POD modes as the same LSTM-NN model parameters are used to train low and high order POD modes. It has been done to save computational resources. The adjustment of the different setting parameters for the low and high order POD modes can solve the problem. However, it makes the LSTM-NN parameter selection less autonomous.

3. The POD-LSTM-NN ROMs show good capabilities in prediction of the POD modes temporal coefficients for future time steps as well as in prediction of the streamwise and cross-flow velocities and the cross-flow displacements, especially for $u_r = 11$.

4. The FPM method is applied to evaluate the lift and drag forces acting on the cylinder surface by using the predicted and the CFD simulated flow fields. The POD-LSTM-

NN ROMs prove their abilities to capture the forces acting on the cylinder surface with a high accuracy.

5.2. Future work

Following suggestions for further investigations can be made:

1. The alternative training strategy (unified model approach) for the LSTM-NN can be tested in order to account for the issues of the multiple model training strategy which was utilized in the present study. According to the unified model approach, the NN is trained with the samples from all ranks of the POD modes, not just from POD modes of the same rank. The unified NN model can be used to predict the coefficients for all POD modes.

2. Different modal decomposition approaches can be tested to define the most efficient decomposition techniques for the reduced-order representation of the dominant spatial-temporal coherent structures of the flow field around 2DoF VIV circular cylinder at high Reynolds number flow.

3. Test the performances of the different NN architectures such as convolution neural network (CNN) - LSTM, multilayer perceptrons (MLP), etc. for the prediction of the flow field evolution over cylindrical bluff bodies subjected to a high Reynolds number flow.